University of Alberta

Anode Materials for Sour Natural Gas Solid Oxide Fuel Cells

by

Nemanja Danilovic

A thesis submitted to the Faculty of Graduate Studies and Research
in partial fulfillment of the requirements for the degree of

Doctor of Philosophy
in
Materials Engineering

Chemical and Materials Engineering

Spring 2010
Edmonton, Alberta

Examining Committee

Dr. Jingli Luo, Chemical and Materials Engineering

Dr. Karl Chuang, Chemical and Materials Engineering

Dr. Tom Etsell, Chemical and Materials Engineering

Dr. Steven Bergens, Chemistry

Dr. John Vohs, University of Pennsylvania, Chemical and Biomolecular Engineering.

Abstract

Novel anode catalysts have been developed for sour natural gas solid oxide fuel cell (SOFC) applications. Sour natural gas comprises light hydrocarbons, and typically also contains H_2S. An alternative fuel SOFC that operates directly on sour natural gas would reduce the overall cost of plant construction and operation for fuel cell power generation. The anode for such a fuel cell must have good catalytic and electrocatalytic activity for hydrocarbon conversion, sulfur-tolerance, resistance to coking, and good electronic and ionic conductivity.

The catalytic activity and stability of ABO_3 (A= La, Ce and/or Sr, B=Cr and one or more of Ti, V, Cr, Fe, Mn, or Co) perovskites as SOFC anode materials depends on both A and B, and are modified by substituents. The materials have been prepared by both solid state and wet-chemical methods. The physical and chemical characteristics of the materials have been fully characterized using electron microscopy, XRD, calorimetry, dilatometry, particle size and area, using XPS and TGA-DSC-MS. Electrochemical performance was determined using potentiodynamic and potentiostatic cell testing, electrochemical impedance analysis, and conductivity measurements.

Neither $Ce_{0.9}Sr_{0.1}VO_3$ nor $Ce_{0.9}Sr_{0.1}Cr_{0.5}V_{0.5}O_3$ was an active anode for oxidation of H_2 and CH_4 fuels. However, active catalysts comprising $Ce_{0.9}Sr_{0.1}V(O,S)_3$ and $Ce_{0.9}Sr_{0.1}Cr_{0.5}V_{0.5}(O,S)_3$ were formed when small concentrations of H_2S were present in the fuels. The oxysulfides formed in-situ were very active for conversion of H_2S. The maximum performance improved from 50 mW cm^{-2} to 85 mW cm^{-2} in 0.5% H_2S/CH_4 at 850 ^oC with partial substitution of V by Cr in $Ce_{0.9}Sr_{0.1}V(O,S)_3$. Selective conversion of H_2S offers potential for sweetening of sour gas without affecting the hydrocarbons.

Perovskites $La_{0.75}Sr_{0.25}Cr_{0.5}X_{0.5}O_{3-\delta}$, (henceforth referred to as LSCX, X=Ti, Mn, Fe, Co) are active for conversion of H_2, CH_4 and 0.5% H_2S/CH_4. The order of activity in the different fuels depends on the substituent element: CH_4, X = Fe>Mn>Ti; H_2, X = Fe>Mn>Ti; and 0.5% H_2S/CH_4, X = Fe>Ti>Mn. The electrocatalytic activity for methane oxidation in a fuel cell correlates with ex-situ temperature programmed catalytic activity. A process is proposed to explain the difference in catalyst order and enhanced

activities in H_2S/CH_4 as fuel compared to CH_4 alone. The maximum power density of 250 mW cm^{-2} was attained using a fuel cell with a composite anode, LSCFe-GDC | YSZ(0.3 mm) | Pt, operated at 850 ^oC (GDC is $Ce_{0.9}Gd_{0.1}O_3$, a good mixed conductor under reducing conditions).

Acknowledgements

Firstly, I'd like to thank my supervisors Dr. Jingli Luo and Dr. Karl Chuang for the support and guidance they have given me in the last four years. You have helped me learn, grow and mature. A special thanks to my committee members, Dr. John Vohs, Dr. Tom Etsell, Dr. Tony Yeung and Dr. Steven Bergens for the time and effort you have taken for my exam.

Secondly, many thanks to my group members past and present: Dr. Alan Sanger, Vitaly, Juri, Zhengrong, Jinxia, Adrien, Cheng, Fu, Xiaoxong, Milad, Andrey and Anh. Without you this would not have been possible. And thirdly, all the support staff at the University of Alberta who are too many to name here and I do not wish to miss anyone. You have made my stay memorable and have greatly contributed to any work I did at the UofA.

To my friends: Ali, Ardalan, Andrew, Babak, Branden, Colin, Chris Holt, Chris Harrower, David, Erik, Errol, Julian, Kinglsey, Lily, Mohsen, Nima, Oswaldo, Patrick, Saeid, Sepideh. And to my family: Mimi, Mirna, Nada, Zelja and Sveta. Thanks for being there for me, everyone in their own way, I am grateful.

I stand on your shoulders!

Nemanja Danilovic

August 31, 2009.

Contents

List of Tables

List of Figures

List of Abbreviations

AE	Alkaline earth
AFC	Alkaline fuel cell
BCC	Body centered cubic
CGO	$Ce_{0.9}Gd_{0.1}O_2$
CN	Coordination number
CSV	$Ce_{0.9}Sr_{0.1}VO_3$
CSCV	$Ce_{0.9}Sr_{0.1}Cr_{0.5}V_{0.5}O_3$
CTE	Coecient of thermal expansion
CUS	Coordinatively unsaturated sites
DSC	Differential scanning calorimetry
EMF	Electromotive force
EIS	Electrochemical impedance spectroscopy
FCC	Face centered cubic
GDC	$Ce_{0.9}Gd_{0.1}O_2$
HCP	Hexagonal close packed
LSCCo	$La_{0.75}Sr_{0.25}Cr_{0.5}Co_{0.5}O_3$
LSCM or LSCMn	$La_{0.75}Sr_{0.25}Cr_{0.5}Mn_{0.5}O_3$
LSGM	$La_{0.8}Sr_{0.2}Ga_{0.8}Mg_{0.2}O_3$
LSF	$La_{0.7}Sr_{0.3}FeO_3$
LSFC	$La_{0.7}Sr_{0.3}Fe_{0.4}Co_{0.6}O_3$
LSM	$La_{0.8}Sr_{0.2}MnO_3$
LSCTi	$La_{0.75}Sr_{0.25}Cr_{0.5}Ti_{0.5}O_3$
LSV	$La_{0.7}Sr_{0.3}VO_3$
MCFC	Molten carbonate fuel cell
MEA	Membrane electrode assembly
MIEC	Mixed ionic electronic conductors
MO	Metal oxide
MMO	Mixed metal oxide
MS	Mass spectrometer
NG	Natural gas
OCV	Open circuit voltage
OCP	Open circuit potential
PAFC	Phosphoric acid fuel cell
PEMFC	Polymer electrolyte fuel cell
RE	Rare earth

RP	Ruddlesden-Popper
S/C	Steam to carbon ratio
SCF	$SrCo_{0.4}Fe_{0.6}O_3$
SEM	Scanning electron microscope
SGSOFC	Sour gas solid oxide fuel cell
SOFC	Solid oxide fuel cell
TGA	Thermogravimetric analysis
TM	Transition metal
TPB	Triple phase boundary
VLY	VO_x-$LaCrO_3$-YSZ
XPS	X-ray photoelectron spectroscopy
XRD	X-ray diffraction
YSZ	$Zr_{0.92}Y_{0.08}O_2$

Chapter 1

Introduction

1.1 Energy demands, efficiency and emissions

Based on the current rate of growth, the US Department of Energy and the International Energy Agency project that our demand for energy will continue to grow throughout the present century [1], primarily due to the increasing demands from the two most populous nations in the world, China and India, as they continue to industrialize and their populations continue to grow.

This energy is used to power the worlds cities, manufacturing, transportation and agriculture. Figure 1.1 shows the sources of the worlds energy, and the projected demand from each source [1].

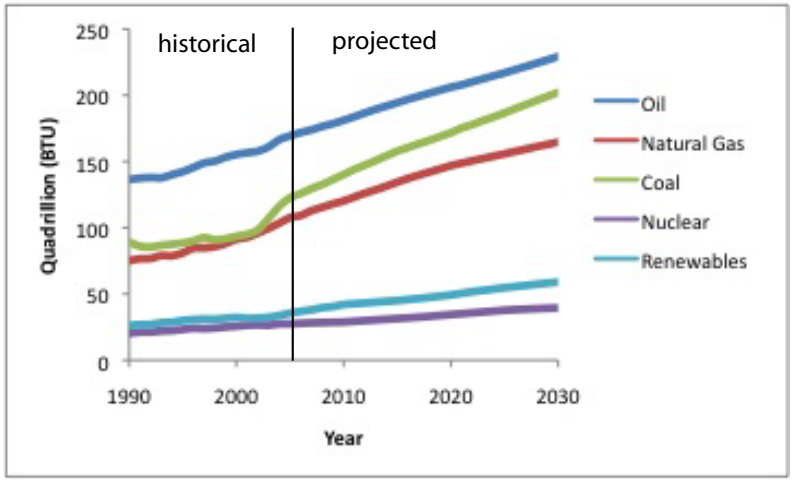

Figure 1.1: Timeline of global energy consumption.

It is clear that carbon based fuels, oil, gas and coal, currently account for the majority of our power generation. At the current course of development of nuclear energy supply, and R&D on alternative energy sources, we are projected to remain in a carbon based economy. It will be a very long time before carbon-free energy sources will be able to meet demand and

growth. Canada's energy breakdown is provided in Figure 1.2. Canada-wide, our energy trends parallel that of the developed areas of the world [2]. However, provincially British Columbia, Quebec and Ontario differ in that they meet their energy demand primarily from hydropower (BC, QC) and nuclear (ON), while the remaining Canadian provinces largely rely on coal.

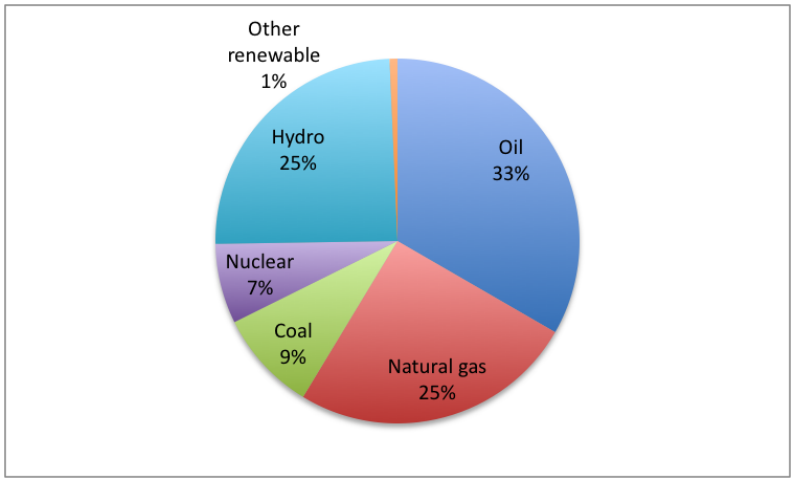

Figure 1.2: Canada's energy consumption.

As these demands are increasingly met with coal generated electricity, the global CO_2 emissions are increasing simultaneously. This is a potential cause of global anthropogenic climate change, but more importantly the local air quality is diminished, leading to many common health complications. Figure 1.3 shows the current and projected emission trends globally [1].

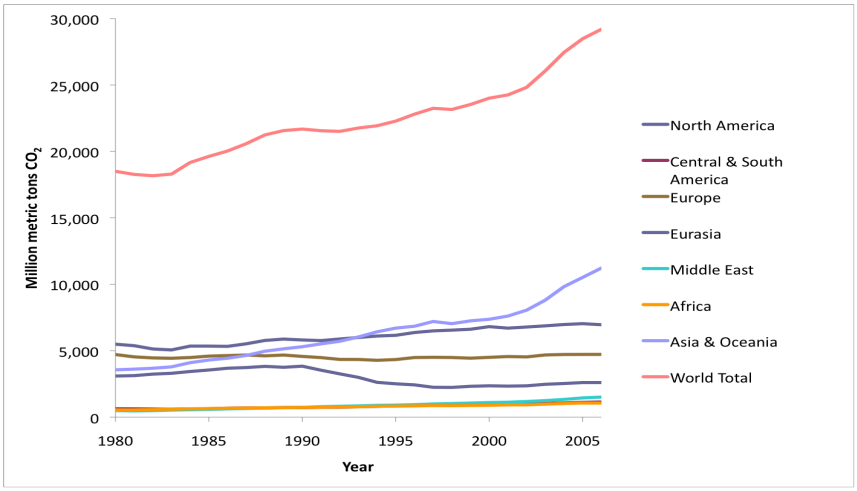

Figure 1.3: Global CO_2 emissions by continent.

Since we must meet our energy demands, and our only immediate realistic choice is to

use carbon based fuels to achieve this, we have only one solution: we must use our limited resources more efficiently. One piece of the efficiency equation is on the consumers' side; however, we currently produce that energy from fossil fuels at around 40% efficiency using gas turbines (heat engines) and this is the most likely source of improvement. A potentially more efficient way of using fossil fuels comes from fuel cells.

1.2 Fuel cells

Fuel cells were first theorized in 1838 by Christian Friedrich Schönbein and demonstrated by Sir William Grove in 1839 [3]. The initial design was a low temperature cell that utilized platinum electrodes and a sulphuric acid electrolyte. Over 160 years later fuel cells are not in widespread use, as batteries and the internal combustion engine, which were invented around the same time, rule the market. Today there are many types of fuel cells, using different types of fuels, addressing different application areas. Table 1.1 [4] lists the most common fuel cell types; other less common types are not included as they are variants of the most common types or are in the very early stages of development [4].

Table 1.1: Fuel cell types.

	Polymer electrolyte (PEFC)	Alkaline (AFC)	Phosphoric acid (PAFC)	Molten carbonate (MCFC)	Solid oxide (SOFC)
Operating T	80^oC	65-220^oC	205^oC	650^oC	600-1000^oC
Electrolyte	NAFION	KOH	H_3PO_4 in SiC	(Na,K)CO_3 in $LiAlO_2$	$Zr_{0.98}Y_{0.02}O_2$
Carrier	H^+	OH^-	H^+	CO^{3-}	O^{2-}
Anode	Pt-C	Ni(+Pt)	Pt	Ni	Ni-YSZ
Cathode	Pt-C	Ni(+Pt)	Pt	NiO	$LaSrMnO_3$

The most promising fuel cell in development for stationary power generation applications is the solid oxide fuel cell (SOFC). High temperature fuel cell has a solid ceramic membrane and electrodes that can potentially operate on a wide range of fuels [5]. SOFCs are ideal for stationary power generation due to their small footprint, modular design and high temperature of operation. There has been a large push in the last two decades to develop SOFCs and bring the technology to a wider commercial market. SOFCs have several operating advantages [4]:

- High efficiency 60% electrical
- High temperature operation allows the waste heat to be used to increase overall efficiency over 80% with heat recovery
- Use of reformed hydrocarbons as a fuel

Large multinational corporations and start-ups such as General Electric, Siemens Westinghouse, Silzer Hexis Ltd., Global Thermoelectric, Rolls-Royce and Liliputian are all engaged in SOFC research and development [6]. There are currently pilot plants running worldwide ranging in size from several kW to MW. 1 kW units are being leased in Japan to households.

In theory any fuel that can be oxidized can be used in a SOFC, such as propane, butane, gasoline or diesel, natural gas (methane), and syngas (CO, H_2) etc. [7-14]. Many reviews and books dealing with solid oxide fuel cells highlight research focused on pure hydrogen and various forms of natural gas fuels [5, 15-18]. However, hydrogen is expensive to produce and hard to transport and contain, and is, therefore, not the most convenient choice of fuel. While natural gas fueled SOFCs currently require that the CH_4 be reformed to H_2 and CO prior to its use, and all of the H_2S present in pipeline gas be completely removed, this increases the plant size and complexity and decreases the overall efficiency of the system. Ideally, natural gas would be used directly as the anode gas, and oxidized in-situ. This is an active area of research in the SOFC field as it requires novel catalyst materials.

1.3 Sour natural gas fuel cells (SGSOFC)

Natural gas consists primarily of CH_4, with minor amounts of higher hydrocarbons and nitrogen. If it does not contain a significant concentration of H_2S it is called sweet natural gas. If it contains H_2S in excess of about 4 ppm it is called sour natural gas. The composition of one sour natural gas is shown in Table 1.2. Most oil and gas wells in eastern BC and Alberta contain large amounts of H_2S. Sweet wells are tapped first, followed by sour wells due to the extra cost involved. The sour gas either must be diluted with sweet gas, or it must be separated from the natural gas (a process called sweetening). Hydrogen sulfide is removed using the Claus process, which is expensive and requires large infrastructure investments [19]. Only then can it be transported by pipeline. The majority of untapped wells consist of sour gas and sour oil. Often, smaller fields are uneconomical for development. A SOFC deployed at the well site could utilize the sour natural gas as a fuel, with little lower infrastructure investment.

Table 1.2: Composition of an exemplary sour natural gas

Component	vol.%
Methane	85
Ethane	6
Propane	2
Nitrogen	3
Carbon dioxide	1
Higher hydrocarbons	1
Hydrogen Sulfide	>4 ppm

A secondary use for SGSOFCs is in dilute H_2S-containing natural gas, or pipeline gas. State of the art Ni-YSZ systems are poisoned in the presence of several ppm H_2S. Hence, if a fuel cell was sufficiently active for use with natural gas, the good sulfur tolerance would increase their market potential dramatically. The majority of fuel cell research has been dedicated to solid-oxide conducting high-temperature fuel cells that use nickel supported on yttria stabilized zirconia (Ni-YSZ) or other anodes to electrochemically convert pure hydrogen. Fuels containing sulfur and promote carbon deposition (with C containing fuels) cause deactivation and poisoning of the anode and degradation of performance. Current anode materials cannot utilize sour natural gas or fuels with H_2S impurities in them without sulfur removal. Hence there is a demand for sulfur resistant materials and high performance methane fuel anode materials (sulfur resistance $>$ 50 ppm and power density $>$300 mW cm^{-2}), in addition to a reduction of the operating temperature to below 800 ^oC to avoid carbon deposition.

In order for the sour gas to be utilized in a SOFC, the electrolyte and anode must be sulfur tolerant, but also the peripheral equipment must be corrosion resistant (piping, current collectors as well as fuel and oxidant distribution channels). Additionally, carbon deposition from methane is easily catalyzed at high temperatures, a major problem with Ni-YSZ anode materials; the SGSOFC must also be resistant to carbon deposition. The anode must be catalytically active for the conversion of the fuel, chemically stable in the fuel gas, and electronically and ionically conductive.

1.4 Scope of thesis

The goal of this project is to develop an anode catalyst for a solid oxide fuel cell running on sour natural gas fuel. The motivation for the work is two fold: first, the abundance and underutilization of sour natural gas fuel in Alberta and the world; second, the need for a sulfur tolerant SOFC anode catalyst. Specifically, the anodes materials developed and tested were mixed metal oxide anode materials (ceramics). They were tested for their activity and stability in a model sour natural gas 0.5% H_2S/CH_4, in addition to H_2 and CH_4.

This thesis comprises fuel cell background theory, and includes experimental results, discussion and conclusions based on the following published and submitted journal articles:

- N. Danilovic, J.L. Luo, K.T. Chuang, A.R. Sanger, J. Power Sources, 192 (2009) 247-257.
- N. Danilovic, J.L. Luo, K.T. Chuang, A.R. Sanger, J. Power Sources, 194 (2009) 252-262.
- N. Danilovic, V. Alzate-Restrepo, Z.R. Xu, J.L. Luo, J.H. Hill, K.T. Chuang, A.R. Sanger, Appl. Catal. A, to be submitted.

- N. Danilovic, A. Vincent, J.L. Luo, K.T. Chuang, A.R. Sanger, Chem. Mat., (2009) doi:0.1021/cm901875u.

1.5 References

[1] Energy Information Agency, US Department of Energy, www.eia.doe.gov, (accessed May 2009).

[2] Envirnonment Canada, Government of Canada, www.ec.gc.ca (accessed May 2009).

[3] P. Gilreath, B.N. Singh, P. Rastgoufard, IEEE Region 5 Annual Technical Conference, April 11, (2003), 29-32.

[4] EG&G Technical Services Inc., "Fuel Cell Handbook", 7th edition, 2004.

[5] K. Kendall, N.Q. Minh, S.C. Singhal, in: S.C. Singhal, K. Kendall (Eds.), "High Temperature SOFCs: Fundamentals, Design and Applications", Elsevier, 2003.

[6] Weaver Associates, G. Weaver, "World Fuel Cells: An Industry Profile with Market Prospects to 2010", Elsevier Science, New York, 2002.

[7] N.Q. Minh, Solid State Ionics, 174 (2004) 271-277.

[8] F.Y. Wang, G.B. Jung, A. Su, S.H. Chan, X. Hao, Y.C. Chiang, J. Power Sources, 185 (2008) 862-866.

[9] M.R. Pillai, I. Kim, D.M. Bierschenk, S.A. Barnett, J. Power Sources, 185 (2008) 1086-1093.

[10] D.D. Burnette, G.G. Kremer, D.J. Bayless, J. Power Sources, 182 (2008) 329-333.

[11] X.F. Ye, S.R. Wang, Z.R. Wang, L. Xiong, X.E. Sun, T.L. Wen, J. Power Sources, 177 (2008) 419-425.

[12] H. Kishimoto, K. Yamaji, T. Horita, Y.P. Xiong, N. Sakai, M.E. Brito, H. Yokokawa, J. Power Sources, 172 (2008) 67-71.

[13] Z.F. Zhou, R. Kumar, S.T. Thakur, L.R. Rudnick, H. Schobert, S.N. Lvov, J. Power Sources, 171 (2007) 856-860.

[14] K. Xie, Q.L Ma, B. Lin, Y.Z. Jiang, J.F. Gao, X.Q. Liu, G.Y. Meng, J. Power Sources, 170 (2007) 271-[8] A. Atkinson, S. Barnett, R.J. Gorte, J.T.S. Irvine, A.J. McEvoy, M. Mogensen, S.C. Singhal, J. Vohs, Nature Materials, 3 (2004) 17-27.

[15] Y. Lin, Z. Zhan, J. Liu, S.A. Barnett, Solid State Ionics, 176 (2005) 1827-1835.

[16] M.R. Ormerod, Chem. Soc. Rev., 32 (2003) 17-28.

[17] B.C.H. Steele, A. Heinzel, Nature, 414 (2001) 345-352.

[18] N. Q. Minh, J. American Ceramic Soc., 76 (1993) 563-588. 277.

[19] G.P. Towler, S. Lynn, Chem. Comm., 155 (1996) 113-143.

Chapter 2

Theory

2.1 Sour natural gas and working with H_2S

An exemplary natural gas consists predominantly of methane (85%), ethane (6%), propane (2%), higher hydrocarbons (< 1%), nitrogen (3%), carbon dioxide (1%) and hydrogen sulfide (0.5%) [1]. However, natural gas has a wide range of compositions, with H_2S content from almost 0% to over 80%. Hydrogen sulfide is the most undesirable of the components of natural gas due to its extreme toxicity and corrosiveness. Natural gas is sweetened before transport and use to minimize the hydrogen sulfide content and undesirable emissions [1].

2.1.1 Working with fuels

- Hydrogen [2]: Hydrogen is an odorless, colorless and tasteless gas. It is flammable and an asphyxiant. The flashpoint is 400 ^{o}C and its flammability range in air is 4-75 vol%. Hydrogen gas is lighter than air and escapes the area at a high vertical velocity.
- Natural Gas (NG) [3]: Methane is a odorless, colorless and tasteless gas used for heating and power generation, and for propulsion in NG vehicles. It is flammable and a simple asphyxiant. The flammability range for methane in air is 5-15 vol%. The auto-ignition temperature is 537 ^{o}C.
- Hydrogen Sulfide [4]: Hydrogen sulfide is a gas with the odor of rotten eggs. Hydrogen sulfide is a flammable, poisonous gas. Its flammability limit in air is 4.3-46 vol% and the auto-ignition temperature is 260 ^{o}C. The odor threshold is 0.1 ppm. At 50-100 ppm it causes eye damage, at 150-250 ppm it paralyzes the olfactory nerves, and 356 ppm is the lethal concentration for 50% of the population (LC50). It is slightly heavier than air.

2.2 Solid state electrochemistry

SOFCs fundamentally function under the rules of solid state electrochemistry, through the solid state defects control conduction of ions and electrons. Below are summarized basic

data on the electrochemistry and the structures of metal oxides that encompass it, which are necessary for engineering oxide anode materials for SOFCs.

Metal oxides (MOs) are ceramic materials composed of ionically bonded cations, alkaline earth (AE), transition metal (TM) and/or rare earth (RE), and oxygen anions. Metal oxides can have a wide spectrum of properties. Electronic and magnetic properties of metal oxides vary greatly, from insulating to metallic conduction, depending on their structures and on the operating temperature. The stoichiometry depends on the valences of the metal cations, which can be varied by changing temperature, pressure and gas composition. Metal oxides can form complex crystal structures due to the ionic forces that dictate separations between cations and anions.

Mixed metal oxides (MMOs) are binary solutions of two metal oxide materials that form thermodynamically ordered structures and complex crystal structures. Their properties are as varied as those of the parent materials. An interesting aspect of MMOs and MOs is the ability to change, alter or adjust properties by adding substituent or dopant elements (metal cations). Aliovalent cations (introduced cation has a different valence than that of the parent cation) can destabilize the structures due to a change in the stoichiometry, as the structure responds by forming non-stoichiometric oxides where charge balance is achieved by incorporation of electrons, holes, vacancies and interstitial atoms or ions.

2.2.1 Bonding

Based on bonding character, ceramics are ionically bonded materials with varying degrees of covalent bonding character. Ionic bonds are formed between two oppositely charged ions, an anion and a cation. Ionic bonding can be described, on a ground state level (uncharged), by the electrostatic (ionic) model. This only serves to describe the ground state of ionic materials and does not give an in depth picture of how the properties of doped ceramics arise. The band model, localized electron model (ligand/crystal field theory) and the chemical bond approach are used to describe these limiting cases [5].

The electrostatic model assumes that electron transfer between cation and anion is complete, leaving no residual electron density. This way the ions can be treated as charged rigid spheres, and the bonding between them is due to electrostatic attraction (balanced by repulsion from the outer electron shells). Born defined the cohesive energy of ionic crystals as [5]:

$$U = \frac{AZ_1Z_2e^2}{R} + \frac{B}{R^n} \tag{2.1}$$

The cohesive energy is a balance between attractive and repulsive forces of two oppositely charged ions (Z_1, Z_2) separated by a distance R; A is the Madelung constant, a characteristic of the geometric arrangement of ions in the crystal; e and B are the repulsion exponent and constant, respectively, a measure of the range and strength of the repulsive interaction [6]. Unfortunately, this model describes the system in the ground state, and not

excited states that give rise to interesting properties of ceramics, such as color and electronic or ionic conduction [6]; in other words, how the oxide responds to external stimuli: stress, temperature, electronic and magnetic perturbances. It also loses its applicability in situations when there are small cations and large anions, which lead to enhanced covalent character of the bonds. Covalent character arises from the overlap of outer shell orbitals of the cation and anion, leading to partial directional bonding. The arrangement of ions is dependent on the strength of the ionic bonds (difference in electronegativity) and the relative sizes of the ions, as discussed in the following section.

2.2.2 Structure

Ceramics are divided by structure type, as all materials are grouped under a prototype material based on their atomic arrangement. Examples include rock salt, fluorites, perovskites, etc. The most common anions in the prototypes are O^{2-}, S^{2-}, F^{-}, and Cl^{-}.

The oxide anion has a filled shell electronic configuration and the radius of the anion varies between 121-128 pm, depending on its coordination [5]. The result is strong ionically bonded, high melting point refractory types of ceramics that are mostly chemically inert at high temperatures. The structures of oxide ceramics can be described by closed packed arrangement of oxide anions with cations placed in tetrahedral and octahedral positions. The exact arrangement between cations and anions within a structure depends on the amount of free space left; therefore knowing the ionic radius of the ions and their coordination in a structure we can approximate the anticipated geometry. See Table 2.1 for a guide [6]. The anion coordination number increases with increasing cation radius resulting in a lower packing density of the unit cell.

Table 2.1: Coordination and geometry as a function of radius ratio

Coordination	r_{cation}/r_{anion}	Geometry
2	0-0.155	Linear
3	0.155-0.225	Triangular
4	0.225-0.414	Tetrahedral
6	0.414-0.732	Octahedral
8	0.732-1	Cubic
12	>1	Cubic

Fluoride, F^{-}, has similar properties to the oxide anion, however is not as chemically inert and its compounds have lower melting points [5]. Sulfide, S^{2-}, is isoelectronic with O^{2-} but, due to a greater spatial extension of the p-orbitals, it shows mixed covalent and metallic bonding [5].

Oxide structures are usually described in terms of a close packed (or nearly close packed) array of oxide ions with metal cations occupying interstitial sites (tetrahedral and octahedral

sites shown in grey in Figure 2.1 below). FCC and HCP types are close packed, with one octahedral site and two tetrahedral sites per oxygen, as shown in Figure 2.1 [7].

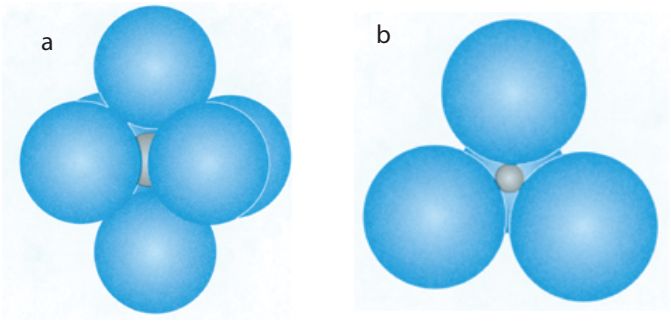

Figure 2.1: a) Octahedral and b) tetrahedral sites.

Of note is the relative size of the tetrahedral and octahedrally coordinated cations: the octahedral site can accommodate a much larger cation. An octahedrally coordinated cation is surrounded by six ligands and can accommodate a cation with a radius equal to 0.414 of the radius of the anion (AX_6) [7]. Octahedra can be visualized or interpreted differently; three different representations are shown in Figure 2.2 below [7].

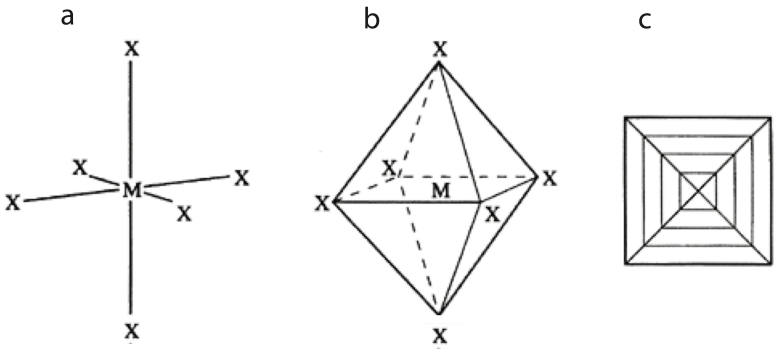

Figure 2.2: AX_6 octahedra presented in different ways.

Tetrahedrally coordinated (tetrahedral) cation sites have four anion ligands and can accommodate a cation with a radius equal to 0.225 of the radius of the anion (AX_4) [7].

$$r_{cation}(octahedral) = 0.414 \cdot r_{anion} \tag{2.2}$$

$$r_{cation}(tetrahedral) = 0.225 \cdot r_{anion} \tag{2.3}$$

Octahedra can be linked via corners, edges and faces. Corner connections provide the most space within the lattice, while faces and edge have the greatest number of shared oxide ions. Figure 2.3 below shows each of the arrangements [7].

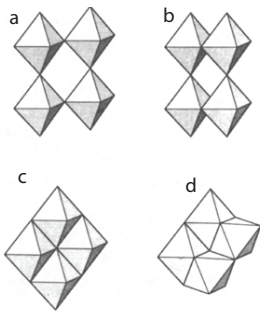

Figure 2.3: AX_6 octahedra: a) corner shared; b) edge shared; c) multiple edge shared; d) face shared.

The following are the most common metal oxide and mixed metal oxide structures [6]; see Table 2.2 for a summary of structures and some examples [8].

AO

Rock Salt (NaCl) - The structure is cubic with a coordination number (CN) of six for both cations and anions. Divalent transition metal oxides all take the rock salt structure (except CuO). TiO, VO and FeO are defect structures, with large numbers of cation/anion vacancies. TiO and VO are metallic conductors, while FeO and CoO are semiconductors.

A_2O_3

Several structures exist for oxides having this chemical formula:

1. (a) Corundum - Intermediate size trivalent cation structures take on the corundum structure, such as Al_2O_3, Ti_2O_3, Cr_2O_3, Fe_2O_3. The trivalent cation can be partly substituted with other valence cations as long as charge balance is maintained.

   (b) II-IV valence pairs ($FeTiO_3$, $MgTiO_3$ & I-V - $LiNbO_3$) - These are ilmenite structures, which is similar to corundum, the difference between the two being only slight and due to the difference in valence and ordering.

2. Rare earth oxides - Larger trivalent cations, such as rare earth (RE) cations, take on three RE-oxide structures.

   (a) A-type is a trigonal structure taken by the large RE cations (La, Nd and actinides Ac and Pu) to form La_2O_3, Nd_2O_3, Pu_2O_3, Ac_2O_3. The unit cell consists of a

Table 2.2: Metal oxide ceramic structures.

Formula	Coordination	Name	Symmetry	Examples
A_2O	2:linear	Cuprite	Cubic	Cu_2O
	4: tetrahedral	Rock salt	Cubic	Na_2O
AO	6: octahedral	Rock salt	Cubic	MgO, NiO
	4: tetrahedral	Zincblende		(no oxides)
		Wurtzite	Hexagonal	ZnO
	4: planar	PdO	Tetragonal	PdO
		Tenorite	Monoclinic	CuO
	4: pyramidal	PbO	Tetragonal	SnO, PbO
A_3O_4	Two B6 (octahedral)	Spinel	Cubic	Fe_3O_4
	One B4 (tetrahedral)			
A_2BO_4	A6 (trigonal)			Al_2MgO_4
	B4 (tetrahedral)			
AB_2O_4	A6 (trigonal)	Inverse Spinel		$MgGa_2O_4$
	B4 (trigonal)			
A_2O_3	6:octahedral	Corundum	Hexagonal	α-Al_2O_3, Ti_2O_3
AO_2	8:cubic	Fluorite	Cubic	ZrO_2, UO_2
	6:octahedral	Fluorite	Cubic	ZrO_2, UO_2
A_2O_5	5+1:distorted	V_2O_5	Orthorhombic	V_2O_5
AO_3	6:octahedral	ReO_3	Cubic	ReO_3, WO_3
	6:distorted	MoO_3	Monoclinic	MoO_3
ABO_3	M6, A12	Perovskite	Cubic or	$SrTiO_3$
	B and A6 (oct)	Ilmenite	Distorted trigonal	$LiNbO_3$
A_2BO_4	B6, A12	Layered perovskite	tetragonal	La_2CuO_4
		(K_2NiF_4)	or Distorted	
$A_2BB'O_6$	B'6, B6, A12	Double perovskites	Cubic or distorted	Sr_2MgMnO_6
ABO_4	B6, A8	Scheelite	Tetragonal	$CaWO_4$
	B6, A8	Zircon-type	Tetragonal	$CeVO_4$

single cation site surrounded by seven oxide ions to form disordered polyhedra. Four cation-oxygen ion distances are shorter than the other three.

(b) Intermediate size RE cations form a B-type structure, of which Gd_2O_3 and Sm_2O_3 are examples. B-type is a highly disordered monoclinic structure.

(c) C-type structure is formed by oxides of the smallest RE cations. It is a cubic structure with a large cell size, similar to the fluorite structure, except that only 3/4 of the anion positions are occupied; thus they have only six fold coordination.

AO_2

Oxides with this structure can take multiple structures: quartz, rutile and fluorite representing four, six and eight fold coordination. Oxides of intermediate size tetravalent cations

take on the rutile structure, which is tetragonal with a single cation site per unit cell which is six coordinated. The prototype is TiO_2 but examples include PbO_2, CrO_2, and SnO_2, while others have a distorted rutile structure: VO_2, MoO_2 and WO_2.

Oxides of large tetravalent metal ions take the fluorite structure, which is cubic. Materials that take this structure include: stabilized ZrO_2, CeO_2, ThO_2, UO_2, PuO_2. The structure is made up of four body centered cubic (BCC) sub-unit cells with a cation in the central atom position in half of the sub cells, surrounded by eight fold coordination. These open cation sites allow facile interstitial substitution. C-type RE oxides are similar to this except that for every eight fluorite cells there are four anions missing which form a ordered array.

Spinels ($\mathbf{A_2BO_4}$)

Spinels, as represented by the prototype Al_2MgO_4, are anionic closed packed cubic structures. The face centered cell contains eight A_2BO_4 units. It can be viewed as having two sets of a tetrahedral and an octahedral unit cell. The anion is interchangeable and the structure is extremely stable. The cations mostly four coordinated (some are six). A and B cations are of similar size. Spinels can be categorized as:

- III-II: Al_2MgO_4, Cr_2FeO_4, Fe_2CoO_4
- II-IV: Mg_2TiO_4, Mg_2GeO_4
- I-VI: Na_2WO_4, Li_2SO_4

Specific site preferences of the cations may force them to assume unexpected positions, resulting in an inverse structure, B_2AO_4.

Perovskites ($\mathbf{ABO_3}$)

The generic formula for perovskite materials is ABO_3 with a large cation, A, in the 12 coordinated site, and an intermediate size cation, B, in the 6 fold site. The A site cations assume face centered atom positions, with B site cations on the edges. Viewed alternatively, there is a (111) array of A and O ions with B ions in octahedral coordinated sites surrounded by O^{2-}. Typically $r_A/r_B > 2$ (r is the radius of the cation with the coordination given above). The stability of the structure is described by the tolerance factor, t:

$$t = \frac{r_A - r_O}{\sqrt{2 \cdot (r_B - r_O)}} \tag{2.4}$$

where r = ionic radii of the respective ions, A,B,O.

The tolerance should be between 0.75 and 1 for a stable structure. In addition to II-IV oxidation state combinations, there are other variations:

- III-III: $LaAlO_3$ $GdFeO_3$;

- I-V: $NaNbO_3$;
- 0-VI: ReO_3 WO_3, MoO_3, each having vacant A sites;

There is a range of oxygen deficient perovskites, some of which have ordered arrangements of vacancies. The properties of perovskites can be adapted to address specific applications due to the large variety of substitutions available. The structures can also be built up to form extended or super structures, Ruddlesden-Popper (RP) and Aurivillius phases. RP phases (eg. Sr_2TiO_4, $Sr_3Ti_2O_7$, $Sr_4Ti_3O_{10}$) consist of several consecutive perovskite blocks, separated by a single NaCl structured block. Aurivillius phases consist of perovskite blocks separated by oxide layers ($Bi_4Ti_3O_{12}$ with Bi_2O_3 layers).

In addition, there are so called double perovskites of the type $A_2B'BO_6$, as two different B site cations are present. This essentially means that four individual perovskite unit cells are put together to form one double perovskite in which every other cell has a different B site cation.

2.2.3 Defects

Defects are present in all materials. In MOs they are responsible for ionic and electronic conductivity through diffusion of charged species. As ceramics are made up of positive and negative ions, the respective charges must be balanced to maintain charge neutrality (in the absence of applied electric fields, or chemical potential gradients). There are several types of defects in ceramics, including:

- Vacant lattice sites (vacancies)
- Ions placed at normally unoccupied sites (interstitials)
- Foreign ions present as either impurities or dopants
- Ions with different charges than those of the base material stoichiometry
- Shear planes

Point defects are the most basic types of defects; they are one dimensional and consist of missing atoms or ions, or atoms and ions placed in interstitial or substitutional positions. In ceramics, to ensure charge neutrality, point defects arise in pairs (unless the material is nonstoichiometric). Two of the most common point defects in ceramics are: Schottky defects, in which a cation-anion vacancy pair are present in the ionic lattice; and Frenkel defects, in which either an anion or cation vacancy and interstitial pair are present in the ionic lattice.

Kröger and Vink introduced a notation to describe defects in ceramics. Kröger-Vink notation consists of the following terms [9]:

$^{\bullet}$: positive charge; ' : negative charge; x : uncharged; MX : M cation, X anion

Table 2.3: Kröger-Vink Notation

Function	Notation
Vacant M site	V_M"
Vacant X site	$V_X^{\bullet\bullet}$
Ion on lattice site	M_X or X_X
L on A site	L_M'
N on A site	$N_A^{\bullet}$
Free electron	e'
Free hole	$h^{\bullet}$
Interstitial A ion	M_i $^{\bullet}$
Interstitial X ion	X_i"

Extended defects, such as dislocations and grain boundaries, are also present in metal oxides and are governed by the same charge neutrality rules. Grain boundary areas are non-stoichiometric due to the disorder present, especially at high angle grain boundaries.

Defects can be introduced into the lattice under conditions of thermodynamic equilibrium; these defects are called intrinsic defects. Vacancies are one example because their concentration depends on temperature, with vacancy concentration increasing with temperature (a reversible process). Extrinsic defects are induced in a material by introducing foreign ions into the host ionic lattice or through non-stoichiometry. The material must offset the charge imbalance due to these defects by introducing vacancies (cation or anion), electrons or holes. These create a nonstoichiometric compound, which will introduce further defects into the lattice because the defects offset the charge imbalance that occurs as a result. Electronic defects arise due to transition of electrons from the valence band to the conduction band, which introduces a hole (or electron hole) in the valence band. In ionic crystals these electrons and holes travel from one ion to the next giving electronic conduction (p or n type semiconductor or metallic). See § 2.2.4 for further discussion.

Table 2.4 lists the 4 types of non-stoichiometry present in oxides [7].

Table 2.4: Types of non-stoichiometry in oxides

Meta Excess (reduced metal)		Metal Deficiency (oxidized metal)	
A: anion vacancies	MO_{1-x}	C: interstitial anions	MO_{1+x}
B: interstitial cation	$M_{1+x}O$, CdO, ZnO	D: cation vacancies	$M_{1-x}O$ TiO

In type A and B oxides extra electrons compensate charge for the excess metal in the structure. These electrons, which are not bound, lead to metallic or n-type conductivity. In C and D type oxides metal deficiency is compensated by holes, inducing p-type conductivity.

Holes are associated with M^{z+} centers and, while not as mobile as electrons, they travel in the opposite direction.

Highly defective materials can reorder spontaneously through a crystallographic shearing mechanism, similar to a martensitic transition in metals. When vacancies aggregate along a lattice plane the lattice shifts uniformly to eliminate an entire row of vacancies [7]. They are present in most d^o oxides (V_2O_5, TiO_2, MoO_3, WO_3) when these are exposed to a reducing environment. This will, in effect, change the structure locally and remove the vacancies in the process.

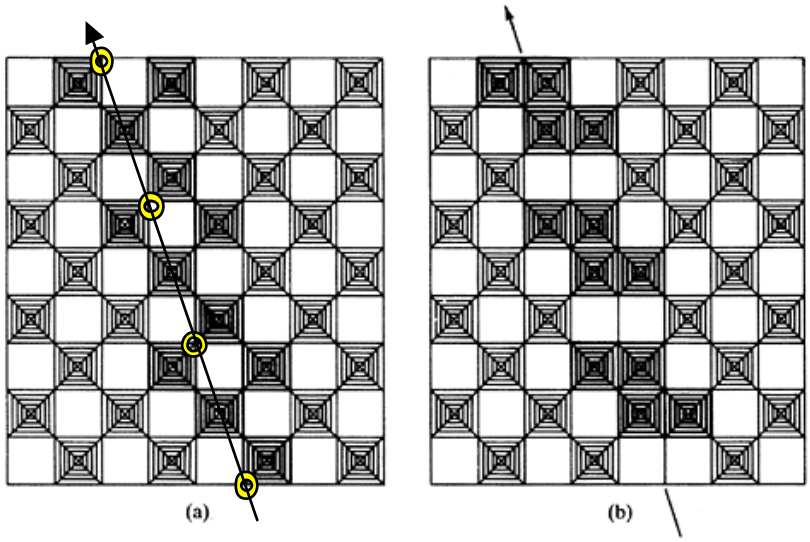

Figure 2.4: Crystal lattice: a) with vacancies (yellow circles), b) after elimination of vacancies by shear mechanism

.

2.2.4 Conduction

Electronic conduction

Three different electronic conduction mechanisms exist:

- Metallic - Metals have no band gap between the valence band and the conducting band. Therefore, electrons can easily travel along the band conducting electricity.

- Semiconductor- Semiconductors have an intermediate size band gap between those of metals and insulators (0-5 eV). They can be doped to produce either n (negative) or p (positive) -type conductivity; in either case there is an overall increase in conductivity due to the insertion of a donor or acceptor level within the band gap which facilitates the transfer of electrons. They can be n-type if the charge carrier is an electron, or p-type if the charge carrier is a hole.

- Insulator - Insulators have large band gaps (> 5 eV), and are electronically insulating.

Metal oxides have a variety of electronic properties in the material world as they can be semiconductors, conductors and insulators. Their properties can change drastically over a range of temperatures (superconductivity, insulator-metal transitions), or over a composition range, and can be amended with doping. In the following section theory on metal oxides in relation to their electronic properties is presented, and related to band theory.

The band structure theory of ceramics, provides a description of the electronic conductivity in ceramics. Band theory allows for delocalization of electrons in contrast to their bound states in bonding theory, allowing for a description of transport properties such as electrical conductivity, requiring energy and momenta for all states. Band theory assumes that there is an overlap of outer orbitals of cations and anions, enough so that their valence electrons are shared and completely delocalized or itinerant (free to move, as in metallic conductors) [6]. The wave functions of the outer electrons overlap to form a continuum of states throughout the crystal. These are called energy bands due to the requirement that electrons must not have the same spin direction and energy. For insulators and semiconductors there is a gap between the lower set of bands and the higher, and this gap is called the band gap. Metals do not have an appreciable band gap. The band below the band gap is the valence band, and the one above it is the conduction band. The Fermi energy E_f is the highest occupied energy level, and there are no free electrons above this energy. The Fermi energy is in the conduction band in conductors and within the band gap for semiconductors and insulators. See Figure 2.5 below for band diagrams illustrating different types of materials; filled boxes are filled valence bands, white boxes are empty conduction bands [10]. The band gaps are marked for each band diagram. Type b) metals do not have a band gap, as the conduction band overlaps the valence band. d-orbital bands are typically described as being very narrow, and degenerate, meaning they are of the same energy. The width of the d band decreases across a period, increased down a group and with increasing temperature. The properties of TM cations are largely determined by the d-band structure [11].

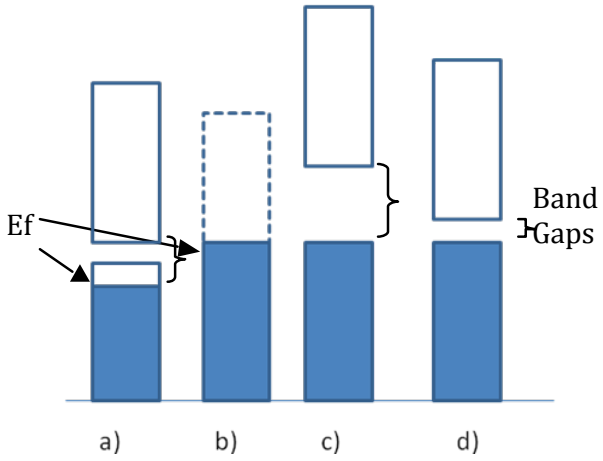

Figure 2.5: Band structures of materials a) d-metal, b) sp-metal, c) insulator, d) semiconductor.

The model derived from band theory works best with s- and p-orbital bonding. However d-orbital states are more complicated, and the situation in binary as well as mixed cation cases is more difficult to model mathematically. f-orbitals, such as those of RE cations or atoms, are generally considered to be non-conducting. A combined approach using crystal field splitting and band theory does a better job, but the chemical bonding approach developed by J.B. Goodenough especially for mixed oxides is more comprehensive [6, 12].

Ionic conduction

Generally speaking, there is essentially one type of ionic conductivity, when ions carry current. However, it can be broken down into cationic (eg. H^+, Na^+) and anionic conduction (eg. O^{2-}, F^-, Cl^-). Conductivity of ions occurs by diffusion of the species in question through the electrolyte material. Some ceramics are natural ionic conductors, and in all cases aliovalent doping initally increases the ionic conductivity by creating vacancies, thereby increasing the number of diffusing (conducting) species. When vacancies are present in the material, the conducting ion can migrate through the electrolyte by hopping to an adjacent vacancy. The diffusion current (J) of species i is increased by the application of a potential gradient (dV/dx) across the membrane, and an increased concentration gradient (dC/dx) [13]:

$$J_i = -\frac{M_{i\mu} RT}{c_i}\frac{dC}{dx} - M_{i\mu} z_i F \frac{dV}{dX} \tag{2.5}$$

where $M_{i\mu}$ is a diffusion coefficient dependent constant specific to each ion.

Essentially, the process can be considered as vacancies traveling in the opposite direction to a conducting ion through the material. When there are no applied potentials or chemical gradients, species will diffuse via random motion called random walk.

2.3 Fuel cell fundamentals

The simplest SOFC reaction is the oxidation of hydrogen, for which the overall reaction is shown in (2.6):

$$H_2 + 0.5O_2 = H_2O + electricity + heat \tag{2.6}$$

A fuel cell is made up of three principal components: anode, cathode and electrolyte. These are shown schematically in Figure 2.6.

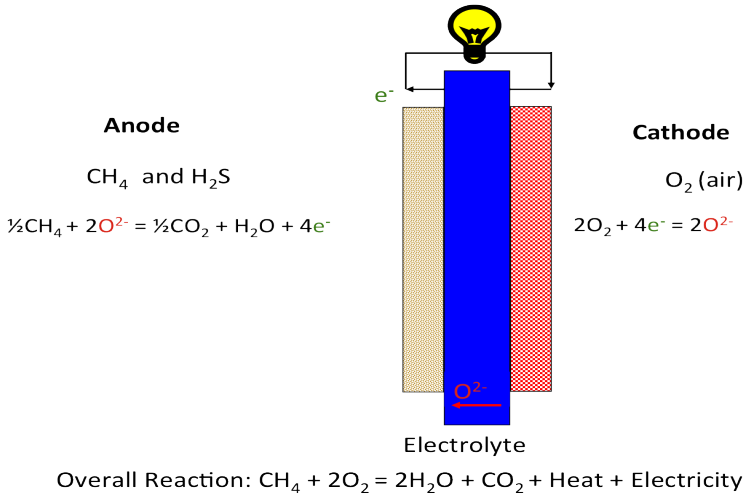

Figure 2.6: Schematic of a fuel cell.

The overall reaction is split into two reactions (Eqn 2.7) and (Eqn 2.8) occurring simultaneously at the anode and cathode, respectively:

$$H_2 + O^{2-} = H_2O + 2e^- \tag{2.7}$$

$$0.5O_2 + 2e^- = O^{2-} \tag{2.8}$$

In an oxide ion conducting SOFC the electrolyte serves to conduct oxygen anions from the cathode to the anode through ionic conduction. When the electrons are conducted from the anode to cathode through a load in an external circuit, the electrons do useful work. The heat provided from the exothermic reaction can be used to sustain the cell at operating temperature, and to preheat the reactant gases. The free energy (ΔG) of reaction (2.6) is directly related to the potential available from the reaction, which is called the cell electromotive force (EMF), or open circuit potential/voltage (OCP or OCV or E^o), as [13]:

$$\Delta G = -nFE^o \tag{2.9}$$

where n = number of electrons and F = Faraday's constant.

OCV describes the state of the system at perfect thermodynamic equilibrium under standard conditions (T and P). As mentioned above, any combustible gas can be used as a fuel, and each reaction will have a different OCV. These are discussed in § 3 below.

A fuel cell's theoretically maximum performance is determined by several factors: reactants and their partial pressures, temperature and external electric field, as described by the Nernst equation (2.10) [13]:

$$E = E^o - \frac{RT}{nF} \ln \frac{p_{product}}{p_{reactant}} \tag{2.10}$$

The actual performance is determined by measuring the current and voltage of the fuel cell which reveal such information as the available energy for reaction, maximum power attainable, fuel utilization, and parasitic losses [11]. While sacrificing a portion of the thermodynamically available cell voltage (E^o, determined by the Nernst equation), a net current is produced from the fuel cell [13], resulting from an increase in the rate of the forward reaction (desired) by decreasing the energy barrier for the reaction. The main types of losses (also called polarization) present in fuel cells are activation (η_{act}), ohmic (η_{ir}), and concentration (η_{conc}) losses. Additionally, there can be a small potential loss due to electrolyte leakage (E_L) [2]. Activation polarization is due to kinetic limitations of the charge transfer reaction at the electrode surfaces (anode and cathode) [13]. Ohmic loss is due to the resistance to charge flow of electrons in the electrodes and of ions through the electrolyte, and contact resistances. Concentration polarization is due to mass transport limitations at high currents.

$$E_{cell} = E^o - E_L - \eta_{ir} - \eta_{act} - \eta_{conc} \tag{2.11}$$

where E_{cell} is the overall cell voltage.

The kinetics of the fuel cell reaction is directly related to the current provided from the cell (the rate of the reaction). The Butler-Volmer equation (2.12) shows the relation between the reaction rate as shown by the exchange current density (i_o) and voltage (specifically overvoltage or applied voltage as η) [13]:

$$i = i_o(exp^{(\frac{-\alpha F n \eta}{RT})} - exp^{(\frac{-(1-\alpha) F n \eta}{RT})}) \tag{2.12}$$

The first part of the expression is for the forward reaction, while the second part is for the reverse reaction. When an overvoltage is applied we push the forward reaction. The transfer coefficient, α, describes the symmetry of the forward and reverse reaction. It has a value between 0 and 1; 0.5 would represent a symmetric reaction.

The power produced by the cell is obtained by multiplying the current and voltage, $Power = E_{cell} \cdot i$. Current and power usually are reported as area specific values; current density and power density, which are obtained by dividing the current by the geometric area of the electrode.

The fuel cell efficiency can be defined in several ways. The thermodynamic efficiency (2.13) depends on the free energy and enthalpy of the reaction, and this depends on the reactants, products and temperature:

$$\varepsilon_{thermodynamic} = \frac{\Delta G}{\Delta H} \tag{2.13}$$

The real efficiency of the fuel cell, ε_{real}, is the product of $\varepsilon_{thermodynamic}$, $\varepsilon_{voltage}$ and $\varepsilon_{fuelutilization}$:

$$\varepsilon_{real} = \varepsilon_{thermodynamic} \cdot \varepsilon_{voltage} \cdot \varepsilon_{fuelutilization} \tag{2.14}$$

where $\varepsilon_{voltage}$ is due to irreversible losses to the ideal voltage as a result of the withdrawal of current (application of overvoltage):

$$\varepsilon_{voltage} = \frac{V_{cell}}{E^o} \tag{2.15}$$

and $\varepsilon_{fuelutilization}$ is due to fuel exiting the fuel cell without reacting or undergoing secondary reactions that do not generate power:

$$\varepsilon_{fuelutilization} = \frac{i/nF}{\nu_{fuel}} \tag{2.16}$$

where ν_{fuel} is the flow rate of the fuel.

2.3.1 Electrochemical measurement techniques

The fuel cells employed in this thesis are single cells called button cells, owing to their likeness to buttons. Figure 2.7 represents a schematic of the button cell with approximate dimensions, while Figure 2.8 shows the entire setup with the current collectors and manifolding (gas conducting) system. A description of the setup is provided in § 4.

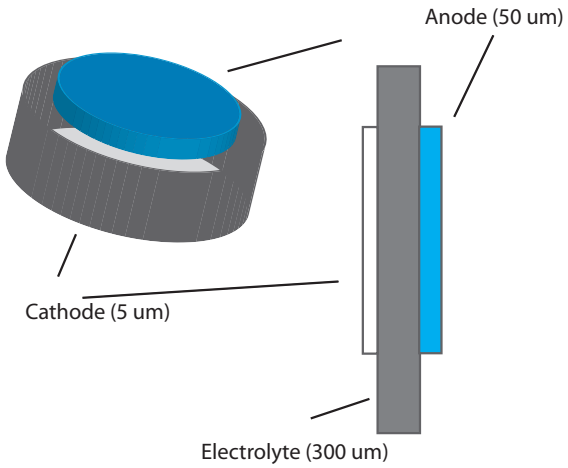

Figure 2.7: Schematic of button cell MEA.

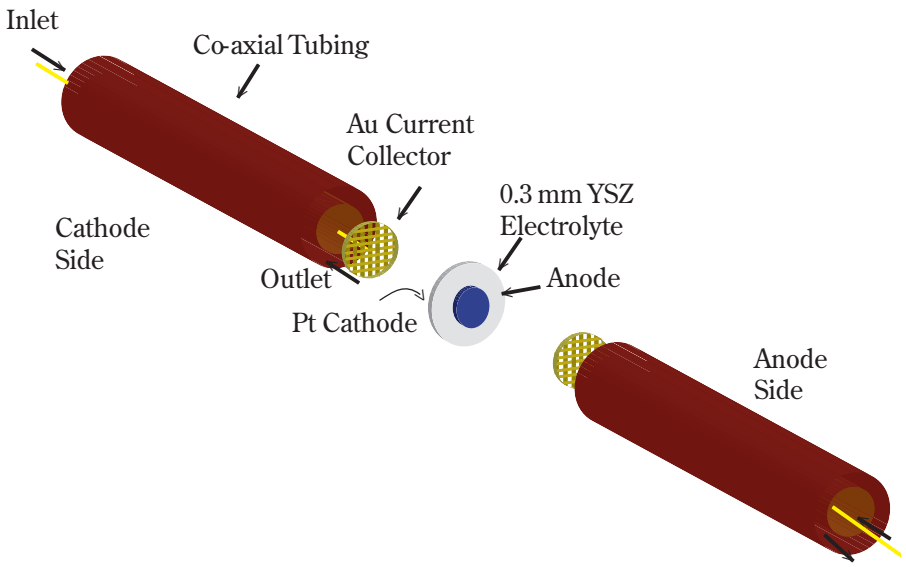

Figure 2.8: Exploded schematic of the testing setup.

The following electrochemical measurement techniques were employed in this work.

Potentiodynamic/Galvanodynamic

In this technique the current or voltage is linearly cycled between two points, while the voltage or current response from the cell is measured. Potentiodynamic measurements are cycled from OCV to 0 V while measuring the current drawn to obtain fuel cell performance data (i-V and P-V). Galvanodynamic measurements are ramped from 0 amps to whatever current value results in a cell voltage of 0 V at the end of the current sweep.

Potentiostatic/Galvanostatic

These two techniques are used to determine time dependent performance under conditions of constant current or voltage withdrawal. The voltage or current is set at the desired point, and the complementary variable is measured versus time. These tests are ideal for long-term stability measurements.

Electrochemical impedance spectroscopy (EIS)

This is a powerful electrochemical characterization technique that allows for the determination of polarization losses occurring in the fuel cell [14]. This technique differs in that it is an AC technique, that may or may not have a DC signal applied simultaneously with the AC signal. The AC signal is perturbed at interfaces in the fuel cell system and thus offsets the AC wave. The magnitude of this offset is used to determine the polarization losses.

Conductivity

Conductivity measurements are performed on dense pellets of the material. There are several different arrangements with which to measure the conductivity, but only two are suitable for testing electrode materials due to their high electronic conductivity. These are both based on DC polarization, in which the pellet is cycled galvanostatically or galvanodynamically and the resistance is obtained from the relation $R = V \cdot i$. The first is a simple two electrode setup applied to the sides of the pellet. The second is called the van der Pauw method, in which four point electrodes are contacted on the surface of the pellet and the resistance is measured between the four points. The thickness and area of the contacts are taken into consideration using the following relations [15]:

- Two electrode
$$\rho(\Omega \cdot cm^{-1}) = R \cdot \frac{Area}{thickness} \tag{2.17}$$
- van der Pauw
$$1 = exp^{(\frac{-\pi dR_1}{\rho})} + exp^{(\frac{-\pi dR_2}{\rho})} \tag{2.18}$$

Electrode setup

Fuel cell measurements can be conducted in a variety of electrode configurations:

- Two electrode: In this electrode setup there is no reference electrode, and the measurements are conducted versus the counter electrode (cathode). In this configuration the cathode and anode each have a current collector attached with one or two leads (wires) per current collector, which serve to supply and withdraw the current and to measure the voltage. If one lead is used, the voltage leads are connected outside of the hot zone of the cell, which simplifies the setup. However, all electrochemical measurements are affected by the resistance of the wires. The contribution of the wires can be measured externally and manually subtracted from the measurements. A two probe setup is preferred since it allows for simultaneous measurement of current and voltage. In this thesis, all fuel cell measurements were conducted using a two electrode-single lead configuration.
- Three electrode: In a three electrode configuration a third, reference electrode is added to the cell on either the anode or cathode side and is used to maintain a constant OCV

between the reference and counter electrode. In a solid state electrochemical system it is difficult to place the third electrode in an appropriate location. There are several references which discuss reference electrode placement [14, 16, 17].

- Four electrode: A four electrode setup will have two reference electrodes, one on the anode side and one on the cathode side. This allows characterization of the complete fuel cell system, however the large number of electrical connections make it very hard to perform reliable and repeatable measurements.

2.3.2 Fuel cell components

Anode

The function of a heterogeneous catalyst is to increase the rate of a reaction by providing a pathway with a lower activation barrier to the reaction, without affecting the state of the catalyst itself [5]. Heterogenous catalysts are used in the chemical industry to more rapidly convert reactants to products, such as in the production of fertilizer from N_2 gas. It is a not an electrochemical process and the rate of the reaction is strongly affected by temperature and catalyst activity. An electrocatalyst is used in electrochemical reactions, and needs to be conductive so as to allow transfer of electrons and ions. The fundamental difference between electrocatalysis and heterogeneous catalysis is that the reaction occurs in two half cells; in other words the anodic and cathodic reactions each occur on its own distinct catalyst [5]. Electrocatalysis is the heterogeneous catalysis of a charge transfer reaction across an electrode-electrolyte interface. The reaction rate is a function of catalytic activity of the catalyst, which depends on the effectiveness of adsorption in reducing the reaction activation energy. The rate is also influenced by the presence of the electric field as well as the nature of the electrolyte. Each electrocatalyst also has a wide range of requirements. The following are the requirements for an SGSOFC anode catalyst [18]:

- Electrochemical performance - fuel activation: The catalytic performance of the potential catalyst is the most important initial criterion because, if the material is presumed not to be catalytic (e.g., electrochemical methane oxidation), then it is of no use. Since the electrocatalytic oxidation of methane closely resembles the catalytic oxidation of methane, materials that are used as catalytic oxidizers provide a good initial testing options. Oxidation at the catalyst surface represents a reversible (dynamic) process in which the coordination number (CN) and oxidation state of the central atom are changed [2]. In the case where we can assume that only the surface of the metal oxides participates in the reaction, the ability of the central atom to have flexibility in CN and oxidation number and to cycle between reduced/oxidized is critical. This can be extended to mixed metal oxide structures in which the surface will be a combination of AO and BO sites, the ratio and CN of which will depend on the crystal structure of the surface.

- An important aspect of electrochemical performance is the concept of a triple phase boundary (TPB) in fuel cell catalysis, since the reaction requires three phases in contact for the reaction to occur which involves transport of gas, electrons and ions. The anode catalyst must provide access for all three. If the anode catalyst is a composite of several materials that contribute either ionic or electronic conduction, but not both, the reaction will occur only at the interface between the particles, the TPB. Activity of single phase mixed conducting electrocatalyst is not limited to a TPB.

  As a general rule, the activity of a electrocatalyst can be defined for the SGSOFC as having a polarization resistance of $< 0.2\ \Omega\ \mathrm{cm}^{-2}$ by AC impedance.

- Electronic conductivity ($\sigma_{electron} > 1\ \mathrm{S\ cm}^{-1}$): The electrocatalyst must be or include an electronic conductor. A p- or n-type conductor is acceptable, but metallic conductors are preferred. The better the electronic conduction the lower will be the resistance of the fuel cell. An additional benefit would be if the electrode material is also an oxide and/or proton conductor in addition to being a electronic conductor; these materials are called mixed ionic electronic conductors (MIECs). MIECs have overall the best properties and the best performance in fuel cell environments because they decrease contact resistance and stability problems due to the use of different materials on the anode side (such as separate electronic and ionic conductors that have incompatible thermal expansion coefficients), and the reaction sites are not limited to TPBs.

- Oxygen anion conductivity ($\sigma_{ion} > 0.1\ \mathrm{S\ cm}^{-1}$): The electrocatalyst must also be or include a ionic conductor, again to ensure an adequate number of TPB sites. Composite electrodes contain a oxygen anion conductor as one component, while MIECs conduct ions in addition to electrons; typically only a small portion of the total conductivity is ionic.

- Chemical stability in H_2S: This criterion relates to a material's resistance or oxidation capability to hydrogen sulfide. Since in sweet NG, H_2S is found only in trace amounts ($<$ 5ppm) it will not provide a lot of power through its oxidation, although if it does oxidize it will be better since SO_2 or S are products more easily removed from the product stream. For NG having high concentration of H_2S the majority of the power can be derived from H_2S oxidation.

- Chemical stability in oxidizing and reducing conditions: Reduction occurs at the anode, oxidation at the cathode. The material at the cathode must be stable in oxidizing conditions up to oxygen partial pressures of 1 atm. The material at the anode must be stable in reducing conditions under low oxygen partial pressures i.e., $P_{O_2} < 10^{-8}$ [19].

- Comparable thermal expansion of MEA components (with YSZ CTE≈11 x 10^{-6} K^{-1}): The anode material must be compatible with YSZ; it should not react or have solid state reactions with YSZ at the fuel cell operating temperatures or below (950 ^{o}C). Up to 1400 ^{o}C would be the most desirable to allow for a good sintering procedure to be followed. Thermal stability is determined by comparable thermal expansion coefficients (α or CTE) of the anode material with the electrolyte. The CTE is the dimensional expansion a material experiences with increase in temperature. A large CTE mismatch would result in cracking or delamination of the fuel cell with increase in temperature.

Electrolyte

The SOFC electrolyte must be: an adequate O^{2-} conductor; have very low electronic conduction under oxidizing and reducing conditions; and it must be mechanically stable under reduction-oxidation (redox) condition. The most commonly used SOFC electrolyte is yttria-stabilized zirconia (YSZ, $Zr_{0.85}Y_{0.15}O_{1.925}$), because it satisfies those requirements. Zirconia (ZrO_2) is doped with yttria (Y_2O_3) for two reasons: first, it stabilizes the high temperature cubic phase of ZrO_2 down to room temperature; second, it generates oxygen vacancies, increasing the ionic conductivity as Y^{3+} replaces Zr^{4+} in the fluorite crystal structure. Using Kröger-Vink notation, the process is illustrated as:

$$Y_2O_3 \xrightarrow{ZrO_2} 2Y'_{Zr} + 3O_o + V_o^{\bullet\bullet} \tag{2.19}$$

Two fairly new electrolytes have been proposed that have superior conductivity and would be suitable for operation at lower temperature: 10 mol% Gd_2O_3 doped CeO_2 (GDC or CGO) and $La_{0.8}Sr_{0.2}Ga_{0.83}Mg_{0.2}O_{3-\delta}$ (LSGM)[19]. However, the chemical and thermal expansion compatibility of LSGM have not been fully explored, and it has not yet been used extensively. CGO is a mixed conductor under low oxygen partial pressure, which makes it a poor choice of electrolyte for use above 800 ^{o}C, as it decreases the OCV. The mixed conductivity makes it a good additive for composite anodes as it increases the TPB extent. Figure 2.9 compares the conductivities of various O^{2-} conducting electrolytes [14].

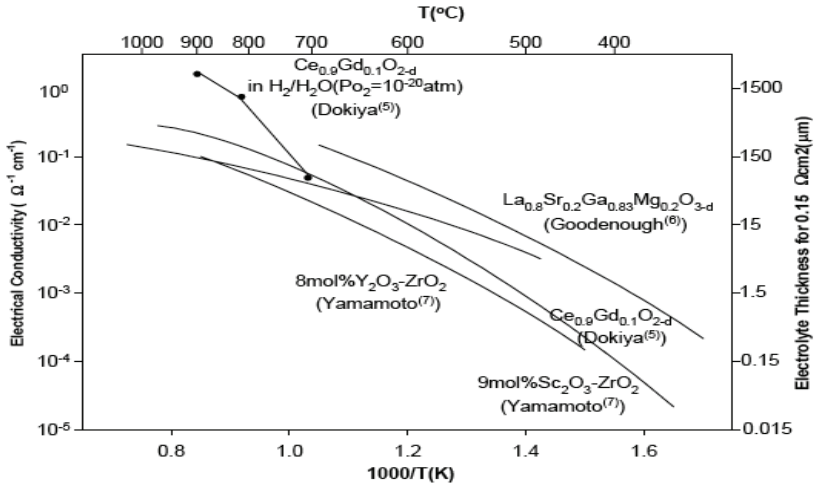

Figure 2.9: Electrolyte conductivity as a function of temperature.

Cathode

The SOFC cathode shares some of the same requirements as the anode, except that it must be active towards the reduction of the oxidant and must be chemically stable under high oxygen partial pressures. Platinum (Pt) and other noble metals were used as early cathodes, however they have since been abandoned in commercial units because of chemical or physical instability and incompatibility with most electrolytes, or because of the high cost [20]. Frequently, Pt is used in small scale cells due to ease of deposition and high reproducibility; for these reasons Pt is used exclusively as the cathode in this thesis.

The state-of-the-art cathodes of today are lanthanum-based perovskites, primarily $La_{0.8}Sr_{0.2}MnO_3$ (LSM). LSM is characterized by satisfactory chemical stability, electronic and ionic conductivity, electro-catalytic activity, and excellent thermal-expansion match with YSZ. LSM is a p-type conductor at high oxygen partial pressures, following reaction 2.20:

$$LaMnO_3 \xrightarrow{SrO} La^{3+}_{1-x}Sr^{2+}_{x}Mn^{3+}_{1-x}Mn^{4+}_{x}O_3 + h^{\bullet} \tag{2.20}$$

There are no interactions with YSZ at temperatures below 1200 ^oC; however, above this temperature a detrimental insulating phase, $La_2Zr_2O_7$, is formed between YSZ and LSM [20].

The ionic and electronic conductivities of LSM are adequate at high temperatures; its ionic conductivity is lower than YSZ and its electronic conductivity is lower than $LaCrO_3$ (interconnect material). This becomes a problem for low-temperature operation ($< 700\ ^oC$), and so other cathode materials must be considered, such as strontium-doped lanthanum ferrite, $La_{0.7}Sr_{0.3}FeO_3$ (LSF), strontium-doped lanthanum ferro-cobaltite $La_{0.7}Sr_{0.3}Co_{0.6}Fe_{0.4}O_3$ (LSCF), and $SrCo_{0.4}Fe_{0.6}O_3$ (SCF) [14].

2.3.3 Catalytic properties

Catalysts accelerate the rate of a reaction without changing its equilibrium; they can affect kinetics but not thermodynamics. Oxide materials are used as both catalysts and as catalyst supports in heterogeneous catalysis (e.g., Fisher-Tropsch, automobile exhaust converters), electrocatalysts and gas sensors. Non-transition metal oxides are good acid-base catalysts while TM oxides are good acid-base and redox catalysts [6]. Metallic oxides can be used as electrocatalysts, as long as their electronic and ionic conductivities are adequate, in addition to possessing catalytic activity. Thus the following discussion will deal mainly with metal oxides as heterogeneous catalysts.

Chemisorption and physisorption

The first step in the catalytic process is adsorption of the reacting molecule onto the surface of the catalyst. The molecule may be physisorbed or chemisorbed. Physisorption is adsorption of an atom or molecule on the surface; the bond formed is a very weak van der Waals bond, and so essentially the adsorbate is not firmly bonded to the catalyst. Chemisorption requires more energy to occur and the adsorbate is strongly bonded to the surface. Once adsorbed the reactant molecule forms an intermediate species by either dissociation or association and then desorbs as product from the surface. A catalyst material has active sites on its surface, onto which the reactant adsorbs. These active sites are typically particular metal atoms, or specific defect sites on the surface of the metal atoms (e.g., steps, edges etc.). In metal oxides these active sites can be cations, anions and vacancies.

Reactivity of the surface sites

Since the catalytic reactions only occur on the surfaces of the catalyst (in heterogenous catalysis and electrocatalysis) the reactivity of the surface is of paramount importance to the reaction being promoted. The composition of the surface of a metal oxide is different from that of a pure metal: metal surfaces only contain a single species; while metal oxide surfaces have at least two species (cation and anion), and the composition of the exposed surface can vary with the particular plane that makes up the surface.

The reactivity of an oxide surface varies with the oxidation state of the cation, the exposed surface plane and the saturation of coordination sites. This is due to changes in the electronic state of the cations. Missing atoms on the surface of catalyst increase the reactivity of the surface. The greater the number of missing neighbors the higher the reactivity; these surfaces are termed coordinatively unsaturated sites (CUS). Oxide surfaces can be polar and non-polar depending on the ions present on the plane of the surface, even at full coordination. For example a MgO (111) surface is polar with either a fully cation or fully anion surface, while the (100) and (110) planes are non-polar containing equal amounts of cations and anions [8]. Polar surfaces typically are more reactive than non-polar surfaces.

In Figure 2.10 below, is a schematic of the surface of a $LaXO_3$ perovskite showing the (100) and (111) planes.

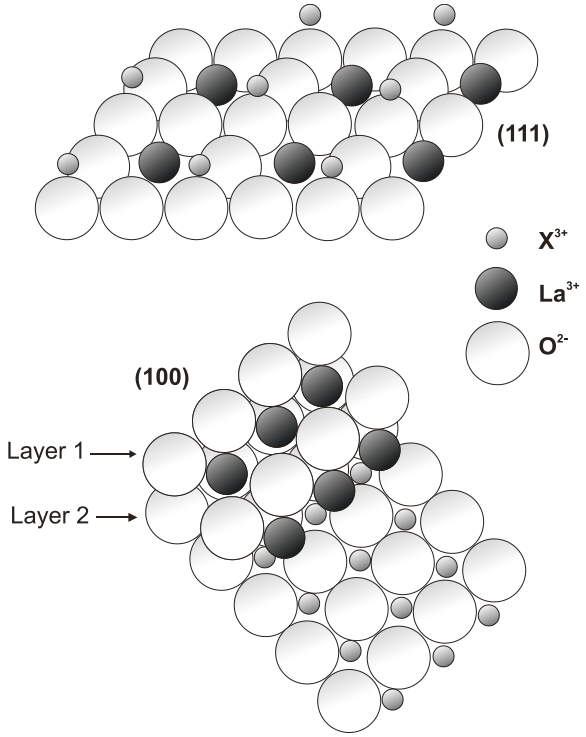

Figure 2.10: Surfaces of the model perovskite $LaXO_3$.

Nucleophilic vs. electrophilic reactants

Once a molecule is chemisorbed on the surface of a metal oxide, bonds must be broken for a reaction to occur [21]. Specifically, to activate a hydrocarbon, the anion participates by removing H from the molecule. O^{2-} has no oxidizing properties; it is a nucleophilic reactant which extracts H from hydrocarbon molecules. O_2^- and O^- are electrophilic reactants, which extract electrons from the catalyst surface and then H from hydrocarbons. The electrophilic reactant is activated by the potential addition of electrons from the hydrocarbon molecule. It is not known whether an oxide fuel cell electrocatalyst is nucleophilic or electrophilic.

Cations are usually oxidizing agents. Mixed oxides are used in conventional catalysis in order to accelerate regeneration (reoxidation) of the active centers. One redox pair participates in the oxidation of the hydrocarbon and the second pair mediates the reoxidation of the catalyst by gas phase oxygen. An example is the Fe^{2+}/Fe^{3+} couple. An oxide fuel cell electrocatalyst participates in similar manner, except that the O^{2-} comes from the bulk of the catalyst, not the atmosphere. Redox capable cations are required for the reaction to proceed.

Redox catalysts: oxidation state of cations at the surface

The oxidation state of cations is important for surface reactions [8]. In redox reactions the cation must be reduced and then oxidized due to the acceptance or transfer of electrons from the adsorbate. Therefore, the cation must have at least two oxidation states and it must start off and end in the oxidized state. Consequently, d^o cations are inert. For any specific ion, the lower oxidation state, the greater is $d^{n>0}$, and the greater is the reactivity. However, if the cation is too reactive there is a danger that it will adsorb the molecule too strongly, resulting in poisoning.

Acid-Base catalysts: acidity of the surface

Acid-base catalysis does not involve direct electron transfer [8]. In acid-base catalysis cations at the surface are Lewis acid sites because they are electron acceptors. Anions are Brönsted bases because they are proton acceptors. This is an extension from the formal definition of Lewis acid as electron acceptor and base as electron donor: a Brönsted acid is a proton donor, and a Brönsted base is a proton acceptor. From this definition vacancies are good adsorption sites being either Brönsted acids or bases. Molecules such as NH_3 and H_2O have lone-pair electrons making them donors of electrons (Brönsted bases) and react with acceptors (Brönsted acid sites) [8].

As a result fuel cell electrocatalysts do not work on an acid-base catalyst reaction path; however secondary reactions such as carbon deposition may be related to the acidity or basicity of the surface.

Adsorption of an atom

It is interesting to discuss adsorption from the perspective of bonding between the catalyst surface (band structure) and the energy levels of the adsorbate.

In the case of sp-band metals, an adsorbate atom with two energy levels approaches a free electron metal having only sp orbitals at the surface [22]. As the adsorbate approaches, its energy levels broaden and shift down in energy, Figure 2.11.

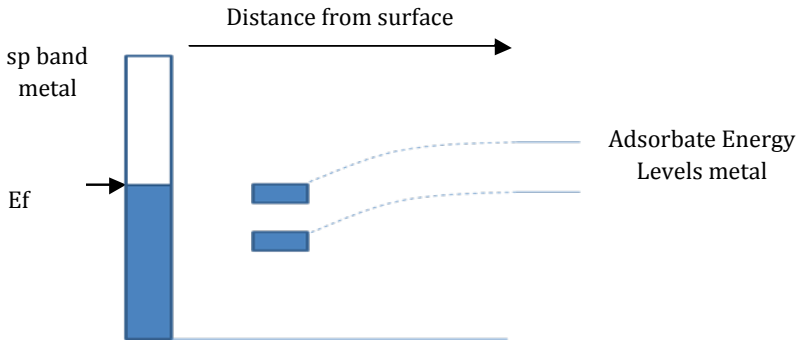

Figure 2.11: Adsorption of an atom on a sp orbital cation

Similarly the d-band causes splitting of the adsorbate energy levels into bonding and antibonding levels which shift and broaden, Figure 2.12 [22]. Filling of the antibonding orbitals weakens the bond, and the orbital will be occupied only as long as it is below the Fermi level of the metal [22].

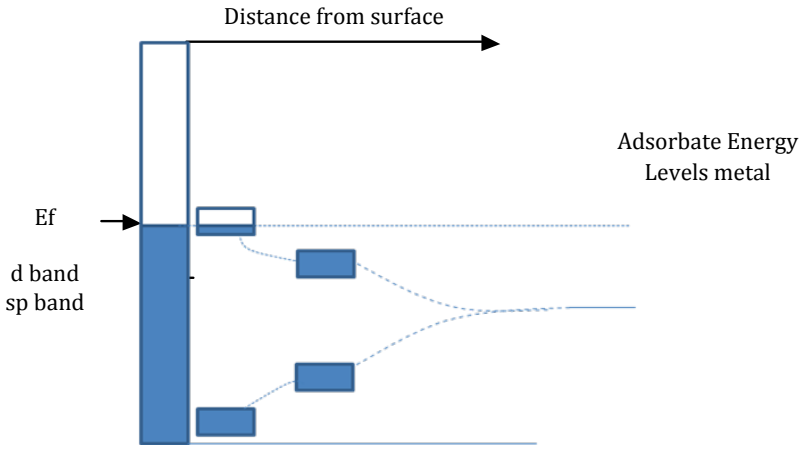

Figure 2.12: Adsorption of an atom on a d orbital cation

Adsorption of a molecule

The process for adsorption of molecules (have bonding and antibonding orbitals) is the same as described above, with the exception of bond splitting of both orbitals. In this case both the bonding and antibonding orbitals of the molecule contribute to the chemisorption bond [22]. Filling of the antibonding orbital results in weakening of the intramolecular bond of the adsorbate and dissociation of the molecule [22].

Stress and strain change the reactivity of the surface as well. While they don't affect the degree of filling of the d orbitals, their width and center change.

One can also look at adsorption on the surface in terms of the split d orbitals. Depending on the number of electrons in the d band and orbital filling, and recalling that the number of t_{2g} and e_g orbitals also depends on the coordination of the oxide, the adsorbate will primarily affect the lower energy t_{2g} orbitals to which it bonds weakly because the orbital overlap will not be as good [8]. If the cation has e_g orbitals they will bond strongly to the adsorbate [8]. This is illustrated in Figure 2.14 below [8].

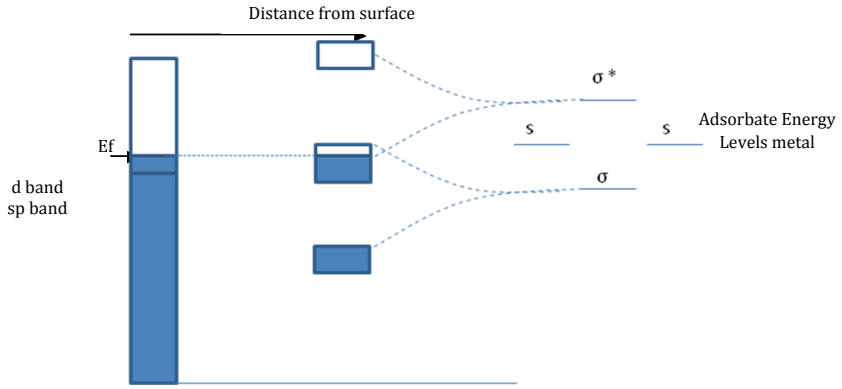

Figure 2.13: Adsorption of a molecule on a d orbital cation

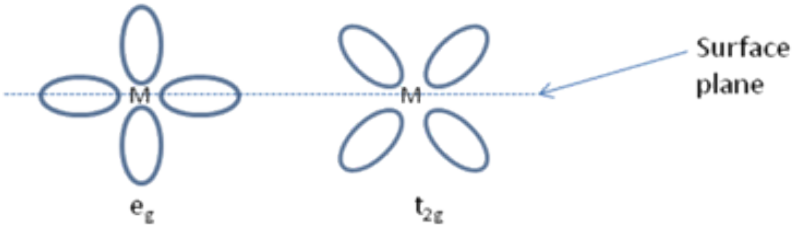

Figure 2.14: Relation of d orbitals to adsorbate orbitals.

This is where the link between the electronic theory of oxides and catalysis comes together. And again the exposed metal cations on the surface depend on the exposed plane as well as the crystal structure of the material.

Selective catalysis

Selective catalysis refers to the ability of a catalyst to preferentially accelerate the rate of one of the two probable reactions, thereby increasing the yield of one product over another. In heterogeneous catalysis of hydrocarbons it is desired that complete oxidation is not obtained because an intermediary (partially oxidized) product is required. For example in the oxidation of CH_4, it is sometimes desired to only partially oxidize the methane to CO and not CO_2. According to Haber et al. [21, 23] this can be controlled by the nature of the non-stoichiometry induced defects described in § 2.2.3 above. If shear planes are produced under reducing conditions the material will maintain its selectivity to a particular oxidation reaction with increasing temperature, and a higher activity can be thus obtained. This is because no new vacancies are formed. A material that only produces vacancies under reducing conditions, that do not restructure the surface will loose its capability for selective catalysis with temperature.

2.4 References

[1] B. Guo, A. Ghalambor, Natural Gas Engineering Handbook, Gulf Publishing Company, 2005.
[2] Hydrogen, Materials Safety Data Sheet, Praxair, 2007.
[3] Methane, Materials Safety Data Sheet, Praxair, 2007.
[4] Hydrogen sulphide, Materials Safety Data Sheet, Praxair, 2007.
[5] S. Somiya, F. Aldinger, N. Claussen, R.M. Spriggs, K. Uchino, K. Koumoto, M. Kaneno, Handbook of Advanced Ceramics, Elsevier Inc., 2003.
[6] C.N.R. Rao, B. Raveau, Transition Metal Oxides, VCH Publishers, New York, 1995.
[7] L.E. Smart, E.A. Moore, Solid State Chemistry: An Introduction, CRC Press, Boca Raton, 2005.
[8] V.E. Henrich, P.A. Cox, The Surface Science of Metal Oxides, University Press, Cambridge, 1994.
[9] P.J. Gellings, H.J.M. Bouwmeester, The CRC Handbook of Solid State Electrochemistry, CRC Press Inc., New York, 1997.
[10] W.D. Callister, Materials Science and Engineering: An Introduction, 5th edition, Wiley, New York, 2000.
[11] R.J.H. Voorhoeve, D.W. Johnson, J.P. Remeika, P.K. Gallagher, Science, 195 (1977) 827-833.
[12] J. B. Goodenough, Metallic Oxides, Pergamon Press, New York, 1971.
[13] R. O'Hayre, W. Colella, S.W. Cha, F.B. Prinz, Fuel Cell Fundamentals, 1st edition, Wiley, New York 2005.
[14] K. Kendall, N.Q. Minh, S.C. Singhal, in: S.C. Singhal, K. Kendall (Eds.), High Temperature SOFCs: Fundamentals, Design and Applications, Elsevier, 2003.
[15] NorECs Norwegian Electro Ceramics, ProboStat Manual, A-6 edition, Oslo, 2007.
[16] J. Winkler, P.V. Hendriksen, N. Bonanos, M. Mogensen, J. Electrochem. Soc., 145 (1998) 1184-1192.
[17] M. Cimenti, A.C. Co, V.I. Birss, J.M. Hill, Fuel Cells, 7 (2007) 364-376.
[18] A. Atkinson, S. Barnett, R.J. Gorte, J.T.S. Irvine, A.J. McEvoy, M. Mogensen, S.C. Singhal, J. Vohs, Nature Materials, 3 (2004) 17-27.
[19] J. Nowotny, C.C. Sorrell (Eds). Key Engineering Materials, 187 (1997) 125-126.
[20] Eg&G Technical Services Inc., Fuel Cell Handbook, 7th edition, 2004.
[21] J. Haber, Selectivity in Hetereogeneous Catalytic Oxidation of Hydrocarbons, American Chemical Society, Washington DC, 1996.
[22] I. Chorkendorff, J.W. Niemantsverdriet, Concepts of Modern Catalysis and Kinetics, Wiley VCH, Weinheim, 2003.
[23] J. Haber, J. Janas, M. Schiavello, R.J.D. Tilley, J. Catal., 82 (1983) 395-403.

Chapter 3

Literature Survey

Herein, the work to date on alternative (non- Ni-YSZ) anode materials will be reviewed.

3.1 Hydrogen-fueled SOFCs

The body of work on conventional hydrogen fueled SOFCs is vast [1]. Briefly, as mentioned in ∮ 2.3.2, the state of the art anode catalyst is the cermet Ni-YSZ. Typically, a 50-50 wt% mixture of NiO and YSZ is used which provides optimal electronic and ionic conduction, and gas mass transfer percolation paths. Typical performance data for an optimized, anode supported cell with thin electrolyte and LSM cathode produces about 1.8 W cm^{-1} at 800 ^oC [2]. Ni is an effective methane cracking catalyst, which leads to carbon deposition and it is easily poisoned by H_2S at concentrations greater than a few ppm. Therefore, Ni cermets are not a viable option for the direct use of H_2S-containing CH_4 fuels, without reforming of CH_4 and scrubbing the H_2S out of the inlet gas.

Most novel SOFC anode catalysts are tested in H_2 in addition to CH_4; these materials are, therefore, discussed in ∮ 3.2 and ∮ 3.3 below.

3.2 Methane-fueled SOFCs

Ni-YSZ cermets are among the anode materials currently preferred for use in solid oxide fuel cells (SOFCs), as they have both high activity towards the oxidation of H_2 and high conductivity [1]. Ni-YSZ anodes can be used as anodes for conversion of either H_2 or reformed methane (a mixture of H_2, CO and CO_2). CH_4 is internally or externally reformed using the catalytic steam reforming process 3.1 and 3.2. When the water-gas shift reaction, reaction 3.3, is also used to remove CO, the resultant fuel is mostly H_2.

$$CH_4 + H_2O \rightarrow 3H_2 + CO \tag{3.1}$$

$$\Delta G^o_{800^oC} = -45.18\ kJ\ mol^{-1}$$

$$CH_4 + CO_2 \rightarrow 2H_2 + 2CO \tag{3.2}$$

$$\Delta G^o_{800^oC} = -44.67\ kJ\ mol^{-1}$$

This reaction may be accompanied by the water gas shift reaction for CO below:

$$CO + H_2O \Rightarrow CO_2 + H_2 \tag{3.3}$$

$$\Delta G^o_{800^oC} = -0.52\ kJ\ mol^{-1}$$

Reactions 3.1 and 3.2 are followed by the electrochemical reactions at the anode catalyst surface, reactions 3.4 and 3.5 (note: Nernst potentials below and throughout are obtained from the free energies for the overall cell reactions with water vapor as a product using the commerical thermodynamic software HSC and the thermodynamic databases within):

$$H_2 + O^{2-} \rightarrow H_2O + 2e^- \tag{3.4}$$

$$E^o_{800^oC} = 0.98\ V\ , \Delta G^o_{800^oC} = -188.69\ kJ\ mol^{-1}$$

$$CO + O^{2-} \rightarrow CO_2 + 2e^- \tag{3.5}$$

$$E^o_{800^oC} = 0.98\ V,\ \Delta G^o_{800^oC} = -189.21\ kJ\ mol^{-1}$$

These reactions do not lead to degradation of the fuel cell with Ni-YSZ cermet anodes. The disadvantages of external or internal reforming are:

- A high steam (S) to carbon (C) ratio (S/C=2) is required for steam reforming. As a result the fuel is diluted, resulting in a reduction of the efficiency of the system.
- Steam reforming is an endothermic process and thus results in a heat loss from the system. In the case of internal reforming this results in additional mechanical stresses due to the resulting large thermal gradients.
- There are added cost and complexity of equipment, footprint and balance of plant requirements.

Direct oxidation of methane is more desirable since it reduces process complexity and increases the efficiency of the process. To eliminate or minimize these additional costs, methane must be used directly as feed and be oxidized in the fuel cell according to reactions 3.6 and/or 3.7 [1]:

$$CH_4 + 4O^{2-} \rightarrow CO_2 + 2H_2O + 8e^- \tag{3.6}$$

$$E^o_{800^oC} = 1.04\ V,\ \Delta G^o_{800^oC} = -800.46\ kJ\ mol^{-1}$$

$$CH_4 + 3O^{2-} \rightarrow CO + 2H_2O + 6e^- \tag{3.7}$$

$$E^o_{800^oC} = 1.06\ V,\ \Delta G^o_{800^oC} = -611.25\ kJ\ mol^{-1}$$

Direct oxidation of methane on modern SOFC anodes was first accomplished effectively in the late 1990s [3,4]. The initial work consisted of using standard Ni-YSZ cermets as the anode material. The trouble with the use of nickel was that it was as great a catalyst for adsorbing carbon as it was for breaking C-H bonds. However, during direct methane oxidation at the anode there is a propensity for a parallel reaction leading to carbon deposition, reaction 3.8. This causes irreversible catalyst degradation when the rate of carbon removal, reactions 3.9, 3.10 and 3.11, is lower than that of carbon formation, reaction 3.8 [2].

$$CH_4 \rightarrow C_{ads} + 2H_2 \tag{3.8}$$

$$\Delta G^o_{800^oC} = -27.130\ kJ\ mol^{-1}$$

$$C + O^{2-} \rightarrow CO + 2e^- \tag{3.9}$$

$$E^o_{800^oC} = 1.07\ V,\ \Delta G^o_{800^oC} = -206.73\ kJ\ mol^{-1}$$

$$C + 2O^{2-} \rightarrow CO_2 + 4e^- \tag{3.10}$$

$$E^o_{800^oC} = 1.03\ V,\ \Delta G^o_{800^oC} = -395.94\ kJ\ mol^{-1}$$

Carbon also can be removed by further reaction with the produced water:

$$C + H_2O \rightarrow CO + H_2 \tag{3.11}$$

$$\Delta G^o_{800^oC} = -18.04\ kJ\ mol^{-1}$$

Studies of carbon deposition on fuel cell catalysts have focused primarily on Ni-YSZ, and there have been several efforts toward its mitigation [5, 6-10]. With the exception of carbon deposition on several $LaCrXO_3$-based perovskite SOFC anode materials [11-13], the mechanism of carbon deposition typically includes adsorption of methane at nickel active sites, then sequential abstraction of all hydrogen from the methane molecule, leaving chemisorbed C. This chemisorbed carbon then dissolves into the metal, growing like a hair (or filament) seemingly from within the metal particle [7]. In Ni based fuel cells this results in delamination of the nickel from the YSZ substrate, and/or from induced mechanical stresses. There have been extensive carbon formation investigations in the SOFC field [14-18].

The types of carbon formed on metal surfaces can be classified as: encapsulating, whisker (graphitic or carbon fiber), and pyrolytic [19]. Pyrolytic carbon is formed mainly by carbon deposition from higher hydrocarbons. Encapsulating carbon forms a thin layer of C and CH_x species on the surface, blocking active sites. Whisker carbon formation leads to cracking of the anode due to carbon fiber growth into the nickel structure.

Strategies used for decreasing the rate of carbon formation in SOFCs operating on methane include: increasing steam to carbon ratio [8, 20, 21]; increasing hydrogen to hydrocarbon ratio [7]; increasing current density [22-24]; alloying [25-27]; using protective barrier layers [28, 29]; and using novel catalysts designed to be coke-resistant [29-32]. The adsorbed carbon blocks active sites of the nickel, thereby decreasing the performance significantly. If carbon is deposited on the surface of the catalyst it can also be electrochemically removed via reaction (3.9).

Use of humidified methane tends to decrease the extent of carbon formation by increasing the rate of reaction (3.11), but at the risk of either cell degradation or loss of performance through competitive adsorption of water [8, 20-22]. Higher current densities result in increased O^{2-} migration to the anode side, and the higher surface density of resulting oxygen species oxidizes the deposited carbon according to reaction 3.9 [22]. However, this only occurs above a critical current density. At intermediate or low current densities there is a propensity for both a decrease and an increase in carbon deposition with increasing current density [10, 22, 32].

Alternative anode catalysts have emerged that can utilize methane directly, and these typically are modified Ni-YSZ anodes, novel cermets and MMOs [1, 2]. MMOs developed over the last decade are promising candidate anode materials for SOFCs. They have high electronic and ionic conduction at elevated temperatures, stability against carbon deposition and sulphur poisoning, and good activity for oxidation of hydrocarbon fuels [29, 30]. However, their performance has only recently been improved to match that of Ni-YSZ in hydrogen, and their long-term performance is not yet established, especially for use with hydrocarbon feeds [33]. The following are a list of the major groups doing work on the most advanced materials.

Dokiya group

Horita et al. [34] investigated Ni-YSZ and Fe-YSZ under different operating conditions in attempts to prevent carbon deposition. They found that under the operating conditions Fe passivated to FeO and Fe_3O_4 which led to a decrease in the current density. Performance with Ni-YSZ was about five times better than with Fe-YSZ. Carbon deposition, even with dry CH_4, was prevented by operating at potentials more positive than -750 mV vs air, which ensured an adequate O^{2-} flux. This group was the first to use dry methane directly in the SOFC with a Ni-YSZ anode, but they have disclosed no further work.

Barnett group

Barnett et al. [35] demonstrated one of the first stable direct methane SOFCs in 1999 on Ni-YSZ. The cells which consisted of LSM (1 mm) | $Ce_{0.85}Y_{0.15}O_2$(YDC, 0.5 μm) | YSZ (8μm) | YDC (0.5 μm) | Ni-YSZ (2μm) produced 370 mW cm^{-2} at 650 ^{o}C in CH_4 (3% H_2O). The performance in H_2 was reported to be 20% higher at the same temperature. The

area specific resistance (ASR) was about 1.25 Ω cm^2 in CH_4(3% H_2O) and 0.25 Ω cm^2 in H_2 (3% H_2O) at 600 ^oC. No carbon deposition was observed when operated below 700 ^oC. The activity and stability were attributed to the oxygen storage ability of the YDC layer, which released oxygen during reaction and kept the surface carbon free.

Later, Barnett and co-workers successfully directly oxidized methane on Ni-YSZ anodes without carbon formation with a high system performance of 520 mW cm^{-2} at 700 ^oC and 1,270 mW cm^{-2} at 800 ^oC using a LSCF | LSCF-GDC(30 wt%) | YSZ | Ni-YSZ (1 mm) MEA [36]. Mass spectral analysis of the effluent showed that the main reaction products were H_2 and CO, with the explanation that carbon deposition was avoided by the high currents generated in the cell.

The Barnett group also developed one of the first all-oxide anodes, $La_{0.8}Sr_{0.2}Cr_{0.8}Mn_{0.2}O_3$, for methane oxidation [37]. The final anode was a composite, containing GDC and 5 wt% NiO, and the MEA components LSCF-GDC | GDC (0.3 mm) | LSCM-GDC-NiO produced 130 mW cm^{-2} at 750 ^oC.

More recently, $La_{0.8}Sr_{0.2}Cr_{0.98}V_{0.02}O_3$, was developed [38]. The final anode was a composite, containing GDC and 5wt% NiO, and the MEA components were LSCF-GDC | GDC (0.3 mm) | LSCV-GDC-NiO, which produced 107 mW cm^{-2} at 700 ^oC. After further optimization a higher performance was achievable; however no testing was conducted using methane [39].

The latest material to emerge from this group is $LaSr_2Fe_2CrO_9$ [40]. This complex oxide had higher oxygen ion conductivity and as a result produced 300/360 mW cm^{-2}. Anode polarization resistances of 0.20/0.25 Ω cm^2 were measured at 750/800 ^oC in humidified H_2.

Recently a novel concept was introduced in which a conducting oxide buffer layer was used on top of Ni-YSZ [41]. The MEAs were anode supported with the arrangement LSM-YSZ | YSZ | Ni-YSZ | $Sr_{0.8}La_{0.2}TiO_3$ (total thickness of $\sim 800\ \mu$m). At 800 ^oC they produced 900, 700 and 550 mW cm^{-2} in H_2, H_2(100 ppm H_2S) and natural gas, respectively. It was shown that the buffer layer allowed for operation in natural gas, H_2 and H_2 (100 ppm H_2S) with only slight degradation in performance.

Mogensen group

Mogensen et al. [4], also in 1999, used $Ce_{0.6}Gd_{0.4}O_{1.8}$ (CGO or GDC), as the anode in humidified hydrogen and humidified methane SOFC. They revealed that at 1000 ^oC the maximum power density was 500 mW cm^{-2} and 80 mW cm^{-2} in H_2 and CH_4, respectively. The cells consisted of GDC | YSZ(180 μm) | LSM-YSZ. Only slight carbon deposition was observed at low steam to carbon ratios. As mentioned in § 2.3.2, GDC is a mixed ionic-electronic conductor, but it also has catalytic activity for hydrogen oxidation. The low activity for methane oxidation was ascribed to a lack of a cracking or oxidation catalyst activity, adding that previous results [3] were attributable to the activity of a porous Pt current collector layer on the anode.

In more recent work, Mogensen et al. expanded on the GDC work with a look at the effect of Gd doping [42]. They found that an adequately low ASR of 0.1 was found at 700 ^{o}C with Gd content greater than 0.1 (ie., $Ce_{0.9}Gd_{0.1}O_{1.8}$ and greater). Furthermore, they stipulated that coking will not be a problem below 750 ^{o}C.

In a review paper Mogensen et al. analyzed hydrocarbon oxidation on doped CeO_2 and other oxides, putting into question earlier work which showed high activity at low temperatures [9]. They insisted that, at the low temperatures examined (700 ^{o}C), the activity was too low, and that it can be attribed to the Pt current collectors used.

Irvine group

Irvine's group has been involved in development of MIEC anodes for direct oxidation of methane for the last decade. In [44] they reported a $La_{0.75}Sr_{0.25}Cr_{0.5}Mn_{0.5}O_3$ (LSCM) perovskite anode. The anode polarization was 0.8 Ω cm^2 at 900 ^{o}C for CH_4 as fuel, and 0.25 Ω cm^2 using H_2. The MEA consisted of LSM (graded with YSZ) | YSZ (0.3 mm) | LSCM (graded with YSZ) operated on humidified methane, with performance around 300 mW cm^{-2} at 950 ^{o}C (500 mW cm^{-2} at 950 ^{o}C in humidified H_2). Oxidation of the anodes after a 6 h galvanostatic test in CH_4 in a TGA showed only minor carbon deposition. They have also come up with some novel uses for this material, such as using it as a symmetric fuel cell as anode and cathode, owing to its redox stability [45]. Since, the first publication of this material they have been able to optimize their cells and have thus far achieved 600 mW cm^{-2} at 800 ^{o}C (160 mW cm^{-2} at 600 ^{o}C) in humidified H_2 using a LSM | LSGM (0.1 mm)| LSCM assembly [46]. Additional modifications proposed are partial substitution of La with Ce [47], Cu-GDC [48], and Ni-GDC additions [37]. Pd-CeO_2 addition on an optimized MEA produced 710 mW cm^{-2} (humidified CH_4) and 1.1 mW cm^{-2} (humidified H_2) at 800 ^{o}C [49].

Recently, further investigations have revealed more information regarding LSCM. It has been determined that LSCM is a p-type conductor throughout the fuel cell p_{O_2} range, with a oxygen transference number in the range 9 x 10^{-7} to 2 x 10^{-6} at atmospheric oxygen pressure [50].

Concurrently, they reported on a novel $La_2Sr_4Ti_6O_{19}$ (LST) structure which is a mixture of a perovskite and pyrochlore [51]. A MEA consisting of LSM | YSZ (0.3 mm) | LST produced 21 mW cm^{-2} at 900 ^{o}C. Although it did not produce very high fuel cell performance, it was an interesting material as the structure allowed for oxygen overstoichiometry under reducing conditions and enhanced electrical conductivity due to the partial reduction of Ti^{4+} to Ti^{3+} [52]. Later they were able to use this knowledge to prevent the formation of extended defects, which would have removed vacancies, by doping with Mn and Ga, to form $La_{4}Sr_8Ti_{11}Mn_{0.5}Ga_{0.5}O_{37.5}$ (LSTMG) [53]. An MEA consisting of LSM | YSZ (0.33 mm) | LSTMG (graded with YSZ) obtained 325 mW cm^{-2} at 950 ^{o}C in humidified methane (3 % H_2O).

Vohs-Gorte Group

The earliest reports from these researchers were on novel Rh-$Ce_{0.9}Sm_{0.1}O_2$ anodes [54]. These cells produced about 5 mW cm^{-2} using both H_2 and CH_4 fuels at 800 ^oC.

Several years later they revolutionized the field with their novel cermets concept, Ni-CeO_2, which was found to deactivate in direct CH_4 operation [55]. However, they followed through with Cu-CeO_2, which proved to be a very good anode design [56, 57]. MEAs consisting of LSM-YSZ (50/50 wt%) | YSZ (60 μm) | Cu-CeO_2(40 wt% Cu, 20 wt% CeO_2, YSZ fibers), produced: 225/300 mW cm^{-2} in H_2 at 700/800 ^oC; 100/150 mW cm^{-2} in n-butane 700/800 ^oC; and 100 mW cm^{-2} in CH_4 at 700 ^oC. They reported stable operation using a variety of hydrocarbon fuels including CH_4. Further examination revealed that CeO_2 must be introducing a drastic catalytic effect to the catalytically inactive Cu, since Cu-YSZ was electrocatalytically inactive.

Alloying Cu with Ni produced good results, 300/500 mW cm^{-2} in H_2/CH_4 at 800 ^oC using 10 wt%CeO_2-20% Cu and Ni [58]. Later the performance was increased by using a Cu-Co alloy with ceria [59] for direct methane oxidation, producing 250 mW cm^{-2} at 800 ^oC.

Goodenough group

Goodenough et al. [60, 61], developed a double perovskite, Sr_2MgMoO_6 ($A_2BB'O_6$ type perovskite) and $Sr_2Mg_{1-x}Mn_xMoO_6$ (SMMO). The MEAs consisted of SCF | LSGM (300 μm) | $La_{0.4}Ce_{0.6}O_{2-\delta}$ (LDC) | SMgMoO/SMnMoO, and at 800 ^oC the cells produced 838/650 and 400/150 mW cm^{-2} in H_2 and CH_4, respectively. The LCO buffer layer ensured no interdiffusion between the LSGM electrolyte and SMMO. The Mg-containing double perovskite was more active for methane. Although they used Pt as a current collector, they claimed this did not introduce a catalytic effect into their results. It appeared that LDC itself was active to hydrogen but not CH_4.

Both SMMO catalysts showed performance that was comparable to Ni-YSZ in hydrogen fuel, but which had the additional benefit that it was sulfur resistant, see $\oint$ 3.3. The cell produced 350 mW cm^{-2} with methane as the fuel and over 800 mW cm^{-2} in hydrogen with 500 ppm H_2S at 800 ^oC.

La doping into SMMO, to produce the mixed oxide $Sr_{2-x}La_xMgMoO_6$ (SLMM) produced optimum results that were recorded with La in 8 mole concentration (x = 0.8), producing 500/650 mW cm^{-2} at 800/850 ^oC in CH_4 [62]. The results obtained were an enhancement over previous results in CH_4 on SMMO alone, and also enhanced performance using C_2H_6 and C_3H_8. This is currently the benchmark in alternative anode materials with sulfur and carbon resistance, although the data have not been reproduced.

This group also tested LSCM with sputtered Pt and Cu and found a drastic improvement in conductivity and activity to CH_4 as cells SCF | LSGM (300 μm) | $La_{0.4}Ce_{0.6}O_{2-\delta}$ (LDC) | LSCM (Pt and Cu) produced 450/550 mW cm^{-2} at 800/850 ^oC in CH_4 [63], a strong

indication that an additional catalytic component is required in LSCM.

Jiang group

This group been largely involved with improving LSCM through changes in preparation techniques as well as through the addition of GDC and YSZ [64-66]. They stipulated that the addition of GDC caused dry reforming of the fuel via lattice oxygen, which produced more H_2 and CO for reaction at active sites via the following reactions:

$$CH_4 + O^x_{O,GDC} \rightarrow CO + 2H_2 + V^{\bullet\bullet}_{O,GDC} \tag{3.12}$$

The lattice oxygen can be replenished via a CO_2 shift:

$$CO_2 + V^{\bullet\bullet}_{O,GDC} \rightarrow CO + O^x_{O,GDC} \tag{3.13}$$

in addition to the O^{2-} from cathode side.

They have also done testing in sulfur environments, see ∮ 3.3 below.

McIntosh group

This new group is performing in depth research into methane oxidation on perovskite oxides, primarily LSCM [67,68]. Their approach was novel in that they used ex-situ reactivity experiments, using temperature programmed reactions of CH_4 over the perovskite in O_2-free atmospheres, to show that the perovskite is active to methane oxidation; however, its activity in the fuel cell environment was sluggish. With increasing Mn content in LSCM, the activity increased; and with increasing temperature the reaction changed from direct oxidation to partial oxidation.

Further notable publications

$La_{0.6}Sr_{0.4}Fe_{0.8}Co_{0.2}O_3/Ce_{0.8}Gd_{0.2}O_{1.9}$(LSFCO/GDC) composite anode material was investigated for the direct electrochemical oxidation of methane in intermediate temperature solid oxide fuel cells [69]. A maximum power density of 170 mW cm^{-2} at 800 ^oC was obtained with CH_4 feed using (unknown) | GDC(300 μm) | LSFCO/GDC (70-30 wt%). The anode degraded in ex situ cell experiments but not in fuel cell experiments.

$SrFeCo_{0.5}O_x$, $SrCo_{0.8}Fe_{0.2}O_x$ and $La_{0.6}Sr_{0.4}Fe_{0.8}Co_{0.8}O_{3-\delta}$ were synthesized and prepared as anodes on yttria-stabilized zirconia for solid oxide fuel cells [70]. Power output measurements showed that the anodes composed of such kinds of oxides exhibited modest electrochemical activities to both H_2 and CH_4 fuels, giving maximum power densities around 100 mW cm^{-2} at 950 ^oC.

$La_{1-x}Sr_xVO_3$ were synthesized and examined as potential anode materials for solid oxide fuel cells [71]. The best performance was found for Pt | YSZ (1 mm) | $La_{0.6}Sr_{0.4}VO_3$/YSZ (50/50 wt%) which had anodic polarization resistances of 0.85/1.38 Ω cm^2 and anodic overpotentials of 0.13/0.2 V at 900 ^oC in H_2/CH_4.

A variety of La-Cr oxides were tested for pure catalytic activity [72]. Lanthanum had less effect on catalytic activity than the B site atom (in ABO_3), and stability decreased with decreasing size of the A cation (in low oxygen partial pressures). Mg was an inhibitor, while Sr and Ca containing catalysts had good activity. Co was an inhibitor, while Mn Fe and Ni were effective.

It was found that $La_{0.8}Sr_{0.2}Cr_{0.97}V_{0.03}O_3$ had very high polarization resistance to CH_4 fuel, and to H_2 at 850 ^oC [73].

3.3 H_2S containing gas-fueled SOFCs

Sulfur is a component in most hydrocarbon resources. If it is present in large concentrations, greater than a 50 ppm, the gas or oil is considered sour. Sulfur tolerance for concentrations of less than 5% is a major design requirement, for gases containing higher concentrations of H_2S the anode should also be active for the oxidation of H_2S. Ni-YSZ anodes deactivate in the presence of H_2S even in a few ppm concentrations [74]. The possible reactions involved in the deactivation of the catalyst are via molecular adsorption (physisorption) 3.14, dissociative (chemisorption) adsorption 3.15, and sulfidation 3.16 [75]:

$$M + H_2S \Rightarrow M - SH_{2,ads} \rightarrow M - S_{ads} + H_2 \tag{3.14}$$

$$M + H_2S \Rightarrow M - SH_{ads} + M - H_{ads} \rightarrow M - S_{ads} + H_2 \tag{3.15}$$

$$xM + yH_2S \rightarrow MxSy + yH_2 \tag{3.16}$$

On Ni all three reactions are very favorable, while on Cu there is no attraction between H_2S and the (111) surface [75]. If sulfur tolerance is the goal, the ideal case is 3.14, physisorption. This is a reversible process as long as it doesn't proceed to completion (chemisorption), since there is no bonding between the surface and the molecule. Sulfidation, (3.16), is the worst case since it changes the bulk structure of the catalyst. Reversible chemisorption is desirable in the case of oxidation of H_2S on the anode surface (H_2S as the fuel). The electrochemical oxidation of H_2S can proceed via the following reactions, including gas phase reforming and secondary electrochemical reactions of the product S_2:

$$H_2S + O^{2-} \rightarrow 1/2S_2 + H_2O + 2e^- \tag{3.17}$$

$$E^o_{800^oC} = 0.78\ V,\ \Delta G^o_{800^oC} = -151.11\ kJ\ mol^{-1}$$

$$H_2S + 3O^{2-} \rightarrow SO_2 + H_2O + 6e^- \tag{3.18}$$

$$E^o_{800^oC} = 0.75\ V,\ \Delta G^o_{800^oC} = -434.69\ kJ\ mol^{-1}$$

$$S_2 + 4O^{2-} \rightarrow 2SO_2 + 8e^- \tag{3.19}$$

$$E^o_{800^oC} = 0.74\ V,\ \Delta G^o_{800^oC} = -567.15\ kJ\ mol^{-1}$$

$$H_2S \rightarrow 1/2S_2 + H_2 \tag{3.20}$$
$$\Delta G^o_{800^oC} = 37.57 kJ mol^{-1}$$

$$2H_2S + SO_2 \leftrightarrow 3/nS_n + 2H_2O\ n = 2-8 \tag{3.21}$$
$$\Delta G^o_{800^oC} = -9.33\ kJ\ mol^{-1}$$

Adsorbed sulfur will block the direct electrochemical oxidation of CH_4 and H_2 via equations, by both physically blocking active site centers on the surface of the catalyst, ex Ni atoms, and chemically by changing the electronic density of the surface.

Winnick-Liu group

This group from Georgia Tech is one of the pioneers of the sulfur containing gases movement. In one of their first publications relating to anode materials for oxides, for MCFC fuel cells, they determined the stabilities and conductivities of Cr and Ga based perovskites [76]. They found that: $La_{1-x}Sr_xGaO_3$ substituted with Ga doped with Cr increased electrical conductivity but was unstable in H_2S; Mg, Ti doped $LaCrO_3$ had high conductivity and was stable in H_2S environment, and no phase changes were observed; $Y_{0.9}Ca_{0.1}FeO_3$ was unstable in H_2S; $SrCo_{0.8}Fe_{0.2}O_3$ was unstable in H_2S, but had a high conductivity. However, no further work was performed on any of these materials.

Their focus shifted to a La-V based perovskite, $La_{1-x}Sr_xVO_3$ (LSV) [77]. It was initially tested in H_2 and H_2S environments, producing about 140 mW cm^{-2} at 1000 ^{o}C in 10%H_2S using a SSC/GDC | YSZ | LSV cell. They initially reported that it was inactive towards H_2. Later, they optimized the cell and a LSM/YSZ | YSZ | LSV cell produced 100 mW cm^{-2} in 5% H_2S-N_2 and 125 mW cm^{-2} in 5% H_2S-H_2 at 1000 ^{o}C. They then stipulated that the anode is active towards H_2 fuel as well. Finally, they concluded that it was not redox stable, although it had a high conductivity at 800 ^{o}C of 800-900 S cm^{-1} [78]. Later they tested it in a H_2S/CH_4 fuel mixture and found encouraging results [79]. The cell consisted of LSM/YSZ | YSZ (250 μm) | LSV(Pt) and at 950 ^{o}C and methane with 5% H_2S produced 280 mW cm^{-2}. It was reported to be active in H_2S, H_2 and CH_4.

Simultaneously, they tested a pyrochlore material $Gd_2Ti_{1.4}Mo_{0.6}O_7$ [80]. A cell consisting of LSM/YSZ | YSZ (250 μm) | GTM and 240/360 mW cm^{-2} was produced in 5%H_2S-H_2 at 800/950 ^{o}C. The anode resistance at OCV and 950 ^{o}C was 0.2 Ω cm^2 in the same fuel gas. The anode was reportedly stable after long term exposure to H_2 and active in both H_2 and H_2S.

They were the first to test LSCM under H_2S conditions [81]. They found that after ex-situ exposure to 10% H_2S-H_2 for 5 days, MnS, La_2O_2S and α-MnOS were formed, while the current density fell from 220 to 80 mA cm^{-2} at 0.7 V in 7 h in 10% H_2S-H_2 at 950 ^{o}C.

Gorte group

The Cu, Cu-Ni and Cu-Co / CeO_2 cermets were found to degrade reversibly in 5000 ppm H_2S concentrations and various hydrocarbon feeds [82,73]. This was due to CeOS formation, not Cu_2S formation, at high H_2S concentrations. H_2S concentrations of up to 450 ppm were adequately low for stable operation at 800 ^oC producing a stable 300 mW cm^{-2} in humidified H_2.

Giorgi group

This group from Ottawa, has produced interesting results using Ni and Co -YSZ cermets in methane and sour gas fuels [84-86]. What they found was that after the introduction of hydrogen sulfide there was an initial decrease in performance followed by an enhancement, 1.5 and 6 times greater performance, respectively, due to NiS and CoS formation. They found a silvery grey film on the surface of the anodes which contained S, O and C. Mass spectral analysis of the effluent also showed formation of CS_2 but not COS or SO_2. Cells consisted of LSM | YSZ (500 μm) | Ni/YSZ (Co/YSZ) with embedded Pt-Rh current collectors. The cells with formed Co-S produced about 50 - 175 mW cm^{-2} at 850 ^oC under potentiostatic operation in 10%H_2S-CH_4.

H_2S was required in both systems for efficient long-term operation, which was especially achieved with the Co-S anodes. Ni-Cu alloying produced detrimental effects on performance and mechanical integrity, while Co addition to Ni produced synergistic effects on the electrocatalytic activity of the sulfides.

Further notable publications

$La_{1-x}Sr_xBO_3$ (B=Cr, Mn, Ti) was tested in hydrogen and H_2S atmospheres [87]. In cells consisting of LSM/YSZ | YSZ (500 μm) | $Sr_{0.6}La_{0.4}TiO_3$/YSZ there was no degradation in the presence of up to 5000 ppm of H_2S in a hydrogen fuel and a power density of 200 mW cm^{-2} was achieved. This anode was also able to operate for 8 h with 1% H_2S without irreversible side-effects. The sulfur tolerance was worse with pure Cr at the B site or LSCM. Interestingly, they reported a 20% increase in performance in the presence of H_2S.

$La_2Mo_2O_9$ (LMO) was tested in H_2 and H_2S atmospheres [88]. The performance of a MEA consisting of SCF | LSGM (300 μm) | LMO achieved 1490 and 860 mW cm^2 in dry H_2 at 900 ^oC and 800 ^oC, respectively. With 10 ppm H_2S the cell performance decreased to 700 mW cm^2 at 800 ^oC but remained stable over 100 h in both pure H_2 and in H_2 with 20 ppm H_2S. The anode degraded under higher concentrations of H_2S ascribed to a chemical reaction. The redox stability of this anode material is in question, as it had to be reduced from an amorphous state. It was briefly stated that the anode was inactive in CH_4.

The Singapore group tested LSCM with GDC addition for its stability in sour gas (0.5%H_2S) [89]. MEAs consisting of Pt | YSZ (1 mm) | LSCM/GDC (50-50 wt%, and Pt mesh) held potentiostatically at 0.5V and 850 ^oC had the anodic current drop from 233

mA cm^{-2} to 200 mA cm^{-2} over a 10 h period, after the fuel was changed from CH_4 to 0.5%H_2S-CH_4. Some reactor products, such as MnS, La_2O_2S, and αMnOS, were detected using XRD on the anode after 120 h of stability test.

Colleagues from our own group developed a composite anode catalyst that was active and stable in 5000 ppm H_2S and 40% H_2-60% CO (syngas, synthesis gas or coal gas) [90]. The composite catalyst was $LaCrO_3$-VO_x-YSZ (VLY) in a 40/40/20 ratio. The MEAs consisted of Pt | YSZ (300 μm) | VLY and obtained 260 mW cm^{-2} at 900 ^oC in the synthesis gas. Proprietary VLY is being further explored. Notably, carbon deposition was suppressed using alkali metal dopants; however, this was achieved at the expense of activity.

3.4 References

[1] K. Kendall, N.Q. Minh, S.C. Singhal, in: S.C. Singhal, K. Kendall (Eds.), High Temperature SOFCs: Fundamentals, Design and Applications, Elsevier, 2003.

[2] Eg&G Technical Services Inc., Fuel Cell Handbook, 7th edition, 2004.

[3] E.P. Murray, T. Tsai, S.A. Barnett, Nature, 400 (1999) 649-651.

[4] O.A. Marina, C. Bagger, S. Primdahl, M. Mogensen, Solid State Ionics, 123 (1999) 199-208.

[5] R. T. Baker, I. S. Metcalfe, Ind. Eng. Chem. Res., 34 (1995) 1558-1565.

[6] H. He, J.M. Hill, Appl. Catal. A: Gen., 317 (2007) 284-292.

[7] C.H. Bartholomew, Appl. Catal. A: Gen., 212 (2001) 17-60.

[8] C.M. Finnerty, N.J. Coe, R.H. Cunningham, R.M. Ormerod, Catal. Today, 46 (1998) 137-145.

[9] M. Mogensen, K. Kammer, Ann. Rev. Mater. Res., 33 (2003) 321-331.

[10] V. Alzate-Restrepo, J.M. Hill, Appl. Catal. A, 342 (2008) 49-55.

[11] R.T. Baker, I.S. Metcalfe, Appl. Catal. A, 126 (1995) 297-317.

[12] R.T. Baker, I.S. Metcalfe, Appl. Catal. A, 126 (1995) 319-332.

[13] J. Sfeir, P.A. Buffat, P. Mckli, N. Xanthopoulos, R. Vasquez, H.J. Mathieu, J. Van herle, K. R. Thampi, J. Catal., 202 (2001) 229-244.

[14] F. Billaud, C. Gueret, and J. Weill, Thermochimica Acta, 211 (1992) 303-322.

[15] K.M. Walters, A.M. Dean, H.Y. Zhu, and R.J. Kee, J. Power Sources, 132 (2003) 182-189.

[16] G.K. Gupta, E.S. Hecht, H.Y. Zhu, A.M. Dean, and R.J. Kee, J. Power Sources, 156 (2006) 434-447.

[17] G.K. Gupta, J.R. Marda, A.M. Dean, A.M. Colclasure, H.Y. Zhu, and R.J. Kee, J. Power Sources, 162 (2006) 553-562.

[18] G.K. Gupta, A.M. Dean, K. Ahn, and R.J. Gorte, J. Power Sources, 158 (2006) 497-503.

[19] J. Sehested, Catal. Today, 111 (2006) 103-110.

[20] S.L. Douvartzides, F.A. Coutelieris, A.K. Demin, P.E. Tsiakaras, AIChE J., 49 (2003) 248-257.
[21] K. Eguchi, H. Kojo, T. Takeguchi, R. Kikuchi, K. Sasaki, Solid State Ionics, 152/153 (2002) 411-416.
[22] Y.B. Lin, Z.L. Zhan, J. Liu, S.A. Barnett, Solid State Ionics, 176 (2005) 1827-1835.
[23] S. Park, R. Craciun, J.M. Vohs, R.J. Gorte, J. Electrochem. Soc., 146 (1999) 3603-3605.
[24] J.H. Koh, B.S. Kang, H.C. Lim, Y.S. Yoo, Electrochem. Solid State Lett., 4 (2001) A12-A15.
[25] C.M. Finnerty, R.M. Ormerod, J. Power Sources, 86 (2000) 390-394.
[26] T. Takeguchi, Y. Kani, T. Yano, R. Kikuchi, K. Eguchi, K. Tsujimoto, Y. Uchida, A. Ueno, K. Omoshiki, and M. Aizawa, J. Power Sources, 112 (2002) 588-595.
[27] N.C. Triantafyllopoulos, S.G. Neophytides, J. Catal., 239 (2006) 187-199.
[28] Y. Lin, Z.L. Zhan, S.A. Barnett, J. Power Sources, 158 (2006) 1313-1316.
[29] M.D. Gross, J.M. Vohs, R.J. Gorte, J. Mater. Chem., 17 (2007) 3071-3077.
[30] J.W. Fergus, Solid State Ionics, 177 (2006) 1529-1541.
[31] G. Kim, G. Corre, J.T.S Irvine, J.M. Vohs, R.J. Gorte, Electrochem. Solid State Lett., 11 (2008) B16-B19.
[32] M. Ihara, C. Yokoyama, A. Abudula, R. Kato, H. Komiyama, K. Yamada, J. Electrochem. Soc., 146 (1999) 2481-2487.
[33] J.B. Goodenough, Y.H. Huang, J. Power Sources, 173 (2007) 1-10.
[34] T. Horita, N. Sakai ,T. Kawada, H. Yokokawa, M. Dokiya, J. Electrochem. Soc., 143 (1996) 1161-1168.
[35] T. Tsai, S.A. Barnett, Solid State Ionics, 98 (1997) 191-196.
[36] Y. Lin, Z. Zhan, J. Liu, S.A. Barnett, Solid State Ionics, 176 (2005) 1827-1835.
[37] J. Liu, B.D. Madsen, Z. Ji, S.A. Barnett, Electrochem. Solid-State Lett., 5 (2002) A122-A124.
[38] B.D. Madsen, S.A. Barnett, Solid State Ionics, 176 (2005) 2545-2553.
[39] B.D. Madsen, S.A. Barnett, J. Electrochem. Soc., 154 (2007) B501-B507.
[40] J.M. Haag, B.D. Madsen, S.A. Barnett, K.R. Poeppelmeiera, Electrochem. Solid-State Let., 11 (2008) B51-B53.
[41] M.R. Pillai, I. Kim, D.M. Bierschenk, S.A. Barnett, J. Power Sources, 185 (2008) 10861093.
[42] K. Kammer, M. Mogensen, Electrochem. Solid-State Lett., 8 (2005) A108-A109.
[43] S. Tao, J.T.S. Irvine, Nature Materials, 2 (2003), 320-323., S. Tao, J.T.S Irvine, J. Electrochem. Soc., 151 (2004) A252-A259.
[44] D.M. Bastidas, S. Tao, J.T.S. Irvine, J. Mater. Chem., 16 (2006) 1603-1605.
[45] J. Pena-Martinez, D. Marrero-Lopez, J.C. Ruiz-Morales, C. Savaniu,P. Nunez, J.T.S. Irvine, J. Chem. Mater., 18 (2006) 1001-1006.

[46] E. Lay, G. Gauthier, S. Rosini, C. Savaniu, J.T.S. Irvine, Solid State Ionics, 179 (2008) 1562-1566.
[47] J.C. Ruiz-Morales, J. Canales-Vazquez, D. Marrero-Lopez, J.T.S. Irvine, Electrochimica Acta, 52 (2007) 72177225.
[48] V.V. Kharton, E.V. Tsipis, I.P. Marozau, A.P. Viskup, J.R. Frade, J.T.S. Irvine, Solid State Ionics, 178 (2007) 101-113.
[49] G. Kim, G. Corre, J. Irvine, J. Vohs, R.J. Gorte, Electrochem. Solid State Lett., 11 (2008) B16-B19.
[50] J. Canales-Vazquez, S.W. Tao, J.T.S. Irvine, Solid State Ionics, 159 (2003) 159165.
[51] J. Canales-Vazquez, M.J. Smith, J.T.S. Irvine, W. Zhou., Adv. Funct. Mater., 15 (2005) 1000-1008.
[52] J.C. Ruiz-Morales, J. Canales-Vzquez, C. Savaniu, D. Marrero-Lpez, W. Zhou, J.T.S. Irvine, Nature, 439 (2006) 568-571.
[53] E.S. Putna, J. Stubenrauch, J.M. Vohs, R.J. Gorte, Langmuir, 11 (1995) 4832-4837.
[54] S. Park, R. Craciun, J.M. Vohs, R.J. Gorte, J. Electrochem. Soc., 146 (1999) 3603-3605.
[55] S.D. Park, J.M. Vohs, R.J. Gorte, Nature, 404 (2000) 265-267.
[56] R.J. Gorte, S. Park, J.M. Vohs, C. Wang, Adv. Mater., 12, (2000) 1465-1469.
[57] H. Kim, C. Lu,W.L. Worrell,J.M. Vohs, R.J. Gorte, J. Electrochem. Soc., 149 (2002) A247-A250.
[58] S. Lee, K. Ahn, J.M. Vohs, R.J. Gorte, Electrochem. Solid-State Lett., 8 (2005) A48-A51.
[60] Y.H. Huang, R.I. Dass, J.C. Denyszyn, J.B. Goodenough, J. Electrochem. Soc., 153 (2006) A1266-A1272.
[61] Y.H. Huang, R.I. Dass, Z.L. Xing, J.B. Goodenough, Science, 312 (2006) 254-257.
[62] Y. Ji, Y. Huang, J. Ying, J.B. Goodenough, Electrochem. Comm., 9 (2007) 1881-1885.
[63] J. Wan, J. Zhu, J. Goodenough, Solid State Ionics, 177 (2006) 1211-1217.
[64] S. Jiang, X. Chen, S. Chan, J. Kwok, K. Khor, Solid State Ionics, 177 (2006) 149-157.
[65] S. Jiang, X. Chen, S. Chan, J. Kwok, J. Electrochem. Soc., 153 (2006) A850-A856.
[66] X.J. Chen, Q.L. Liu, K.A. Khor, S.H. Chan, J. Power Sources, 165 (2007) 3440.
[67] M. K. Bruce, M. van den Bossche, S. McIntosh, J. Electrochem. Soc., 155 (2008) B1202-B1209.
[68] M. van den Bossche, S. McIntosh, J. Catal., 255 (2008) 313323.
[69] A. Sin, E. Kopnin, Y. Dubitsky, A. Zaopo, A.S. Arico, L.R. Gullo, D. La Rosa, V. Antonucci, J. Power Sources, 145 (2005) 6873.
[70] S. Wang, Y. Jiang , Y. Zhang, W. Li, J. Yan, Z. Lu, Solid State Ionics, 120 (1999) 75-84.
[71] X. M. Ge, S. H. Chanz, J. Electrochem. Soc., 156 (2009) B386-B391.

[72] J. Sfeir, P.A. Buffat, P. Mockli, N. Xanthopoulos, R. Vasquez, H.J. Mathieu, J. Van herle, K. Ravindranathan Thampi, J. Catal., 202 (2001) 229-244.
[73] S. Primdahl, J.R. Hansen, L. Grahl-Madsen, P.H Larsen, J. Electrochem. Soc., 148 (2001) A74-A81.
[74] M. Gong, X. Liu, J. Tremblay, C. Johnson, J. Power Sources, 168 (2007) 289-298.
[75] M. Gong, 2007, Y.M. Choi, C. Compson, M.C. Lin, M. Liu, Chem. Phys. Letters, 421, (2006) 179-183.
[76] S. Wang, M. Liu, J. Winnick, J. Solid State Electrochem., 5 (2001) 188-195.
[77] L. Aguilar, S. Zha, S. Li, J. Winnick, M. Liu, Electrochem. Solid-State Lett., 7 (2004) A324-A326.
[78] Z. Cheng, S. Zha, L. Aguilar, M. Liu, Solid State Ionics, 176 (2005) 1921-1928.
[79] Z. Cheng, S. Zha, L. Aguilar, D. Wang, J. Winnick, M. Liu, Electrochem. Solid-State Lett., 9 (2006) A31-A33.
[80] S. Zha, Z. Cheng, M. Liu, Electrochem. Solid-State Lett., 8 (2005) A406-A408.
[81] S. Zha, P. Tsang, Z. Cheng, M. Liu, J. Solid State Chem., 178 (2005) 18441850.
[82] H. Kim, J.M. Vohs, R.J. Gorte, Chem. Commun., (2001) 23342335.
[83] H. He, R.J. Gorte, J.M. Vohs., Electrochem. Solid-State Lett., 8 (2005) A279-A281.
[84] C.M. Grgicak, M.M. Pakulska, J.S. OBrien, J.B. Giorgi, J. Power Sources, 183 (2008) 26-33.
[85] C.M. Grgicak, R. Green, J.B. Giorgi, J. Power Sources, 179, (2008) 317-328.
[86] M.M. Pakulska, C.M. Grgicak, J.B. Giorgi, Appl. Catal. A, 332 (2007) 124129.
[87] R. Mukundan, E.L. Brosha, F.H. Garzon, Electrochem. Solid-State Lett. 7 (2004) A5-A7.
[88] X.C. Lu, J.H. Zhu, J. Electrochem. Soc., 155 (2008) B1053-B1057.
[89] X.J. Chen, Q.L. Liu, S.H. Chan, N.P. Brandon, K.A. Khor, J. Electrochem. Soc., 154 (2007) B1206-1210.
[90] Z.R. Xu, J.L. Luo, K.T. Chuang, A.R. Sanger., J. Phys. Chem. C, 111 (2007) 16679-16685.

Chapter 4

$Ce_{0.9}Sr_{0.1}VO_x$ (x = 3,4) as anode materials for H_2S-containing CH_4 fueled solid oxide fuel cells

4.1 Introduction

$La_{0.7}Sr_{0.3}VO_3$ (LSV) type perovskites were selected as the prototypical material for this thesis as it has been shown that vanadium containing oxide catalysts have promising catalytic activity for conversion of a variety of fuels in fuel cells [1-6]. A power density of 275 mW cm^{-2} was achieved using LSV for conversion of 5% H_2S-CH_4 at 950 ^oC [1]. I decided to examine the potential utility of new Ce- and V-containing oxide materials having perovskite (ABO_3) or zircon (ABO_4) types of structure (V^{n+} (n = 3, 5 for perovskite and zircon types of structure), respectively), based on the LSV phase [7-10].

To evaluate the role of the A-site cation, Ce^{3+} was selected as the A-site cation in both the perovskite and zircon-type anodes as it was expected to confer catalytic activity and redox stability, whereas La^{3+} typically was used in prior investigations utilizing perovskite catalysts [1, 5]. Moreover, it was recognized that the different valence states available for $Ce^{3+/4+}$ can provide a secondary active site on the surface of the anode, and a recent patent lists several Ce based perovskites as anodes for SOFCs [11]. The combination of Ce and V in a heterogeneous catalyst is precedented: unpromoted $CeVO_3$ and $CeVO_4$ each showed significant activity when tested as oxidation catalysts for H_2S and hydrocarbon fuels at intermediate temperatures [11-14].

This chapter contains results on the stability and activity in 0.5% H_2S-CH_4 of $Ce_{0.9}Sr_{0.1}VO_3$ and $Ce_{0.9}Sr_{0.1}VO_4$ anode materials. XRD showed that $Ce_{0.9}Sr_{0.1}VO_4$ was reduced when the fuel gas was 0.5% H_2S-CH_4, while $Ce_{0.9}Sr_{0.1}VO_3$ remained stable over 24 h at 950 ^oC. Electrochemical tests in 0.5% H_2S-CH_4 showed stable performance at 950 ^oC and 800 ^oC for cells comprising $Ce_{0.9}Sr_{0.1}VO_3$ | YSZ (0.3 mm) | Pt. Comparison of fuel cell performances using 0.5% H_2S-CH_4, 0.5% H_2S-N_2 and 5% H_2S-N_2 as feeds showed that $Ce_{0.9}Sr_{0.1}VO_3$ was not active for oxidation of methane, but highly active for conversion of H_2S. Electrochemical

impedance results were consistent with the finding that the anode was activated only in an environment that contained H_2S. Conductivity measurements showed there was an increase in conductivity in H_2S-containing environments, and that this increase resulted from a change in composition and structure from the oxide to monoclinic $Ce_{0.9}Sr_{0.1}V(O,S)_3$, as evidenced by XPS and XRD analyses.

In order to focus on the catalytic activity of the material under study, a composite anode (CSV + oxide ion conducting or mixed ionic-electronic conducting material) was not investigated.

4.2 Experimental

4.2.1 Catalyst preparation

$Ce_{0.9}Sr_{0.1}VO_3$ (CSV3) and $Ce_{0.9}Sr_{0.1}VO_4$ (CSV4) were prepared by solid state synthesis from the powdered oxide precursors: SrO (Alfa Aeser), CeO_2 (Sigma Aldrich, 99.9%) and V_2O_5 (Alfa Aeser, 98%). The powders were mixed in a ball mill for 24 h, then sintered in alumina boats at 1100 ^{o}C in 10% H_2-Ar (CSV3) and N_2 (CSV4) for 6 h. This procedure was repeated until the desired phase was formed as the single or predominant material, as shown by XRD analysis (Figure 4.2).

4.2.2 Fuel cell testing

Membranes were prepared by painting platinum paste (Heraeus, 1 cm^2) onto YSZ (8 mol% Y_2O_3, Intertec Southwest, 25.4 mm OD, 0.3 mm thick) to form the cathode, and calcining at 900 ^{o}C in air for 1 h. The anode catalyst, either CSV3 or CSV4, was finely ground using a mortar and pestle and dispersed in α-terpineol to form a paste, and a 1 cm^2 area was screen printed onto the opposite face of the electrolyte to form a membrane electrode assembly (MEA). The MEA was pre-sintered in 10% H_2-Ar for 2 h at 1000 ^{o}C. Typical anode thicknesses were about 50 μm, while the cathode thicknesses were 5-10 μm.

The MEA was installed in the fuel cell testing apparatus as shown schematically in Figure 4.1. Gold current collector wires (single probe) with spiral wound ends ran through the length of the inlet tube. During a typical MEA installation, ceramic sealant (Aremco, Type 503) was applied to an end of the outlet anode tube, and the MEA was placed onto the sealant. The sealant was then cured, using the procedure prescribed by Aremco, while the cell was heated at 2 ^{o}C min^{-1} to a prescribed operating temperature, in flowing 1% H_2-N_2 gas. The flow rates of operating fuel cell gas feeds (i.e. air on cathode side and fuel on anode side) then were set using flow controllers (Arbin Instruments Solid Oxide Fuel Cell Test Station, MKS mass flow controllers); flow rates used at each of the anode and cathode sides were 200 mL min^{-1} in all comparative tests. The chamber volume was close to 80 mL; LHSV 150 h^{-1}. Fuel cell testing was conducted with standard DC and AC electrochemical techniques using a Solartron 1287A Potentiostat/Galvanostat (5 mV sec^{-1} sweep rate was

used for potentiodynamic tests) and a Solartron 1252A FRA (electrochemical impedance was analyzed from 1 MHz to 0.5 Hz, at OCV and $\pm$ 20 mV). Fuel cell tests were conducted using a two electrode set-up. The wire resistance was manually compensated by externally measuring the wire resistance at the testing temperature.

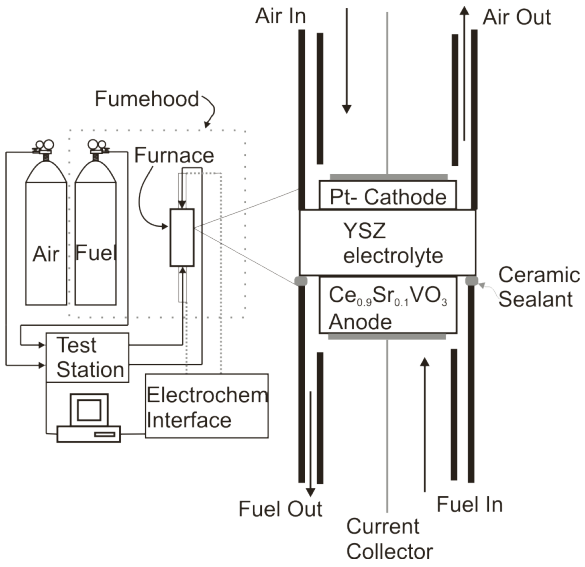

Figure 4.1: Schematic of fuel cell setup.

4.2.3 Conductivity testing

Conductivity measurements were conducted in a commercial NorECs Probostat electrochemical measurement cell using gold mesh current collectors (two probes) in a single gas environment. Cylindrical pellets were prepared by pressing powdered catalyst at 2 tonnes in a 1 cm ID die, and the pellet so formed was fired at 1250 ^{o}C in 1% H_2-N_2 for 2 h. Gold paste was painted on both sides of the pellet and fired at 800 ^{o}C in 1% H_2-N_2 for 1 h. The combinations of anode feed gases used during the tests were 10% H_2-N_2 and 5% H_2S-N_2, each flowing at 50 mL min^{-1}. The samples were heated at 2 ^{o}C min^{-1} and tests were performed at selected temperatures in the range 500 - 950 ^{o}C. Measurements were made using the two point DC conductivity method and the samples were held at each testing temperature until stable conductivity was achieved. Typically, in H_2 atmospheres stable values were obtained 2 h after stabilization at the testing temperature. Under an H_2S-containing environment the sample typically was held at 925 ^{o}C for 24 h before a constant conductivity was achieved, whereas at lower temperatures stable conductivity values were achieved within 2 h.

4.2.4 Chemical stability testing

Chemical stability tests were conducted using powdered samples of anode materials in an alumina boat. The samples were heated in a stream of flowing N_2, held at 1000 ^{o}C in 0.5%

H_2S-CH_4 (Praxair) for 12 h, and then cooled, again in a stream of flowing N_2. Chemical stability was also determined for samples that had been used for conductivity testing. The phase composition of the powders was determined using XRD.

4.2.5 Materials characterization

A Rigaku RU200 Powder x-ray diffraction (XRD) system with a rotating anode and a Co target was used for analysis of all synthesized powders, with a scan rate of 2 $^o\theta$ min^{-1}. The commercially available software Jade was used for identifying phases present in the samples.

A Hitachi S-4800 field emission scanning electron microscope (SEM) was used for characterizing cross-sections of MEAs.

X-ray photoelectron spectroscopy (XPS) was performed on samples using a Kratos Analytical AXIS 165. A monochromated Al Kα (hν = 1486.6 eV) source was used at a power of 210 W, with a base pressure of 3 x 10^{-8} Pa in the analytical chamber. Fixed analyser transmission (FAT) mode was applied with a resolution of 0.55 eV for Ag 3d and 0.70 eV for Au 4f peaks. The analysis spot was 700 x 300 μm. Charge neutralization (current 1.7 A, balance 1.8 V, bias 1.1 V) was applied to compensate for photoelectrons leaving the sample surface. After degassing, survey scans between 1100 and 0 eV were collected at a pass energy of 160 eV, 0.35 eV step size and a dwell time of 200 ms, and were accumulated over three scans. Narrow scans of Ce, V, O and S were collected at 20 eV pass energy, 0.1 eV step size and 200 ms dwell time and 10-20 scans per sample. Spectra were referenced to C 1s binding energy of 283.26 eV, and were fitted using Gaussian-Lorentzian peak shapes and Shirley baselines.

Differential scanning calorimetry thermogravimetric analysis (DSC-TGA) was performed using a TA Instruments SDT Q600. Precisely measured powder samples weighing about 20 mg were placed in an alumina cup (90 μL) under a flowing stream comprising 100 mL min^{-1} N_2 and 1 mL min^{-1} H_2. The sample was heated at 20 ^{o}C min^{-1} to 850 ^{o}C and held for 30 min until the signal stabilized, then the stream to the chamber was switched to 200 mL min^{-1} of 500 ppm-H_2S (in N_2) at a constant temperature for 20 min. The sample was subsequently cooled under N_2.

Quantachrome Instruments Autosorb I was used for BET surface area determinations of the freshly prepared, reduced catalysts using He gas.

4.3 Results

4.3.1 Characterization of anode materials

The XRD pattern of as-prepared CSV3 (PDF# 25-0307) showed that it possessed a perovskite structure with a tetragonal unit cell and lattice parameters a = 5.52 Å and c = 7.81 Å (Figure 4.2a). To form this structure Ce must be present in the 3+ oxidation state, and V predominantly as 3+; the substituent Sr is 2+. Analysis of the XRD pattern of

CSV4 (PDF# 12-0757) (Figure 4.2b) showed a zircon-type tetragonal unit cell, with lattice parameters a = 7.36 Å and c = 6.49 Å. For this structure Ce must be in the 3+ oxidation state, V predominantly as 5+; again, substituent Sr is 2+.

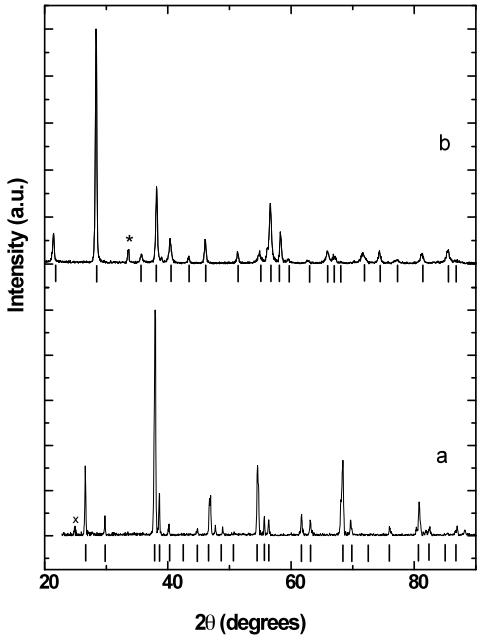

Figure 4.2: XRD patterns of fresh (a) $Ce_{0.9}Sr_{0.1}VO_3$ and (b) $Ce_{0.9}Sr_{0.1}VO_4$.

The BET surface areas of fresh catalyst materials were low, 1.17 m^2 g^{-1} (CSV3) and 2.38 m^2 g^{-1} (CSV4).

4.3.2 Chemical stability of anode materials

XRD analyses conducted after the chemical stability tests of $Ce_{0.9}Sr_{0.1}VO_3$ in 0.5% H_2S-CH_4 showed that the used material retained the structure of fresh material (Figure 4.3 a), and that no discernable amounts of sulphur-containing phases were present. Thus there was no reaction or decomposition of the oxide. However, there was a larger amorphous background between 25 and 35 $2\theta^o$ which was ascribed to carbon present in the powder that had been formed by thermal cracking of methane at 1000 ^{o}C.

CSV4 was reduced in the gas mixture, and the XRD pattern of the tested sample matched that of CSV3 (Figure 4.2 b). Again, there were no sulphur-containing phases present, and the only change was the presence of a stronger background signal of carbon between 25 and 35 $2\theta^o$. In this case it appeared that the carbon included material formed by methane decomposition that flaked from the walls of the quartz tube onto the sample during retrieval. It comprised roughly 5 wt% of the sample.

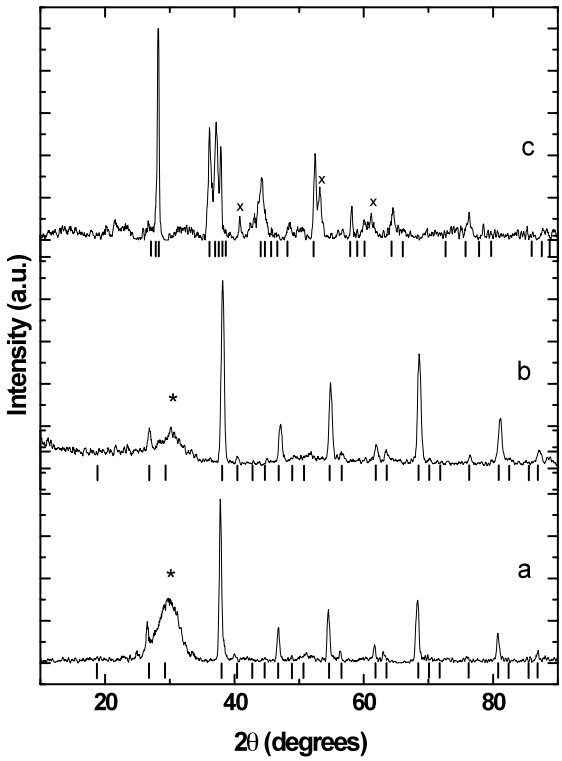

Figure 4.3: XRD patterns of (a) $Ce_{0.9}Sr_{0.1}VO_3$ after stability test, (b) $Ce_{0.9}Sr_{0.1}VO_4$ after stability test and (c) sulfided $Ce_{0.9}Sr_{0.1}VO_3$ formed after conductivity test. (* Indicates amorphous carbon, x are unidentified peaks)

Separate MEAs with CSV4 and CSV3 as anodes screen-printed onto the electrolyte were pre-sintered at 1000 ^oC prior to testing. CSV4 was reduced during the pre-sintering of the MEA in 10% H_2-Ar which, due to a dimensional change of the anode relative to YSZ, led to delamination of the anode from the electrolyte, with consequent high resistance and no useful activity for activation of the fuel. Sintering CSV4 in N_2 and testing under reducing conditions also led to rapid delamination of the anode arising from reduction of the oxide.

In contrast, CSV3 formed a stable bond with the surface of YSZ and, as a result, adhered well to the electrolyte throughout tests. Figure 4.4 shows a cross-sectional SEM image of a CSV3 | YSZ | Pt MEA. It was found that CSV3 was stable under a reducing atmosphere, as the performance of MEAs remained high and stable as long as the cells remained hot. The material was prone to cracking during cool-down. Such cracking may have occurred as a result of differential thermal expansion or contraction between components. However, in the present case we found it most unlikely that there was differential expansion. The interface was stable throughout presintering and testing. During the presintering process there was good adhesion between the pure anode CSV layer and the YSZ electrolyte, even without roughening the surface of the YSZ. Further, during fuel cell testing, in which the anode was exposed to H_2S and a sulfidation reaction occurred, there was no loss in power

density, showing that there was no delamination at that time. Thus there was a stable interface between either the unsulfided anode or the sulfide anode and the electrolyte. It was found that delamination occurred only during cool down, during which it was found that the sealant tended to crack. Thus, while we cannot unequivocally state that there was no differential contraction during cool down, I attributed the cracking to consequences of sealant cracking, possible resulting in oxidation of the anode material.

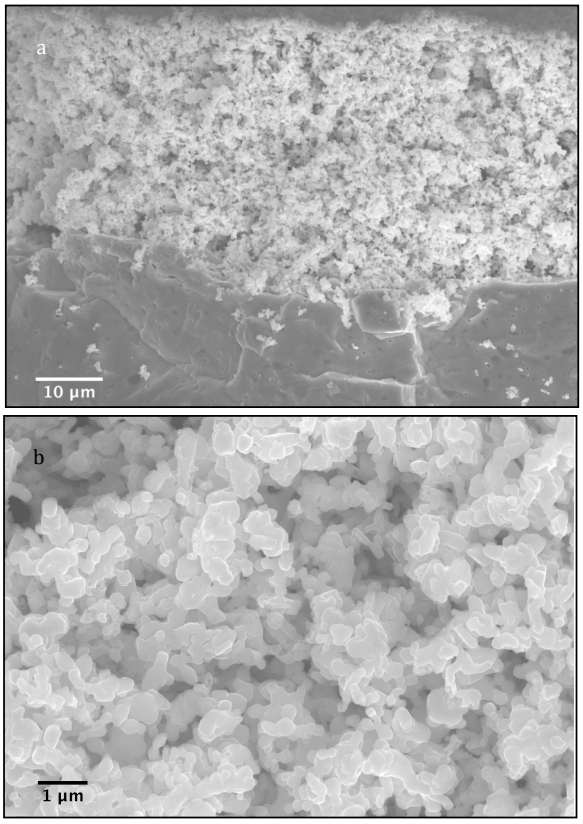

Figure 4.4: SEM image of (a) cross-section of prepared MEA and (b) higher magnification of $Ce_{0.9}Sr_{0.1}VO_3$ anode.

Due to the ease of oxidation of CSV anode materials, the anode feed gas was not humidified.

4.3.3 Electrochemical performance

Potentiodynamic tests were conducted to determine the electrochemical activity of the anode material for conversion of each of methane and H_2S. The MEAs were tested at 950 ^oC and 800 ^oC, in separate tests for each of the feeds 0.5% H_2S-CH_4 (to simulate sour gas), 0.5% H_2S-N_2, 5% H_2S-N_2, and pure CH_4. The initial tests were performed using sour gas, but it was necessary to ascertain if one or both components of the gas contributed to the activity of the cell; hence, I also used H_2S with balance N_2 and pure CH_4 in comparative tests (Figures 4.5 and 4.6). The performances were similar for both 0.5% H_2S-CH_4 and

0.5% H_2S-N_2 at 950 ^oC, but a slight difference was found at 800 ^oC, where use of the 0.5% H_2S-N_2 feed provided a slightly higher power output by about 5 mW cm^{-2}. When the concentration of H_2S was increased to 5%, the performance increased to a maximum power density of 140 mW cm^{-2} (950 ^oC) and 120 mW cm^{-2} (800 ^oC). These values are high for a feed having such a low concentration of H_2S, and so show the high activity of the sulfided anode catalyst for conversion of H_2S [15-21]. At the same time no activity to when using pure H_2 or CH_4 is seen.

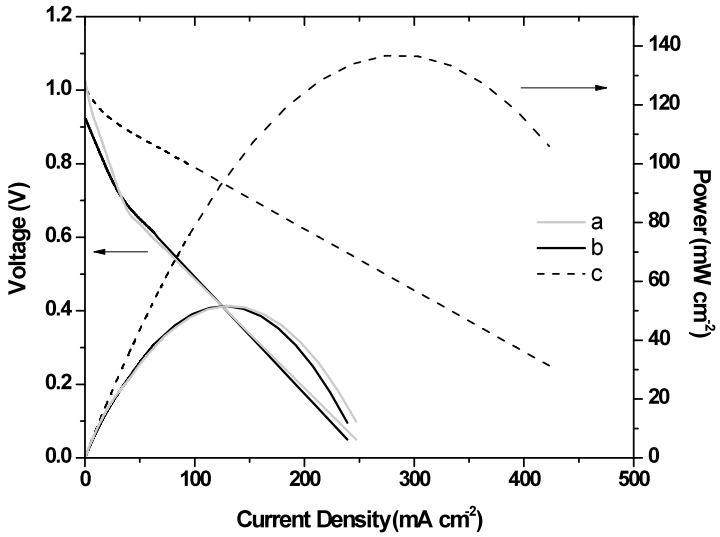

Figure 4.5: Potentiodynamic curves for sulfided $Ce_{0.9}Sr_{0.1}VO_3$ | YSZ | Pt at 950 ^oC in (a) 0.5% H_2S-CH_4 (b) 0.5%H_2S-N_2 (c) 5% H_2S-N_2.

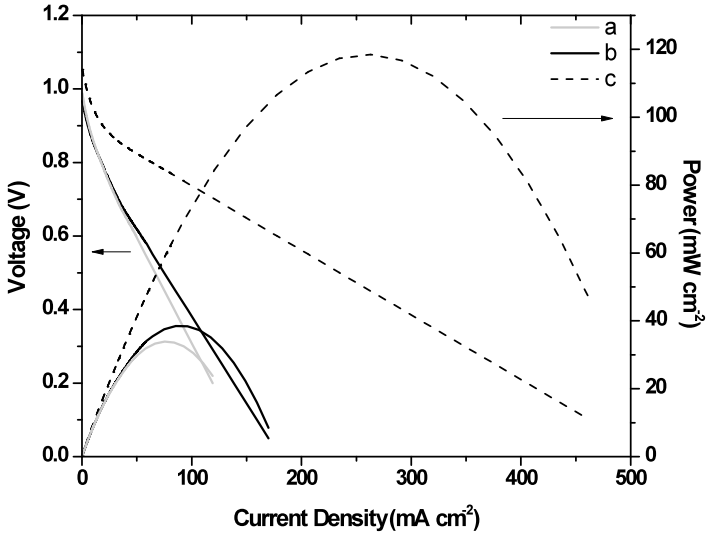

Figure 4.6: Potentiodynamic curves for sulfided $Ce_{0.9}Sr_{0.1}VO_3$ | YSZ | Pt at 800 ^oC in (a) 0.5% H_2S-CH_4 (b) 0.5%H_2S-N_2 (c) 5% H_2S-N_2.

Figure 4.7 shows the impedance spectra for the MEA having the same CSV3 anode at 950 ^oC in different gas mixtures. The impedance arising from diffusion of H_2S to the active sites increased with decreasing H_2S content due to dilution. The high frequency intercept, R_S, did not change significantly between the spectra when using different fuels, and the value for R_{P1} (combined cathode and electrolyte resistance) was also similar in each case. In contrast, the value for R_{P2} (anode resistance) increased two-fold when using 0.5% H_2S-CH_4 and 0.5% H_2S-N_2. The data are summarized in Table 4.1. Impedance spectra were collected at OCV because of the uncertainty in collecting impedance spectra under an applied potential with a two-electrode setup, because the cathode contribution cannot be accurately identified and eliminated. It was found that our OCVs from experiment to experiment were reproducible, and hence the impedance spectra collected were reproducible, varying the AC voltage did not affect the result, except for decreasing noise at the low frequency end. Therefore, the measurements were taken in a linear i-V region.

Figure 4.8 shows the stability of the catalyst in 0.5% H_2S-CH_4 over a 2.5 h period at 80 mA cm^{-2}. There was no degradation of the voltage after an initial decrease, ascribed to conditioning of the catalyst, and there was no detectable carbon deposition on the anode as determined by analysis after cooling to room temperature. If, however, there was an undetected negligible amount of carbon deposited as a result of thermal processes, the amount was so small that it could not be seen either visually or using SEM, and there was no effect on electrochemical performance as there was no increase in overpotential during the galvanostatic tests. However, under more strenuous conditions these and similar catalysts are prone to coking [22].

Due to the complexity of the gas mixture used, including the corresponding reaction products, it was not possible to adequately determine the reaction products at the time of testing. Gas chromatography (GC) and mass spectrometry (MS) are the two most widely used methods for identifying gas phase molecules, at the time of testing GC was the only instrumentation available and identifying and quantifying all of the possible reaction products, at the quantities present was not possible.

Sulfur deposits were seen at the cool anode exhaust gas end after long term electrochemical tests were conducted. Therefore the product gas is most likely S_2, SO_2 is only expected at high current densities which were not achieved using these cells. S_2 is the preffered product since it can be condensed into elemental sulfur and collected as a value-added product, whereas SO_2 requires more sophisticated scrubbing and cataltic reforming to produce sulfuric acid.

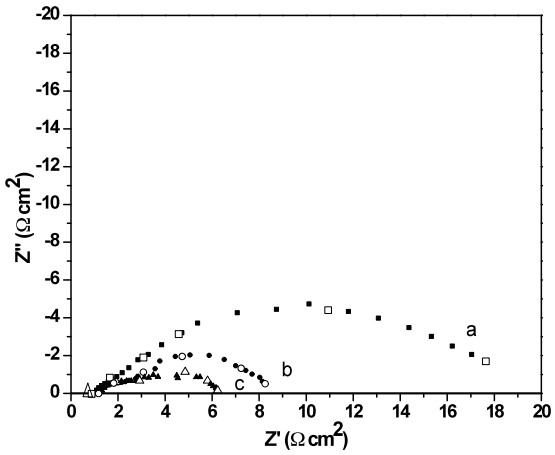

Figure 4.7: Impedance spectra of sulfided $Ce_{0.9}Sr_{0.1}VO_3$ | YSZ | Pt at 950 ^{o}C in (a)0.5% H_2S-CH_4 (b) 0.5%H_2S-N_2 (c) 5% H_2S-N_2. (Frequency decades 1 x 10^5-1 x 10^{-1} are labelled.)

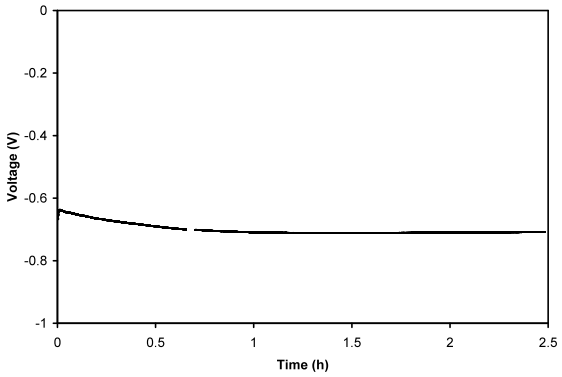

Figure 4.8: Long term galvanostatic test of sulfided $Ce_{0.9}Sr_{0.1}VO_3$ | YSZ | Pt in 0.5% H_2S-CH_4 at 950 ^oC and 40 mA cm^{-2}.

Table 4.1: Summary of impedance results at 950 ^oC (Ω cm^2).

Component	0.5% H_2S-N_2	0.5%H_2S-CH_4	5% H_2S-N_2
R_S	1.2	1.0	1.3
R_P1	1.2	1.0	1.3
R_P2	4.8	10.7	2.0
R_P3	N/A	N/A	2.2

4.3.4 Total conductivity

The total conductivity of CSV3 was determined under a range of conditions to determine the effects of atmosphere and temperature on its electrochemical properties. The conductivity of CSV3 in H_2 increased with increasing temperature (Figure 4.9a), behaviour typical of semiconductors and ionic conductors [23]. The activation energy was 0.106 eV. The conductivity of the same material in H_2S (Figure 4.9b) decreased with increasing temperature, which behaviour is typical of metallic and pseudo-metallic conductors. The conductivity at 925 ^oC increased greatly from a value of 0.41 S cm^{-1} in the H_2-containing environment to 248 S cm^{-1} in the corresponding H_2S-containing environment. The activation energy of conduction in the H_2S containing environment was -0.120 eV, indicating that the conductivity of the anode was pseudo-metallic in character.

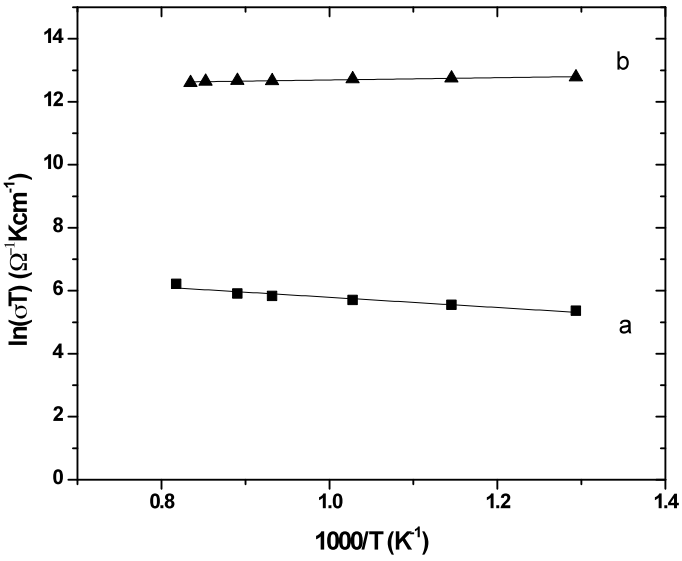

Figure 4.9: Conductivity of (a) $Ce_{0.9}Sr_{0.1}VO_3$ in 10% H_2-N_2, and (b) sulfided catalyst in 5% H_2S-N_2.

XRD and XPS analyses were conducted on both fresh and used pellets to determine whether the change in conductivity was associated with changes in the composition or structure of the material, which were not evident visually. The gold electrode paste was removed, and the pellet was ground to a fine powder. XRD analysis of the powder showed that the material had undergone a chemical reaction with H_2S, to form a material having a structure similar to that of fully sulfided $Ce_{0.9}Sr_{0.1}VS_3$. However, the XRD pattern was not fully consistent with that of $Ce_{0.9}Sr_{0.1}VS_3$, as seen by comparing the peak positions and intensities with that of the sulfide (PDF# 47-1039) (Figure 4.3 c).

4.3.5 Thermal analysis

In order to gain more insight into the reaction that occurred between H_2S and CSV3, the material was exposed to H_2S while under a H_2 atmosphere at 850 ^oC in a DSC/TGA instrument. The weight and heat flow changes were monitored using TGA and DSC respectively (Figures 4.10 a and 4.10 b). The signal was allowed to stabilize for 30 min upon reaching the reaction temperature as some further reduction reaction was occurring to the already reduced sample.

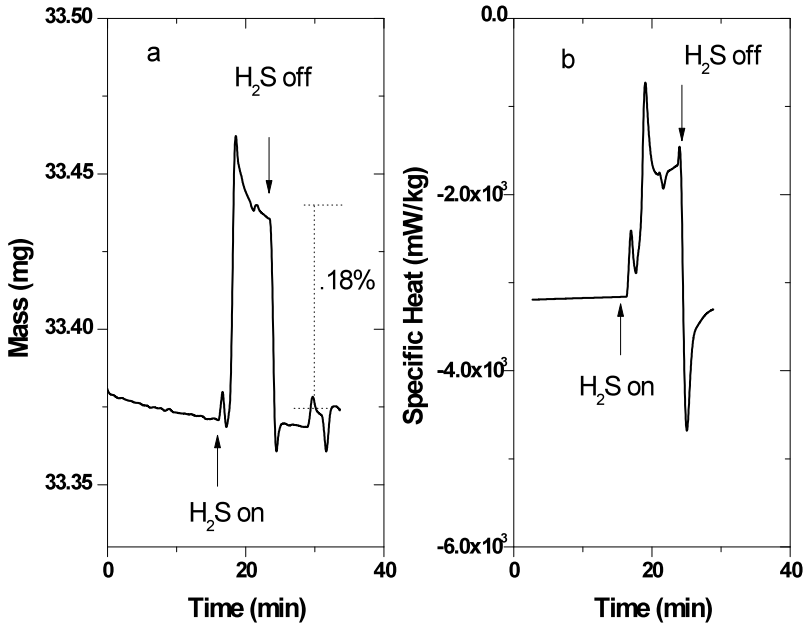

Figure 4.10: Effect on the (a) mass (TGA) and (b) specific heat (DSC) on exposure of CSV3 at 850 ^{o}C to 5000 ppm of H_2S in H_2. (A rising value indicated exothermicity in the DSC.)

There was an initial increase in weight and an exothermic heat flow. The weight gain was 0.07805 mg which, assuming that it is totally ascribable to adsorbed H_2S, constitutes 2.61 x 10^{18} molecules (4.34 x 10^{-6} mol). Assuming that chemisorbed H_2S dissociated to form a monolayer of adsorbed S atoms, and if the catalyst particle geometry was approximated as spherical, this constituted about 15% partial surface coverage. The DSC signal also showed an exothermic peak followed by an increased heat capacity, which was indicative of adsorption and a change in the phase of the material. After 15 min the H_2S flow was stopped and pure H_2 continued to flow, which was followed, starting essentially immediately, by a gradual return to the original weight as the adsorbed S was desorbed as it reacted with H_2 to reform H_2S. In addition, trace amounts of SO_2 were also detected in the effluent, attributed to continuing reaction of sulfur with oxygen anions to form SO_2 and regenerate electrons. Since the DSC/TGA instrument used horizontal beams to position the samples in the reactive gas flow, buoyancy effects were minimized. Blank trials using empty alumina cups did not show the same response as those shown in Figure 4.10, signifying that the reaction measured was adsorption of H_2S onto the catalyst sample.

4.3.6 XPS analyses

XPS was employed to determine the near-surface composition and near-surface ion electronic states of fresh $Ce_{0.9}Sr_{0.1}VO_3$ and the sulfided material, either $Ce_{0.9}Sr_{0.1}VS_3$ or

$Ce_{0.9}Sr_{0.1}V(O,S)_3$, formed during conductivity measurements in 5% H_2S atmosphere. Figure 4.11 shows high resolution sweeps of the main ionic components in the two materials. The compositions and peak locations are summarized in Table 4.2.

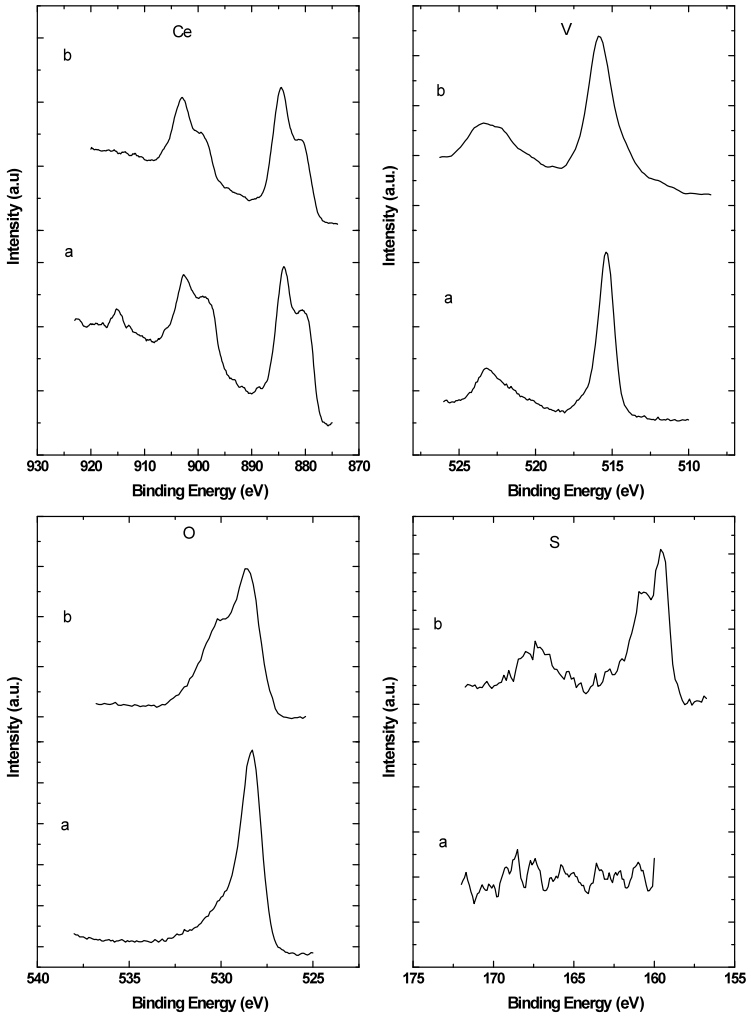

Figure 4.11: XPS spectra for different elements of (a) fresh and (b) sulfided $Ce_{0.9}Sr_{0.1}VO_3$.

Ce had five peaks attributed to $d^{5/2}$ and $d^{3/2}$ orbitals in the fresh sample while there were only four peaks in the spectrum of the sulfided material. The highest energy peak for Ce, at 914.78 eV, was not present after sulfidation. Two peaks at 883.92 eV and 898.03 eV were shifted by about 0.5 eV to higher energies after sulfidation. The increase in binding energy may be related to an increase in oxidation state of a portion of Ce from Ce^{3+} to Ce^{4+} with sulfidation, since a more electropositive bond with S would decrease the binding energy. It is shown below that the ratio of surface total anions/cations did not change by more than a small fraction, and so any partial change in oxidation state was small. Therefore, it may be that the change in peak position was attributable to a change in the

anion bonded to the Ce cations. Although, Ce peaks are notoriously hard to characterize due to many body effects and satellite peaks due to exicitation from unpaired electrons [24]. However, a change in surface state is apparent between the sulfided and unsulfided material, which is also reflected in other XPS peaks.

Bond energy shifts of the V peaks were also detected following sulfidation, as the lowest energy $2p^{3/2}$ peak at 515.35 eV shifted by 1 eV to a lower energy while the higher energy peak stayed at the same energy of 515.6 eV. After sulfidation the two $2p^{1/2}$ peaks appeared to merge into one peak, the value of which was centered between those of the original peaks. The decrease in binding energy of some peaks signified predominantly V-S bonding as opposed to V-O bonding.

The lower energy O peak did not shift in energy, 528.4 eV, but the higher energy peak at 529.63 eV increased by about 0.5 eV. The relative areas of the two peaks (528.3 eV/529.6 eV) also changed with sulfidation from 60/40 to 40/60, evidence that there were two different bonding states present for oxygen and, as shown below, for sulphur as well [25-27], the first being a structural O^{2-}, while the second being a bridging oxygen.

The spectrum for sulphur showed two pairs of overlapping peaks. The lower energy peak was attributed to a structural sulphur, S^{2-}, while the higher energy peak was attributed to a bridging sulphur.

Thus there is a change in the composition of the surface which may have been, for example, from M-O-M(O)-O-M to M-O-M(S)-O-M, or from M-O-M(O)-O-M to M-S-M(O)-O-M either of which would change the ratio of surface O to bridging O, where M indicates a cation, -O- and -S- indicate bridging anions, while (O) and (S) indicate terminal O and S.

The oxygen to metal cation ratio (O/cation) at the surface of fresh CSV3 was 2.3, whereas the sulfided CSV3 had an O/cation ratio of 1.9 and a sulfur to cation ratio (S/cation) of 0.43. Thus the formulation of the sulfided materials is best represented by the formula $Ce_{0.9}Sr_{0.1}V(O,S)_3$, and the ratio of O/S was 4.5 and the surface (O+S)/cation ratio was 2.3. Hence the ratio of total surface anions/cations was in each case close to 2.3.

Table 4.2: Summary of fitted XPS data.

	Ce					V			
CSV	$3d^{5/2}$	$3d^{5/2}$	$3d^{3/2}$	$3d^{3/2}$	$3d^{3/2}$	$2p^{3/2}$	$2p^{3/2}$	$2p^{1/2}$	$2p^{1/2}$
Area	5895	7868	5592	5382	1048	2299	1364	917	627
FWHM	3.2	3.5	4.4	4.3	3.1	1.0	2.2	2.8	1.4
Position (eV)	880.0	883.9	898.0	902.5	914.8	515.4	515.7	521.8	523.2
Concentration	22.8	30.4	21.7	21.0	4.1	44.2	26.2	17.6	12.0
	O								
	1s	1s							
Area	5517	3371							
FWHM	1.2	2.7							
Position (eV)	528.3	529.6							
Concentration	33.9	66.1							
CSV-S									
Area	4531	6760	2089	4846		1577	1956	1365	
FWHM	3.5	3.4	3.0	4.1		3.5	1.5	3.1	
Position (eV)	880.3	884.3	898.6	902.6		514.4	515.6	522.6	
Concentration	24.8	37.0	11.5	26.7		32.2	39.9	27.9	
	O		S						
	1s	1s	2p	2p	2p	2p			
Area	3395	4433	376.9	352.10	196.6	329.8			
FWHM	1.3	2.4	0.9	1.3	2.7	2.8			
Position (eV)	528.5	530.0	159.5	160.7	162.0	167.2			
Concentration	14.0	86.0	28.1	53.6	6.2	12.1			

4.4 Discussion

Due to the instability of CSV4 under reducing conditions, as shown by the changes to the XRD spectra of the material under methane, leading to a phase change and concomitant large dimensional change, this material is not a suitable anode catalyst. Thermodynamic analysis showed that $CeVO_4$ was not stable at low oxygen partial pressures and higher temperatures, as summarized in Figure 4.12. Thermochemical data for this analysis were obtained from reference [28] and the analysis was conducted according to the procedure developed by Yokokawa et al. [29]. Hence, assuming non-doped structures of $CeVO_3$ and $CeVO_4$, the reduction shown in (4.1) under reducing atmospheres (0.5% H_2S-CH_4 or 10% H_2-N_2) was to be expected.

$$CeVO_4 \rightarrow CeVO_3 + 1/2O_2 \tag{4.1}$$

$$\Delta G_{rxn} = \Delta G_f(CeVO_3) + 1/2\Delta Gf(O_2) - \Delta G_f(CeVO_4) \tag{4.2}$$

The plot of dependence of partial pressure of oxygen on temperature, Figure 4.12, is derived from reactions (4.1) and (4.2). Because $CeVO_4$ readily undergoes reduction by loss of oxygen, the primary focus in this work was on structural and electrochemical characterization of CSV3.

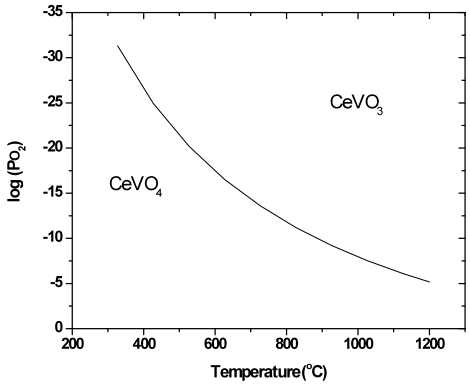

Figure 4.12: Thermodynamic stability regions for $CeVO_3$ and $CeVO_4$.

The XRD of anode samples CSV3 (Figure 4.3 a) that were treated in the fuel gas atmosphere showed that there were no changes to the bulk crystal structure. However, a strong background signal was clearly evident, due to carbon deposited on the entire quartz tube as a result of CH_4 decomposition during the test which then flaked off onto the sample during extraction. It is interesting that these findings differed from the XRD pattern of the tested material after conductivity measurements (Figure 4.3 c) which showed the formation of $Ce_{0.9}Sr_{0.1}V(O,S)_3$. This result is most likely due to the difference in concentration of H_2S, which was ten times greater in the conductivity measurement case, as well as the

lower oxygen partial pressure in the conductivity setup. The susceptibility of the material to sulfidation and the degree of sulfidation appeared to be a function of the amount of H_2S under conductivity conditions, since during the chemical stability test the material did not appear to be sulfided to any significant degree. This suggests very fast oxygen-sulfur ionic exchange kinetics under polarization conditions. The DSC/TGA data (Figure 4.10) showed that saturation of adsorbed H_2S species happened very rapidly at 850 ^oC.

It is noteworthy that sulfidation was not accompanied by any significant redox reaction. The ratio of total surface anions/cations in each of the unsulfided and sulfided materials was close to 2.3, indicating that the primary reaction on sulfidation was replacement of O^{2-} by S^{2-}, and was not oxidation.

Potentiodynamic tests showed that the CSV3 anode was inactive towards CH_4; in fact, no current withdrawal was possible under either pure methane or pure hydrogen. The cell showed no activity upon heating in H_2, and the ohmic resistance of the cell was high, typically 10 Ω cm^2 or greater. Upon introduction of H_2S fuel the resistance dropped and the activated catalyst was highly active towards H_2S, but remained inactive to H_2 and CH_4. This interpretation is fully consistent with the changes in the impedance spectra (Figure 4.7). The polarization resistance, as characterized by the second semicircle (the first semicircle is ascribed to the reaction at the Pt cathode), increased when in the presence of only N_2 and CH_4, and decreased when H_2S was present, especially at higher concentrations. The anode was active for H_2S electro-oxidation, whether the fuel stream was diluted with either or both of N_2 and CH_4. Each diluent impeded the gas phase diffusion of H_2S to the active sites. Under OCV conditions methane impeded the conversion of H_2S more than N_2, and so the semicircle was larger when methane was the diluent. The cause of this effect may be reversible adsorption of methane at catalyst sites, as shown by the high OCV in the presence of methane, a characteristic of the methane electro-oxidation reaction. However, under polarization conditions the IV curves were similar for each mixed feed of the same H_2S concentration, consistent with conversion of only H_2S. Increasing the H_2S concentration ten-fold led to a three-fold increase in fuel cell performance, attributed wholly or in large part to a 1 Ω cm^2 decrease in the anode polarization resistance, R_{P2}. These results indicated that the CSV3 anode was highly active towards H_2S, similar to the activity for the related oxide anode $La_{0.7}Sr_{0.3}VO_3$ [1-4].

Gas phase pyrolysis of CH_4 occurs at 950 ^oC, thus there is a possibility that H_2 is produced. However, since there was no change in performance with N2 or CH4 as the dilutent, even if there was H_2 produced it did not participate in the reaction, no carbon was detected on the anodes, nor the tubing after the end of testing. Carbon deposition on CSCV anodes is addressed in §6, but briefly, there is virtually no carbon present on these anodes when exposed to pure CH_4 fuel.

It is noteworthy that the activity of the anode catalyst under thermal catalytic oxidation conditions [12-14] differed from that under the above fuel cell conditions. Whereas the

catalyst converted both H_2S and CH_4 in the presence of an atmosphere containing oxygen, the electrochemical process oxidized only H_2S. Thus it appears that conversion of CH_4 requires a significantly elevated concentration of O species at the catalyst surface, and this did not occur under fuel cell operating conditions, especially in the presence of H_2S [29].

The conductivity change resulting from the conversion of the oxide to sulfide was consistent with the low performance of the material in non-H_2S-containing feed gases, and also explained why the performance was so similar at 800 ^oC and at 950 ^oC, since the conductivity was higher at the lower temperature. The increase in conductivity was balanced by a decrease in ionic conductivity as well as activation polarization. The stability of CSV3 towards carbon deposition and sulfur poisoning, as opposed to activation as a result of sulfidation, was confirmed by stability of performance during long-term electrochemical tests.

The OCV in all cases was higher than that predicted by the Nernst equation for the pure components (e.g., OCV for CH_4 theoretically is 1.04V, experimentally 1.2V), which may be a consequence of changes in the partial pressures of the components of the gas due to secondary reactions occurring in the gas phase while the gas traveled through the heated mullite tube towards the reaction zone [2].

Substitution of a multivalent rare earth cation, $Ce^{3+/4+}$ for La^{3+} in $Ce_{0.9}Sr_{0.1}VO_3$ resulted in an improvement in performance in 5% H_2S-N_2 at 950 ^oC [2]. The conductivity of CSV3 was similar to that of $LaVO_3$, but only approached that of Sr substituted $LaVO_3$ after the sulfidation reaction [3]. Therefore, the activity of CSV3 can be ascribed to an improvement in activity for H_2S electro-oxidation. It is not clear whether the same transition from oxide to sulfide also occurred in $LaVO_3$, as thermodynamic calculations and stability tests indicated that it is thermally stable in H_2S [4].

The XPS results clearly showed the presence of both oxygen and sulfur species in the sulfided material. Furthermore, a predominant amount of oxygen, relative to sulfur, was present in the near-surface. Quantatative analysis of the XPS spectra for O and S relative to the cationic spectra showed the O/cation ratio decreased slightly after sulfidation, and the ratio of O/cation was four and a half times as large as the S/cation ratio, but that the total surface anion/cation ratio was approximately constant. The nature of the samples and the testing apparatus made it impossible to fully shield the sample from atmosphere after testing. Based on research by Lau and Fang [24], exposure of samples of lanthanum oxide, lanthanum hydroxide and lanthanum oxysulfide to atmosphere did not produce experimentally significant changes in their XPS patterns. Therefore, I expected that any oxygen adsorbed from the atmosphere would be small and would not significantly affect our XPS data.

With sulfidation, a small fraction of Ce^{3+} may have been partly oxidized to Ce^{4+} to accommodate the oxysulfide. However, as the overall anion/cation ratio was unchanged, it is more likely that the shift in positions of XPS peaks was caused by a change in anion species

to which Ce cations were neighbours. The peaks for V^{3+} also underwent consequential small shifts after sulfidation, again probably due to bonding of V with sulfur. The V ionic ratios did not appear to change, as indicated by the relative peak areas, indicating that the oxidation state did not change. Therefore, Ce and V both participated in some manner in the sulfidation reaction, which provided a different mechanism from low temperature oxidation of H_2S on $CeVO_4$, where only $Ce^{3+/4+}$ was found to participate in the reaction [31].

For effective, stable operation of a fuel cell, the anode material must be electronically and ionically conductive. CSV3 was used as a single component mixed ionic and electronic conducting catalyst. Thus, during fuel cell testing when the anode underwent the phase transformation from $Ce_{0.9}Sr_{0.1}VO_3 \rightarrow Ce_{0.9}Sr_{0.1}V(O,S)_3$ in a H_2S containing environment, it must have sustained the reaction by continuing to conduct oxygen ions. In the fuel cell with a potential and chemical gradient in effect across the membrane, conducting oxygen ions from the electrolyte into the anode structure would have kept replenishing the structure with structural oxygen. Thus the anode material in the MEA always included some steady proportion of both oxide and sulfide ions, with the formula $Ce_{0.9}Sr_{0.1}V(O,S)_3$, since the MEA retained its activity for extended periods of time, as found during operation under galvanostatic conditions.

The DSC/TGA results revealed important information regarding what occurred to the anode during fuel cell testing. The initial exothermic peak and final endothermic peaks shown in Figure 4.10 b were attributed primarily to adsorption and desorption of H_2S on the surface as the materials underwent chemical reactions (4.3-4.5):

$$H_2S(g) + 2* \rightarrow *HS + *H \rightarrow *S + *2H \tag{4.3}$$

$$2 * H + O^{2-} \rightarrow H_2O(g) + 2e^- \tag{4.4}$$

$$* S + 2e^- \rightarrow S^{2-} \tag{4.5}$$

H_2S adsorbed onto the surface dissociated according to reaction 4.3 to form surface *HS and *H species, and *HS further dissociated to *H and *S species. When surface *H reacted with O^{2-} species, reaction 4.4, the released electrons then ionized the adsorbed *S according to reaction 4.5. I propose that the ionized S^{2-} diffused into the structure of $Ce_{0.9}Sr_{0.1}VO_3$, substituted for O^{2-}, and so formed $Ce_{0.9}Sr_{0.1}V(O,S)_3$. Once the majority of surface oxygen was removed, the reactants were depleted and the reaction no longer proceeded at the same rate. However, in the electrochemical environment of the fuel cell there was an applied O^{2-} flux that replenished the oxide ion concentration.

Hydrogen sulfide has two possible electrochemical oxidation reactions in fuel cells reactions 3.17 and 3.18, and a third oxidation reaction of the product S_2 by reaction 3.19. Additionally, indirect conversion can be accomplished via two further chemical reactions, a thermal decomposition reaction 3.20 and a reforming reaction (Claus reaction) 3.21. The

nature of each of these reactions is complex, and involves adsorption, dissociation, electron transfer, bond formation, and desorption steps.

H_2S chemisorbs on the surface of the anode where, most likely, it is attracted by the V^{3+} sites. It dissociates to H^+ and S^{2-} which, with electron transfers, electrochemically react with either O^{2-} (transferred from the cathode) or with other S species (from other dissociated H_2S molecules or the sulfided anode) to form the products H_2O, S_2 or SO_2.

One possible means by which the anode operated was that reduced CSV3 was present near the electrolyte, while the rest of the anode was $Ce_{0.9}Sr_{0.1}V(O,S)_3$. The oxide portion provided the O^{2-} anions for the reactions that occurred on the active layer of the anode which consisted of $Ce_{0.9}Sr_{0.1}V(O,S)_3$ with the actual reaction occurring at triple phase boundaries throughout the anode. As Ferrizz et al. have shown [31], the oxidation state and S content in the Ce-O-S system are dependent on both temperature and partial pressures of both oxygen and sulfur. Thus it was possible to have a gradient of concentrations of oxide and sulphide ions within the structure of the anode under reaction conditions.

A second explanation for the activity of the anode, and more plausible explanation based on the available evidence, is that the structure of a part or all of the anode itself changed from tetragonal to monoclinic with very little sulfur content, while the bulk of the lattice sites were still occupied by oxygen. This, too, would be consistent with the stability of the oxide ion conduction in the fuel cell mode. The DSC/TGA data also supported this hypothesis because the weight of the sample did not continue to increase with exposure to H_2S under non-conductive conditions, meaning that there was no additional uptake of H_2S onto the material, and no migration of sulphide ions into the bulk under DSC/TGA experimental conditions. Furthermore, the XPS data also supported this conclusion, as the amount of bound oxygen in the near-surface was over four times greater than bound sulfur. The XRD data also showed that there were intensity differences for some peaks, which can be explained by O occupying S sites, resulting in a lower intensity due to O scattering, so that it textured the XRD signal. The co-existence of S within oxide structures was found for NiO saturated with S, and for NiO-Ni_3S_2 [33]. However, in those situations the presence of sulfide caused a decrease in the conductivity by binding electron holes to the S anions. Furthermore, Lince and Hilton found that O content in the structure of sputtered MOS_2 films was on the order of 10-20 at%, thus forming $MoS_{2-x}O_x$, which had a significant effect on the tribological properties of that material [34].

While the available evidence does not allow full elucidation of the phenomena occurring in the anode catalyst material during use under electrochemical operations, the evidence makes it clear that the partially sulfided catalyst $Ce_{0.9}Sr_{0.1}V(O,S)_3$ is very effective for conversion of H_2S and is not active for conversion of methane or H_2 diluents.

Interestingly, the electrochemical data show no dependence of conductivity of the material (ohmic resistance) on concentration of H_2S. The TG-DSC measurements were made in a 500 ppm H_2S stream. The XPS data were for the material exposed to 5% H_2S. The

data correlated well as the S surface coverage was about 15% as determined by TGA and 13% from XPS, essentially similar values despite the difference in H_2S concentrations. Thus the extent of the sulfidation reaction appears to reach a limiting or equilibrium extent at a concentration at or below 500 ppm H_2S.

In order to focus on the catalytic activity of the material under study, a composite anode (CSV + oxide ion conducting or mixed ionic-electronic conducting material) was not investigated. However, owing to the high electronic conductivity (and most likely a low ionic conducivity). Much better results can be obtained with the additon of YSZ or GDC to the anode. In the current case the boundary between the anode catalyst and the YSZ electrolyte are most likely the only sites of activity.

4.5 Conclusions

New Ce- and V-containing perovskite and zircon-type oxide anode materials were tested in H_2S- and CH_4-containing atmospheres. I found that:

- $Ce_{0.9}Sr_{0.1}VO_4$ anodes were reduced in 0.5% H_2S-CH_4 and in H_2-containing atmospheres. Due to the dimensional changes associated with the reduction of the oxide when bonded to an electrolyte, this material was not a suitable SOFC anode.

- $Ce_{0.9}Sr_{0.1}VO_3$ anodes are chemically stable in 0.5% H_2S-CH_4 at 950 ^oC for 12 h under non-electrochemical conditions, but $Ce_{0.9}Sr_{0.1}V(O,S)_3$ was formed under 5% H_2S during conductivity measurements, as determined using XRD and XPS analyses.

- The total conductivity of $Ce_{0.9}Sr_{0.1}VO_3$ in H_2 was several orders of magnitude lower than in H_2S environment. The nature of the conductivity changed from semiconducting to metallic semiconducting. XPS and XRD measurements showed the formation of $Ce_{0.9}Sr_{0.1}V(O,S)_3$ which explains the changes in conductivity.

- $Ce_{0.9}Sr_{0.1}VO_3$ anodes had high activity only after the introduction of H_2S to the fuel feed. A possible explanation for the sustainable electrochemical activity of sulfided $Ce_{0.9}Sr_{0.1}VO_3$ catalyst, consistent with XPS, XRD and DSC/TGA results, is that the structure of the anode must contain a significant portion of O^{2-} to sustain fuel cell activity; such a structure was denoted as $Ce_{0.9}Sr_{0.1}V(O,S)_3$.

- After initially forming $Ce_{0.9}Sr_{0.1}V(O,S)_3$ the anodes were only active towards the oxidation of H_2S in the fuel feed. A maximum power density of 140 mW cm^{-2} was achieved at 950 ^oC in 5% H_2S-N_2.

4.6 References

[1] Z. Cheng, S. Zha, L. Aguilar, D. Wang, J. Winnick, M. Liu, Electrochem. Solid-State Lett., 9 (2006) A31-A33.

[2] L. Aguilar, S. Zha, Z. Cheng, J. Winnick, M. Liu, J. Power Sources, 135 (2004) 17-24.
[3] Z. Cheng, S. Zha, L. Aguilar, M. Liu, Solid State Ionics, 176 (2005) 1921-1928.
[4] Z. Cheng, S. Zha, M. Liu, J. Electrochem. Soc., 153 (2006) A1302-A1309.
[5] Z. Cheng, M. Liu, J. Electrochem. Soc., 155 (2008) B449-B454.
[6] C. Sun, U. Stimming, J. Power Sources, 171 (2007) 247-260.
[7] J.W. Fergus, Solid State Ionics, 177 (2006) 1529-1541.
[8] J.B. Goodenough, Y.H. Huang, J. Power Sources, 173 (2008) 1-10.
[9] E.V. Tsipis, V.V Kharton, J.R. Frade, J. Eur. Ceram. Soc., 25 (2005) 2623-2626.
[10] A. Watanabe, J. Solid State Chem., 153 (2000) 174-179.
[11] C. Reiichi, Y. Bunichi, S. Yoji, T. Yoshitaka, A. Masayasu, Japanese Patent, JP2004186148A.
[12] C.T. Au, W.D. Zhang, H.L. Wan, Catal. Lett., 37 (1996) 241-246.
[13] K.-T. Li, Z.-H. Chi, Appl. Catal. A, 206 (2001) 197-203.
[14] M. Bellakki, T. Baidya, C. Shivakumara, N. Vasanthacharya, M. Hegde, G. Madras, Appl. Catal. B, 84 (2008) 474-481.
[15] H.P. He, A. Wood, D. Steedman, M. Tilleman, Solid State Ionics, 179 (2008) 1478-1482.
[16] K. Haga, S. Adachi, Y. Shiratori, K. Itoh, K. Sasaki, Solid State Ionics, 179 (2008) 1427-1431.
[17] Z. Cheng, M. Liu, Solid State Ionics, 178 (2007) 925-935.
[18] M. Gong, X. Liu, J. Trembly, C. Johnson, J. Power Sources, 168 (2007) 289298.
[19] C M. Grgicak, J.B. Giorgi, J. Phys. Chem. C, 111 (2007) 15446-15455.
[20] C. M. Grgicak, M. M. Pakulska, J.S. OBrien, J. B. Giorgi, J. Power Sources, 183 (2008) 26-33.
[21] C M. Grgicak, R.G. Green, J.B. Giorgi., J. Power Sources, 179 (2008) 317-328.
[22] N. Danilovic, V. Alzate-Restrepo, Z.R. Xu, K.T. Chuang, J.M. Hill, J.L. Luo, A.R. Sanger, Applied Catalysis: A, to be submitted.
[23] C. Kittel, Introduction to Solid State Physics, 8th ed., Wiley, Berkley CA, 2005.
[24] E. Beche, P. Charvin, D. Perarnau, S. Abanades, G. Flamant, Surf. Interface Anal., 40 (2008) 264267.
[25] N.T. Lau, M. Fang, J. Catal., 179 (1998) 343-349.
[26] D. Gonbeau, C. Guimon, G. Pfister-Guillouzo, A. Levasseur, G. Meunier, R. Dormoy, Surf. Sci., 254 (1991) 81-89.
[27] D. Lichtman, J.H. Craig, Jr., V. Sailer, M. Drinkwine, Appl. Surf. Sci., 7 (1981) 325-331.
[28] M. Dorogova, A. Navrotsky, L.A. Boatner, J. Solid State Chem., 180 (2007) 847-851.
[29] H. Yokokawa N. Sakai, T. Kawada, M. Dokiya, Solid State Ionics, 52 (1992) 43-56.
[30] M. Mogensen, K. Kammer, Annu. Rev. Mater. Res., 33 (2003) 321-331.
[31] S. Yasyerli, G. Dogu, T. Dogu, Catal. Today, 117 (2006) 271-278.

[32] R.M. Ferrizz, R.J. Gorte, J.M. Vohs, Appl. Catal. B, 43 (2003) 273-280.
[33] V.B. Tare, J.B. Wagner, J. Appl. Phys, 54 (1983) 252-257.
[34] J. R. Lince, M.R. Hilton, Surf. Coat. Technol., 43/44 (1990) 640-651.

Chapter 5

Effect of substitution with Cr^{3+} and addition of Ni on the physical and electrochemical properties of $Ce_{0.9}Sr_{0.1}V_{0.5}O_3$ as a H_2S-active anode for solid oxide fuel cells

5.1 Introduction

After the inital work on $Ce_{0.9}Sr_{0.1}VO_3$ (CSV) as a potential anode catalyst for the direct oxidation of 0.5% H_2S-containing CH_4, described in §4, it was found that, even though the material had exceptional conductivity and produced a significant power density of 140 mW cm^{-2} from the electrocatalytic oxidation of up to 5% H_2S-N_2, it was not active towards methane electro-oxidation [1]. The CSV catalyst was fully active only on partial sulfidation, which resulted in a structure change from a tetragonal to a monoclinic perovskite structure with partial anion site occupation by both S^{2-} and O^{2-}.

In an attempt to activate the material to CH_4, I chose to dope CSV with chromium oxide, Cr_2O_3, a known hydrocarbon oxidation catalyst which has a wide oxidation state stability range from P_{O_2}=1 atm to P_{O_2}=10^{-20} atm [2,3]. In this chapter I show that partial substitution of Cr for V in CSV to form $Ce_{0.9}Sr_{0.1}Cr_{0.5}V_{0.5}O_3$ (CSCV) improves redox stability of the catalyst, but by itself does not confer significant activity for methane conversion. A fuel cell comprising $Ce_{0.9}Sr_{0.1}Cr_{0.5}V_{0.5}O_3$ | YSZ (0.3 mm) | Pt had a maximum power density of 85 mW cm^{-2} in 0.5% H_2S-CH_4 at 850 ^oC, arising only from the electroxidation of H_2S.

In order to investigate the possibility of adding a secondary catalytic component to oxidize CH_4, Ni was added to CSCV. Ni is also a well known CH_4 oxidation catalyst [4]. Hence I used a combination of CSCV and Ni for electro-oxidation of a feed having both H_2S and methane. Using the same thick membrane, promotion of the anode with 5 wt% NiO increased the total anode electro-oxidation activity to afford maximum power density of 100

mW cm^{-2} with 0.5% H_2S-CH_4 feed. The same membrane provided 30 mW cm^{-2} in pure CH_4, showing that the incremental improvement arose substantially from CH_4 conversion. In addition, I showed that a cermet comprising a combination of CSCV, Ni and YSZ had enhanced activity for methane electro-oxidation. Performance of each anode was stable for over 12 h at maximum power output.

XPS and XRD analyses showed that an increase in conductivity of $Ce_{0.9}Sr_{0.1}Cr_{0.5}V_{0.5}O_3$ in H_2S-containing environments resulted from a change in composition and structure from the tetragonal oxide to monoclinic $Ce_{0.9}Sr_{0.1}Cr_{0.5}V_{0.5}(O,S)_3$. However, the cermet composite had a different sulfidation behavior, most likely associated with NiS formation in addition to forming the CSCV oxysulfide, which could compromise the long term performance of the cermet.

5.2 Experimental

5.2.1 Catalyst preparation

$Ce_{0.9}Sr_{0.1}VO_3$ (CSV) and $Ce_{0.9}Sr_{0.1}Cr_{0.5}V_{0.5}O_3$ (CSCV) were prepared by solid state synthesis from the powdered oxide precursors: SrO (Alfa Aeser), CeO_2 (Sigma Aldrich, 99.9%), V_2O_5 (Alfa Aeser, 98%) and Cr_2O_3 (Alfa Aesar, 99%). The powders were mixed in a ball mill for 24 h, then sintered in alumina boats at 1100 ^oC in 1% H_2-Ar for 6 h. This procedure was repeated until the desired phase was formed as the single or predominant material, as shown by XRD analysis (Figure 5.1). For CSCV fuel cell anodes, a nanopowder was prepared by the gel combustion synthesis method. Briefly, the procedure commenced by dissolving V_2O_5 in nitric acid, then mixing stoichiometric amounts of the nitrate salts $Ce(NO_3)\cdot 6H_2O$ (Acros Organics, 99.5%), $Sr(NO_3)_2$ (Alfa Aesaer, 99%) and $Cr(NO_3)_3\cdot 9H_2O$ (Acros Organics, 99%). The mixture was stirred continuously on a hot plate at 90 ^oC. Citric acid was added to form a 2:1 ratio of metal ions to acid. Ammonium hydroxide (Fisher Scientific) was added to balance the pH to 7. The mixture was stirred further on the hot plate at 90 ^oC for several hours until the water had evaporated. The temperature was increased to 100 ^oC to form the sol-gel, followed by an increase to 300 ^oC to combust the gel. The porous foam formed after combustion was finely ground, then calcined in air at 900 ^oC for 2 h. The mixture subsequently was reduced in 1% H_2-Ar at 1100 ^oC for 2 h to form the required phase.

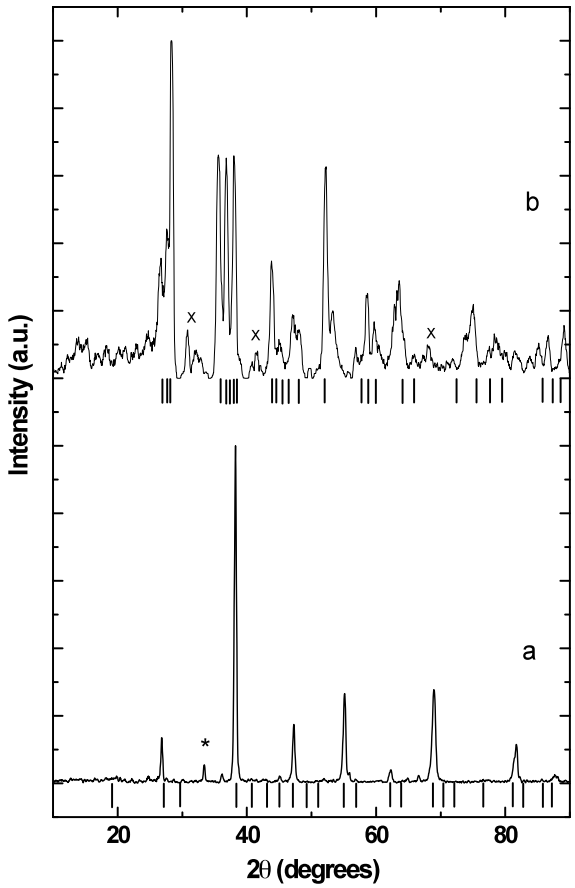

Figure 5.1: XRD patterns of a) $Ce_{0.9}Sr_{0.1}Cr_{0.5}V_{0.5}O_3$ (vertical lines indicate PDF# 25-0307) and b) sulfided$Ce_{0.9}Sr_{0.1}Cr_{0.5}V_{0.5}O_3$ formed after conductivity test (vertical lines indicate PDF# 47-1039). (* indicates a small CeO_2 signal, x indicates an unknown phase)

NiO was synthesized as a nanopowder by the same combustion synthesis method using $Ni(NO_3)_2{\cdot}6H_2O$ (Alfa Aesar, 99.9985%), the gel from which was combusted and heated to 900 ^oC for 2 h.

NiO, CSCV and YSZ (Inframat Advanced Materials, 99.9%) were ball milled in a weight ratio of 5:47.5:47.5 for 24 h to form an intimately mixed composite anode NiO-CSCV-YSZ (NCY).

5.2.2 Fuel cell testing

The anode catalyst (CSCV or NCY) powder was ground using a mortar and pestle, dispersed in α-terpineol to form a paste, and a 1 cm^2 area anode was screen printed onto a YSZ disk (8 mol% Y_2O_3, Intertec Southwest, 25.4 mm diameter, 0.3 mm thick) electrolyte. The disk was pre-sintered in 1% H_2-Ar for 2 h at 1000 ^oC. Prior to testing, the cathode was prepared by painting platinum paste (Heraeus, 1 cm^2) onto the cathode side of the button cell, and the membrane assembly (MEA) was fired in-situ during the fuel cell test ramp-up.

Typically, anode thicknesses were ca. 50 μm, while the cathode thickness was 5-10 μm.

The MEA was installed in the fuel cell testing apparatus as shown and described in Figure 4.1. The anode and cathode chamber gas flow rates were each 100 mL min^{-1}, and the chamber volume was close to 80 mL, so the LHSV was about 75 h^{-1}.

Fuel cell tests were conducted using standard DC and AC electrochemical techniques with a two electrode set-up, a Solartron 1287A Potentiostat/Galvanostat (5 mV sec^{-1} sweep rate was used for potentiodynamic tests) and a Solartron 1252A FRA (electrochemical impedance was analyzed from 1 MHz to 0.5 Hz, at OCV and $\pm$ 20 mV). The wire resistance was manually compensated by externally measuring the wire resistance at the testing temperature.

5.2.3 Conductivity testing

Conductivity measurements were conducted in a commercial NorECs Probostat electrochemical measurement cell using gold current collectors (two probes) in a single gas environment. Cylindrical pellets were prepared by pressing powdered catalyst at 2 tonnes in a 1 cm ID die, and the pellet so formed was fired at 1250 ^{o}C in 1% H_2-N_2 for 2 h. Gold paste was painted on both sides of the pellet and fired at 800 ^{o}C in 1% H_2-N_2 for 1 h. The combinations of gases used during the tests were 10% H_2-N_2 and 5% H_2S-N_2, each flowing at 50 mL min^{-1}. The samples were heated at 2 ^{o}C min^{-1} and tests were performed at selected temperatures in the range 500 - 950 ^{o}C. Measurements were made using the two-point DC conductivity method. The samples were held at testing temperature until a stable conductivity value was reached. Typically, in H_2 atmosphere stable values were obtained 2 h after stabilization of the testing temperature. Under a H_2S-containing environment the sample typically was held at 925 ^{o}C for 24 h before constant conductivity was achieved, whereas at lower temperatures stable conductivity values were achieved within 2 h.

5.2.4 Thermo-chemical characterization

Simultaneous differential scanning calorimetry thermogravimetric analysis (DSC-TGA) was performed using a TA Instruments SDT Q600. The instrument has a horizontal balance which reduces buoyancy effects of the gas and prevents damage to the balance housing from reducing or corrosive gases.

For H_2S stability tests, an accurately weighed ca. 20 mg powder sample was placed in an alumina cup (90 μL). The chamber was purged for 1 h. The sample was heated in a gas mixture comprising 100 mL min^{-1} N_2 and 1 mL min^{-1} of H_2 (1% H_2) at 20 ^{o}C min^{-1} to 850 ^{o}C at which temperature it was held for 30 min until the signal stabilized. A feed comprising 500 ppm of H_2S (in N_2) flowing at 200 mL min^{-1} was then introduced to the chamber and maintained for 20-30 min. The sample was subsequently cooled in flowing N_2.

For oxidation-reduction measurements, an accurately measured sample of about 10 mg of powder was placed in an alumina cup (90 μL), then the system was purged for 30 min

using 100 mL min^{-1} flowing N_2 prior to testing. The samples were then heated to 1100 ^oC at 10 ^oC min^{-1} separately in each of the test gases: N_2, air and 1% H_2-N_2, flowing at 100 mL min^{-1}.

5.2.5 Materials characterization

A Rigaku RU200 Powder X-ray diffraction (XRD) system with a rotating anode and a Co target was used for analysis of all synthesized powders, with a scan rate of 2 θ^o min^{-1}. The commercially available software Jade was used for identifying phases present in the samples.

A Hitachi S-4800 field emission scanning electron microscope (SEM) was used for characterizing the cross-sections of MEAs.

X-ray photoelectron spectroscopy (XPS) was performed on the samples in a Kratos Analytical AXIS 165. A monochromated Al Kα (hν = 1486.6 eV) source was used at a power of 210 W, with a base pressure of 3 x 10^{-8} Pa in the analytical chamber. Fixed analyser transmission (FAT) mode was applied with a resolution of 0.55 eV for Ag 3d and 0.70 eV for Au 4f peaks. The analysis spot was 700 x 300 μm. Charge neutralization (current 1.7 A, balance 1.8 V, bias 1.1 V) was applied to compensate for photoelectrons leaving the sample surface. After degassing, survey scans between 1100 and 0 eV were collected at a pass energy of 160 eV, 0.35 eV step size and a dwell time of 200 ms, and data were merged over three scans. Narrow scans of Ce, V, Cr, O and S were collected at 20 eV pass energy, 0.1 eV step size and 200 ms dwell time with 10-20 scans per sample. Spectra were referenced to C 1s binding energy of 283.26 eV, and were fitted using Gaussian-Lorentzian peak shapes and Shirley baselines.

Quantachrome Instruments Autosorb I was used for BET surface area determinations of freshly prepared reduced catalysts, using He gas.

5.3 Results

5.3.1 Characterization of anode materials

The XRD pattern of freshly prepared CSCV (PDF# 25-0307) showed the previously reported perovskite type structure for CSV, with a tetragonal unit cell and lattice parameters a = 5.52 Å and c = 7.81 Å (Figure 5.1 a) [1]. To form this structure Ce is present in the 3+ oxidation state, Cr as 3+, V as 3+ and Sr as 2+ under reducing conditions.

The BET surface areas of the prepared powders are summarized in Table 5.1. The high BET surface area of the NCY composite was due to the addition of nanoparticle YSZ. CSCV and the composite NCY each had good thermal expansion coefficient (TEC) matches with YSZ and so adhered well to the electrolyte. SEM images of prepared cross-sections of CSCV and NCY MEAs (Figures 5.2 and 5.3) showed that both anodes adhered well to the YSZ electrolyte after sintering. CSCV catalyst particles were well dispersed, well interconnected, and the structure had good porosity. The NCY anode had well distributed

phases YSZ, CSCV and Ni and a porous structure.

Table 5.1: Summary of BET surface areas of prepared catalysts.

Material	CSV	CSCV		NCY
Preparation	conventional	conventional	sol-gel	sol-gel
BET (m^2 g^{-1})	1.2	1.1	5.9	38.1

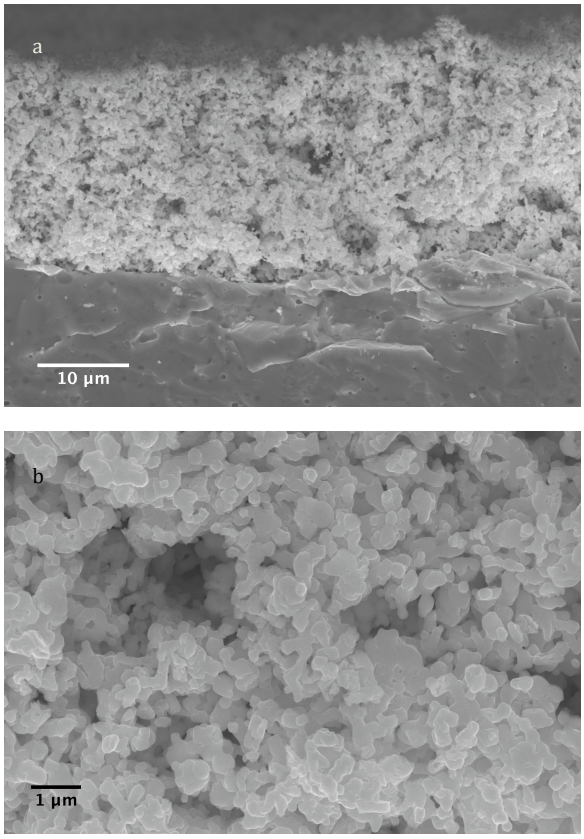

Figure 5.2: SEM image of: a) cross-section of CSCV MEA and b) high magnification of $Ce_{0.9}Sr_{0.1}Cr_{0.5}V_{0.5}O_3$ anode.

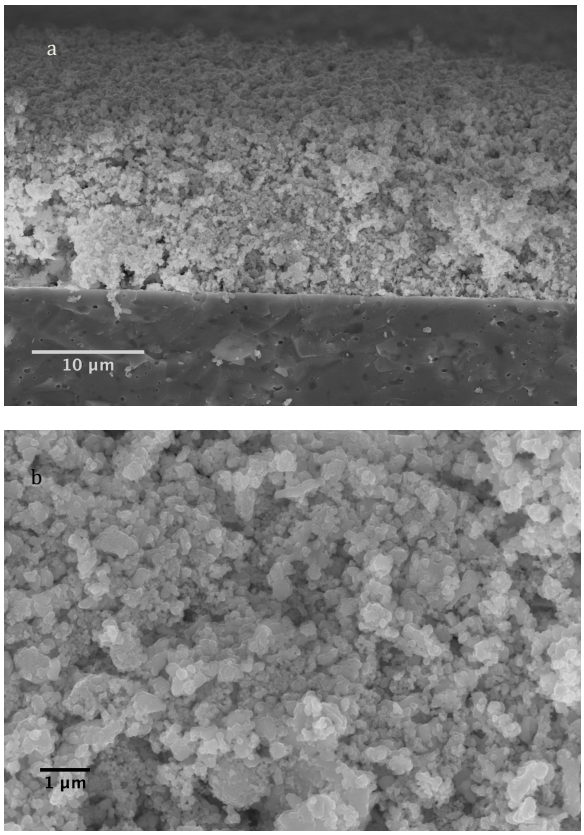

Figure 5.3: SEM image of: a) cross-section of NCY MEA and b) high magnification of Ni-CSCV-YSZ anode.

5.3.2 Thermal Analysis

The thermal stabilities of CSV and CSCV under oxidizing, inert and reducing environments were investigated using appropriate flowing gases in a DSC/TGA.

The TGA and DSC results for CSV are presented in Figures 5.4 and Figure 5.5, respectively. Figure 5.4 shows a 7% total weight gain when the CSV oxidized from $Ce_{0.9}Sr_{0.1}VO_3$ to $Ce_{0.9}Sr_{0.1}VO_4$. $Ce_{0.9}Sr_{0.1}VO_4$ has a zircon-type tetragonal unit cell, with lattice parameters a = 7.36 Å and c = 6.49 Å (PDF# 12-0757) [1]. For this structure Ce must be in the 3+ oxidation state, V predominantly as 5+ again, and substituent Sr is 2+. The oxidation reaction occurred in two stages with an initial small weight increase that started about 300 ^oC, followed by a second major weight gain that started at 400 ^oC and was complete at 500 ^oC. The weight gain is due to incorporation of additional O, the first peak possibly attributable to oxidation of V^{3+} to V^{4+} and the second to oxidation to V^{5+}. During reduction there was a 6% weight loss, when $Ce_{0.9}Sr_{0.1}VO_4$ was reduced to $Ce_{0.9}Sr_{0.1}VO_3$, showing that the redox process was fully reversible. Reduction occurred much less readily than the oxidation reaction, as it started at 800 ^oC and finished at 950 ^oC. When $Ce_{0.9}Sr_{0.1}VO_3$ was heated under N_2 there was no weight change, and so there was no change in composition; however there was a phase change close to 400 ^oC. The DSC curves under reduction and

oxidation conditions did not show any phase changes occurring independently of the oxidation and reduction reactions. Thus the reduction reaction may have been slower than oxidation as a consequence of the relative rates of the associated phase changes.

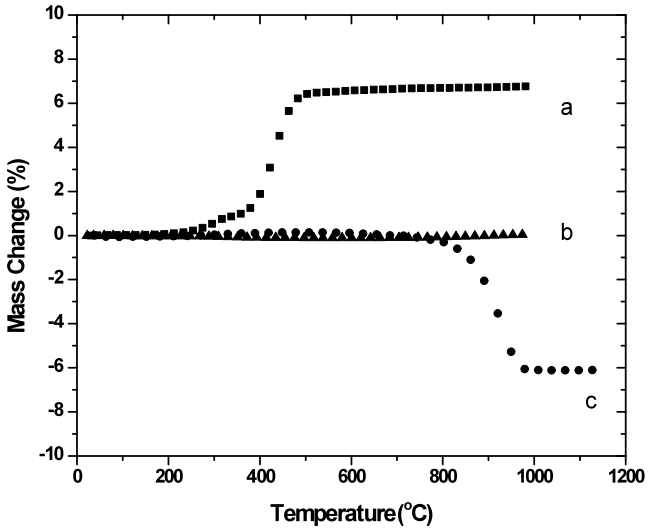

Figure 5.4: TGA curves for a) oxidation of $Ce_{0.9}Sr_{0.1}VO_3$ in air, b) $Ce_{0.9}Sr_{0.1}VO_3$ in N_2, and c) reduction of $Ce_{0.9}Sr_{0.1}VO_4$ in 1%H_2-N_2.

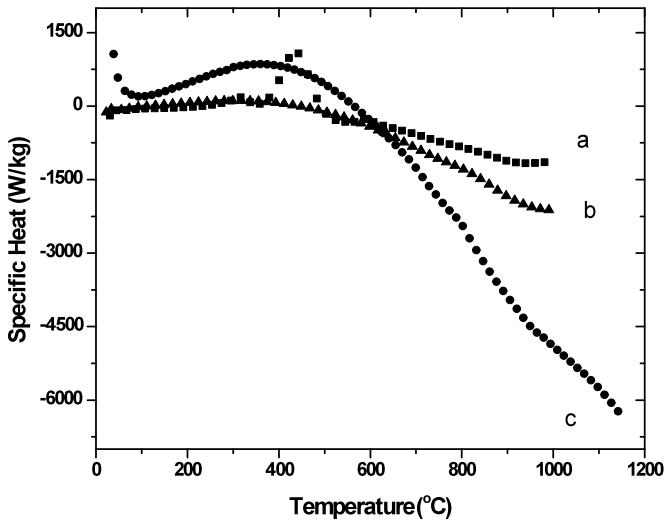

Figure 5.5: DSC curves for a) oxidation of $Ce_{0.9}Sr_{0.1}VO_3$ in air, b) $Ce_{0.9}Sr_{0.1}VO_3$ in N_2, and c) reduction of $Ce_{0.9}Sr_{0.1}VO_4$ in 1%H_2-N_2.

The TGA and DSC data for CSCV are presented in Figures 5.6 and 5.7, respectively.

CSCV gained 4% weight during oxidation, in a two-step process that started about 400 ^{o}C and was completed about 700 ^{o}C. The 4 wt% gain corresponded to an uptake of oxygen of only half ($Ce_{0.9}Sr_{0.1}Cr_{0.5}V_{0.5}O_{3.5}$) of what was required to fully oxidize the entire structure to $Ce_{0.9}Sr_{0.1}Cr_{0.5}V_{0.5}O_4$. Physically, this corresponded to oxidation of either half the V^{3+} to V^{5+} or all V^{3+} to V^{4+}, with a consequently greater oxygen coordination around the V cations. The process was reversible, as reduction of the oxidized CSCV also was 4 wt%, and occurred between 800-900 ^{o}C. No mass changes occurred under inert gas conditions, although there was a similar phase change at 400 ^{o}C, which was half as energetic as the one that occurred for CSV. Again, the DSC curves under reduction and oxidation conditions did not show any phase changes occurring independently of the oxidation and reduction reactions.

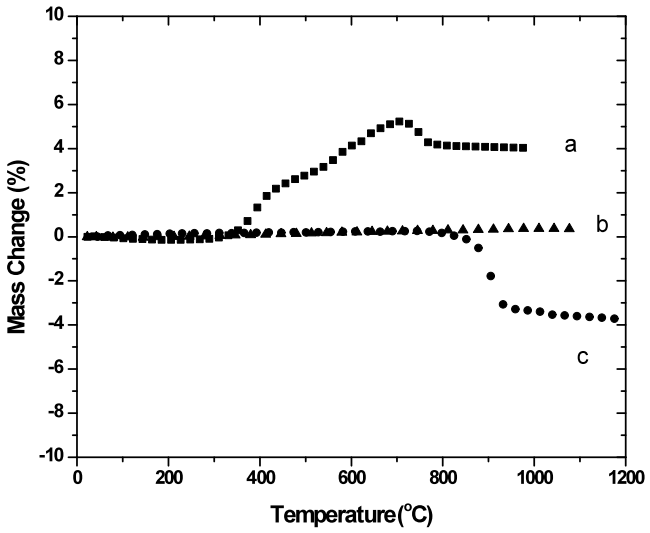

Figure 5.6: TGA curves for a) partial oxidation of $Ce_{0.9}Sr_{0.1}Cr_{0.5}V_{0.5}O_3$ in air, b) $Ce_{0.9}Sr_{0.1}Cr_{0.5}V_{0.5}O_3$ in N_2 and c) reduction of $Ce_{0.9}Sr_{0.1}Cr_{0.5}V_{0.5}O_{3+\delta}$ in 1%H_2-N_2.

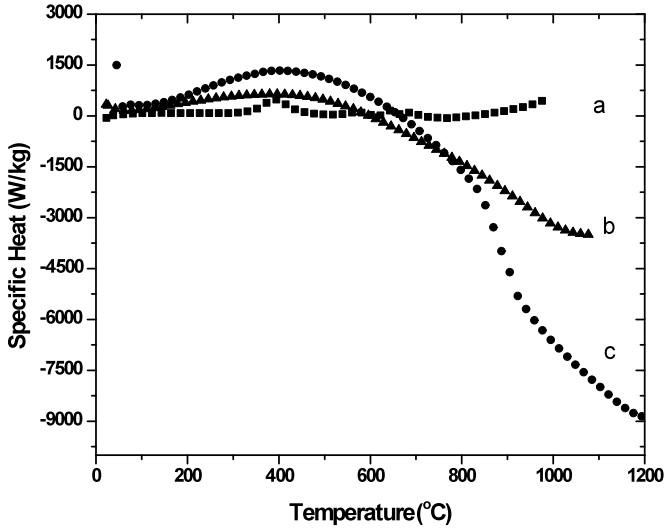

Figure 5.7: DSC curves for a) partial oxidation of $Ce_{0.9}Sr_{0.1}Cr_{0.5}V_{0.5}O_3$ in air, b) $Ce_{0.9}Sr_{0.1}Cr_{0.5}V_{0.5}O_3$ in N_2 and c) reduction of $Ce_{0.9}Sr_{0.1}Cr_{0.5}V_{0.5}O_{3+\delta}$ in 1%H_2-N_2.

Due to the ease of oxidation of CSCV composite anodes the anode feed gas was not humidified.

5.3.3 Electrochemical properties

Potentiodynamic tests were conducted to determine the electrochemical activity of the anode materials CSCV and NCY towards each of methane and H_2S. The MEAs were tested at 850 ^oC, in simulated sour gas comprising 0.5% H_2S-CH_4, 0.5% H_2S-N_2, 5% H_2S-N_2, and pure CH_4. Figure 5.8 shows the IV and IP curves for CSCV | YSZ | Pt, in 0.5% H_2S-CH_4. With this feed the cell produced maximum power density 85 mW cm^{-2}, while in 0.5% H_2S-N_2 it was slightly lower, 75 mW cm^{-2}. In either pure CH_4 or H_2 the cell did not produce any measurable level of power. This could be due to the low conductivity of the anode under non-H_2S atmospheres, however similar oxide materials discussed in §7 even with conductivities of similar magnitudes produced reasonable power densities in pure H_2 and CH_4, indicating the lack of catalytic activity of CSCV materials to hydrogen and methane electrooxidation. Reverting to a pure H_2 fuel after exposing the anode to H_2S fuel, caused it to revert back to an inactive oxide material.

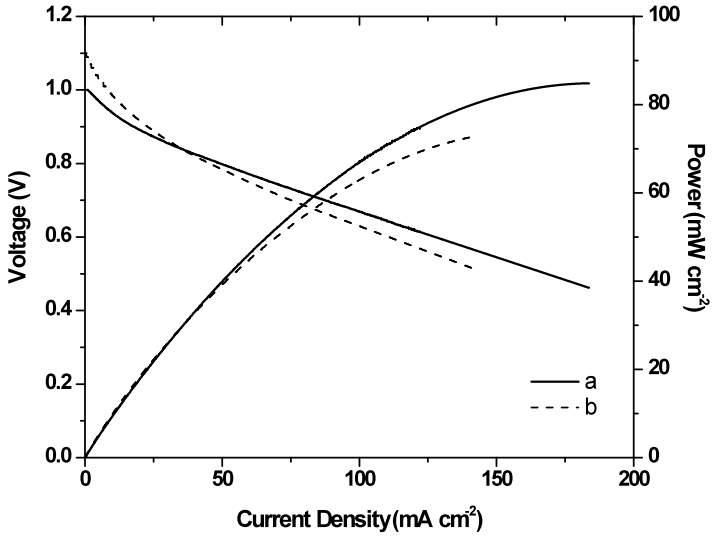

Figure 5.8: Potentiodynamic curves for sulfided $Ce_{0.9}Sr_{0.1}Cr_{0.5}V_{0.5}O_3$ | YSZ | Pt at 850 ^oC in (a) 0.5% H_2S-N_2 (b) 0.5%H_2S-CH_4.

In the methane containing fuel the open circuit voltage (OCV) was elevated to 1.1 V compared to about 1.0 V in N_2 containing H_2S, showing that CH_4 contributed to anode performance. Thus the difference in activity of the anode catalyst between feeds pure CH_4, 0.5% H_2S-CH_4 and 0.5% H_2S-N_2 did not arise from conversion of CH_4 over the unsulfided catalyst, but in the presence of H_2S the catalyst was partially sulfided, and this appeared to confer some capability to convert CH_4.

Figure 5.9 shows impedance curves for CSCV under the conditions above, and performance data are compared in Table 5.2. The fitting was done in using resistor-capacitor parallel circuits. The high frequency intercept, R_S, did not change significantly between the spectra when using different fuel feeds, and the value for R_{P1} (combined cathode and electrolyte resistance) was also similar in each case. In contrast, the value for R_{P2} (anode resistance) increased two-fold when using 0.5% H_2S-CH_4 and 0.5% H_2S-N_2.

Table 5.2: Summary of impedance data.

Resistivity	CSCV		NCY	
(Ω cm^2)	0.5% H_2S-N_2	0.5% H_2S-CH_4	CH_4	0.5% H_2S-CH_4
R_S	1.7	1.7	2.3	1.4
R_P1	3.1	3.8	9.3	4.7
R_P2	1.2	3.3	2.0	1.2

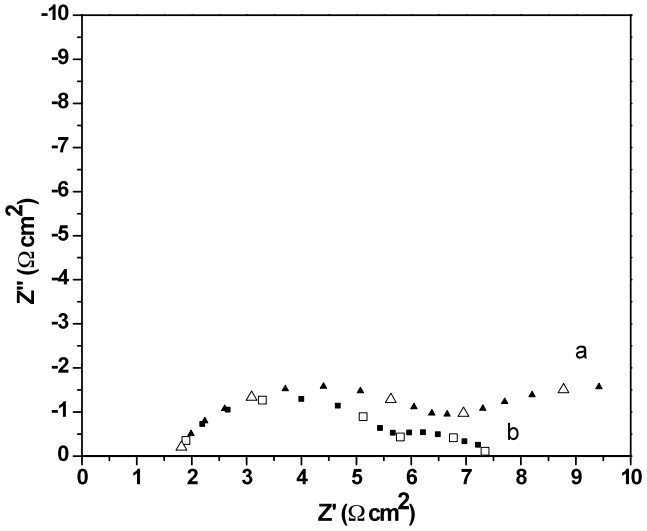

Figure 5.9: Impedance spectra for sulfided $Ce_{0.9}Sr_{0.1}Cr_{0.5}V_{0.5}O_3$ | YSZ | Pt ^oC at 850 ^oC in (a) 0.5% H_2S-N_2 (b) 0.5%H_2S-CH_4 (Frequency decades 1 x 10^5-1 x 10^{-1} are labelled with open symbols.)

The potentiodynamic curves for the MEA having the composite anode, NCY | YSZ | Pt, obtained using CH_4 and 0.5% H_2S-CH_4 feed gases are shown in Figure 5.10. The addition of Ni increased the activity of the anode for conversion of pure CH_4 and the maximum power density was 30 mW cm^{-2}. The power density using 0.5% H_2S-CH_4 as anode feed increased to 100 mW cm^{-2}. Impedance curves (Figure 5.11) showed that the presence of H_2S in the gas improved the ohmic resistance, and also decreased the secondary polarization process. The high frequency intercept, R_S, was affected when the fuel was changed from pure methane to 0.5% H_2S-CH_4, as the CSCV portion of the composite anode was activated, thus reducing the resistance. The change in value for R_{P1}, the first electrode polarization resistance which is ascribed to the cathode in the CSCV case, represented an anode process in the composite NCY because the cathode resistance did not change as a result of the change in anode gas. Hence there was a shift in mechanism of the reaction from only a H_2S electrochemical reaction to inclusion of a CH_4 reaction. When pure CH_4 was used as the fuel R_{P1} was 9 Ω cm^2, and the value of R_{P1} decreased when CH_4 and H_2S competed for adsorption sites. The second semicircle, representing the anode process, R_{P2}, decreased by about half when using 0.5% H_2S-CH_4 instead of pure CH_4, showing that the partially sulfided catalyst had lower resistance than the oxide form.

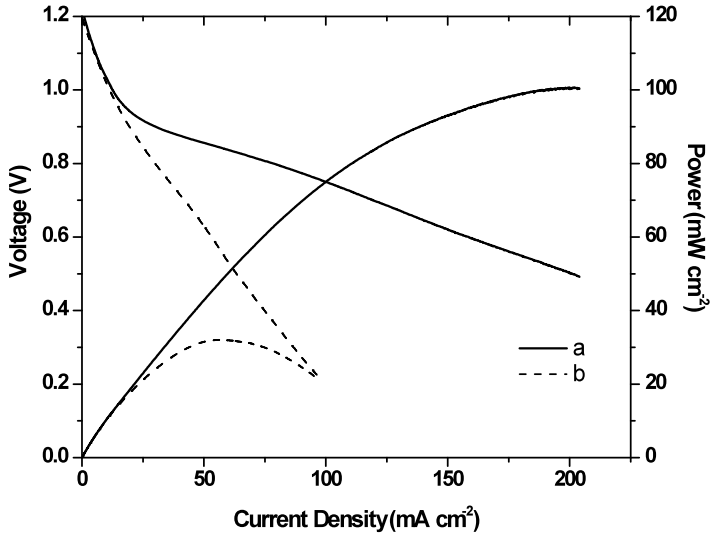

Figure 5.10: Potentiodynamic curves for Ni-$Ce_{0.9}Sr_{0.1}Cr_{0.5}V_{0.5}O_3$-YSZ | YSZ | Pt at 850 ^oC in (a) 0.5% H_2S-CH_4, (b) CH_4.

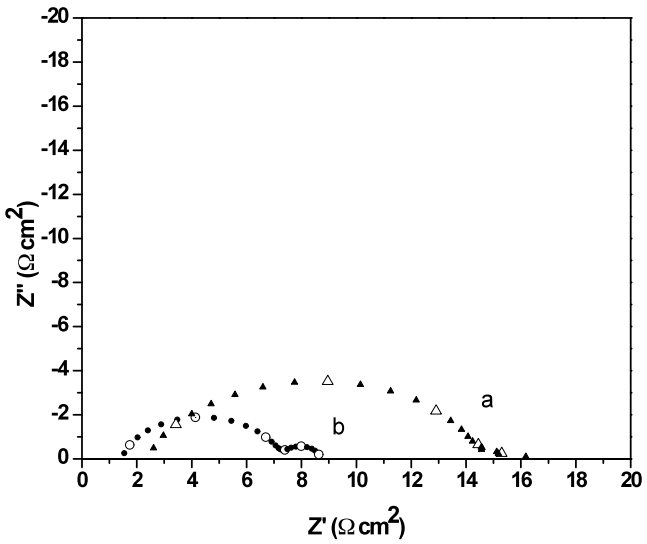

Figure 5.11: Impedance spectra for Ni-$Ce_{0.9}Sr_{0.1}Cr_{0.5}V_{0.5}O_3$-YSZ | YSZ | Pt ^oC at 850 ^oC in (a) CH_4, (b) 0.5%H_2S-CH_4. (Frequency decades 1 x 10^5-1 x 10^{-1} are labelled with open symbols.)

Figure 5.12 compares the sustainability over 15 h of galvanostatic performance of the catalysts CSCV and NCY, with fuel cell output 75 mA cm^{-2} and 40 mA cm^{-2}, respectively. The NCY anode was less stable than CSCV under galvanostatic conditions, as can be seen by

the slight increase in overpotential from -0.65 to -0.6 V. This was most likely a consequence of one of two processes: sintering of the Ni particles, and poisoning of Ni sites by H_2S. Both processes are known to occur in SOFC systems containing Ni [5-14].

Due to the complexity of the gas mixture used, including the corresponding reaction products, it was not possible to adequately determine the reaction products at the time of testing. Gas chromatography (GC) and mass spectrometry (MS) are the two most widely used methods for identifying gas phase molecules, at the time of testing GC was the only instrumentation available and identifying and quantifying all of the possible reaction products, at the quantities present was not possible.

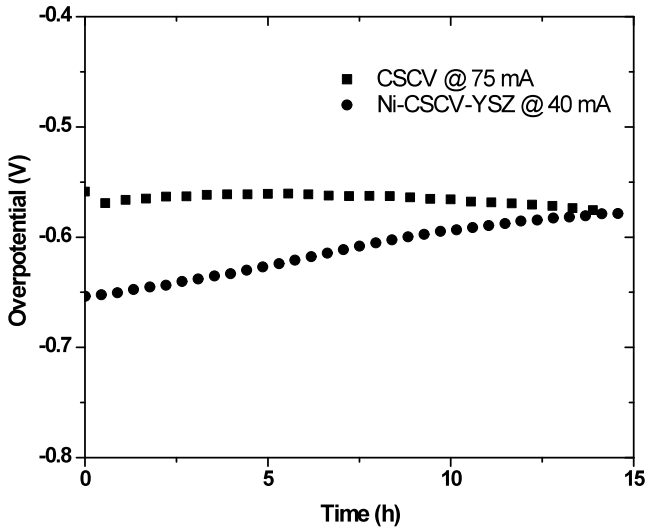

Figure 5.12: Long term galvanostatic test of sulfided $Ce_{0.9}Sr_{0.1}Cr_{0.5}V_{0.5}O_3$ | YSZ | Pt and Ni-$Ce_{0.9}Sr_{0.1}Cr_{0.5}V_{0.5}O_3$-YSZ | YSZ | Pt at 850 ^oC.

5.3.4 Total conductivity

The total conductivity of CSCV was determined under a range of conditions to determine the effects of atmosphere and temperature on its electrochemical properties. The conductivity of CSCV in H_2 increased with temperature, behaviour typical of semiconductors and ionic conductors (Figure 5.13 a). The activation energy was 0.1 eV. The conductivity of CSCV in H_2S containing gas (Figure 5.13 b) increased slightly with increasing temperature, behaviour which indicated occurrence of two competitive processes arising from the combination of Cr and V. Without Cr addition, pure CSV showed conductivity behaviour typical of metallic conductors [1]. In H_2S the conductivity increased two orders of magnitude from 0.64 to 4.34 S cm^{-1} (at 900 ^oC), in contrast to behaviour in the H_2 environment, and the activation energy was much lower, -0.03 eV, reflecting the metallic conductivity behavior.

XRD and XPS analyses were conducted on both fresh and used pellets to determine

whether the change in conductivity was associated with changes in the composition and/or structure of the material, which were not evident visually. The gold electrode paste was removed, and the pellet was ground to a fine powder. XRD analysis of the powder showed that the material had undergone a chemical reaction with H_2S, to form a material having a structure similar to that of fully sulfided $Ce_{0.9}Sr_{0.1}Cr_{0.5}V_{0.5}S_3$. However, the XRD pattern was not fully consistent with that of $Ce_{0.9}Sr_{0.1}Cr_{0.5}V_{0.5}S_3$, as seen by comparing the peak positions and intensities with those of the fully sulfided compound (PDF# 47-1039) (Figure 5.1 b), and supported by the XPS results below. These findings were consistent with partial substitution of O by S in the oxide, which results in a phase change of the structure from tetragonal perovskite to monoclinic perovskite, forming the product $Ce_{0.9}Sr_{0.1}Cr_{0.5}V_{0.5}(O,S)_3$ [1].

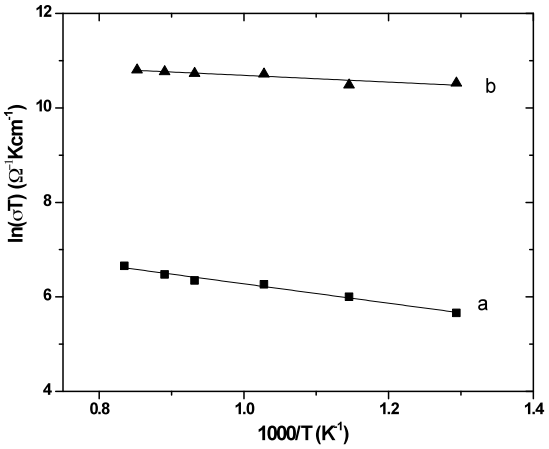

Figure 5.13: Conductivity of $Ce_{0.9}Sr_{0.1}Cr_{0.5}V_{0.5}O_3$ in (a) 10% H_2-N_2 and (b) sulfided catalyst in 5% H_2S-N_2.

5.3.5 H_2S stability

The CSCV and NCY anodes were also tested for H_2S reactivity at 850 ^oC. Both CSCV and NCY reacted with H_2S; the uptake of H_2S is shown in Figure 5.14 and 5.15.

The weight and heat flow change were monitored before and during the reaction and TGA and DSC signals are shown in Figures 5.14 a and 5.14 b, respectively. The signal was allowed to stabilize for 30 min upon reaching the reaction temperature, during which reduction of the sample was still occurring. There was an initial increase in weight and an exothermic heat flow. The weight gain was 0.07475 mg which, assuming that it was totally ascribable to adsorbed H_2S, constituted 2.5 x 10^{18} molecules (4.15 x 10^{-6} mol). Assuming that chemisorbed H_2S dissociated to form a monolayer of adsorbed S atoms, and that the catalyst particle geometry was approximately spherical, and the BET surface area, and the 8.2x10^{1}8 atoms Sads m^{-2} surface area [15], this constituted about 14% partial surface

coverage. The DSC signal also showed an exothermic peak followed by an increased heat capacity, which was indicative of adsorption and a change in the phase of the material. After 15 min the H_2S flow was stopped and pure H_2 allowed to flow, which was followed, starting essentially immediately, by a gradual return to the original weight as the adsorbed S was desorbed as it reacted with H_2 to reform H_2S. Trace amounts of SO_2 were also detected in the effluent (using a mass spectrometer coupled to the TGA), attributed to continuing reaction of sulfur with oxygen anions to form SO_2. Since the DSC/TGA instrument used horizontal beams to position the samples in the reactive gas flow, buoyancy effects were minimized. Blank trials using empty alumina cups did not show the same response as those shown in Figures 5.14 and 5.15, signifying that the reaction measured was dissociative adsorption of H_2S onto the catalyst sample.

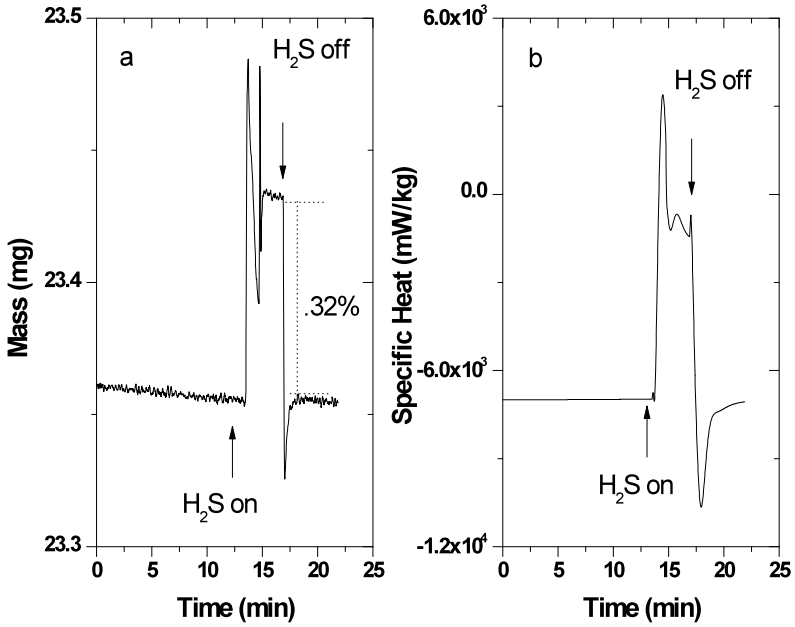

Figure 5.14: Effect of 500 ppm of H_2S on: a) TG, and b) DSC signal of $Ce_{0.9}Sr_{0.1}Cr_{0.5}V_{0.5}O_3$ at 850 ^oC.

The behaviour of the composite anode NCY differed from that of the pure component CSCV. The pure component material continuously adsorbed H_2S throughout the period of exposure, and when the supply of H_2S was terminated the adsorbed gas slowly desorbed from the material. During the 30 min of exposure to the gas, the weight of the material increased by 0.1047 mg, equivalent to 5.82 x 10^{-6} mol H_2S.

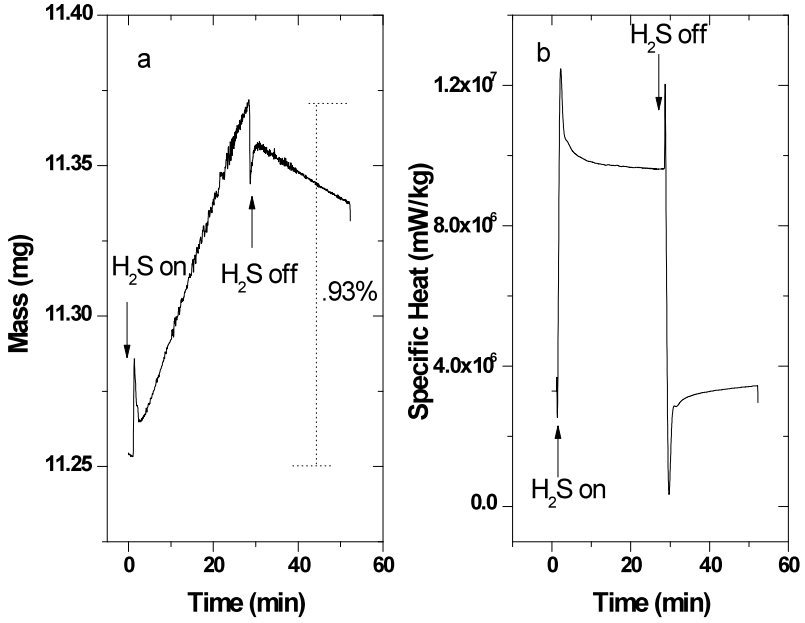

Figure 5.15: Effect of 500 ppm of H_2S on: a) TG, and b) DSC signal of Ni-$Ce_{0.9}Sr_{0.1}Cr_{0.5}V_{0.5}O_3$-YSZ at 850 ^oC.

5.3.6 XPS analyses

XPS was employed to determine the near-surface composition and near-surface ion electronic states of fresh CSCV, sulfided NCY, and sulfided $Ce_{0.9}Sr_{0.1}Cr_{0.5}V_{0.5}(O,S)_3$ which was formed after conductivity measurements in 5% H_2S containing atmosphere. Figure 5.16 shows high resolution sweeps of the main ionic components in the two materials. The compositions and peak locations are summarized in Table 5.3.

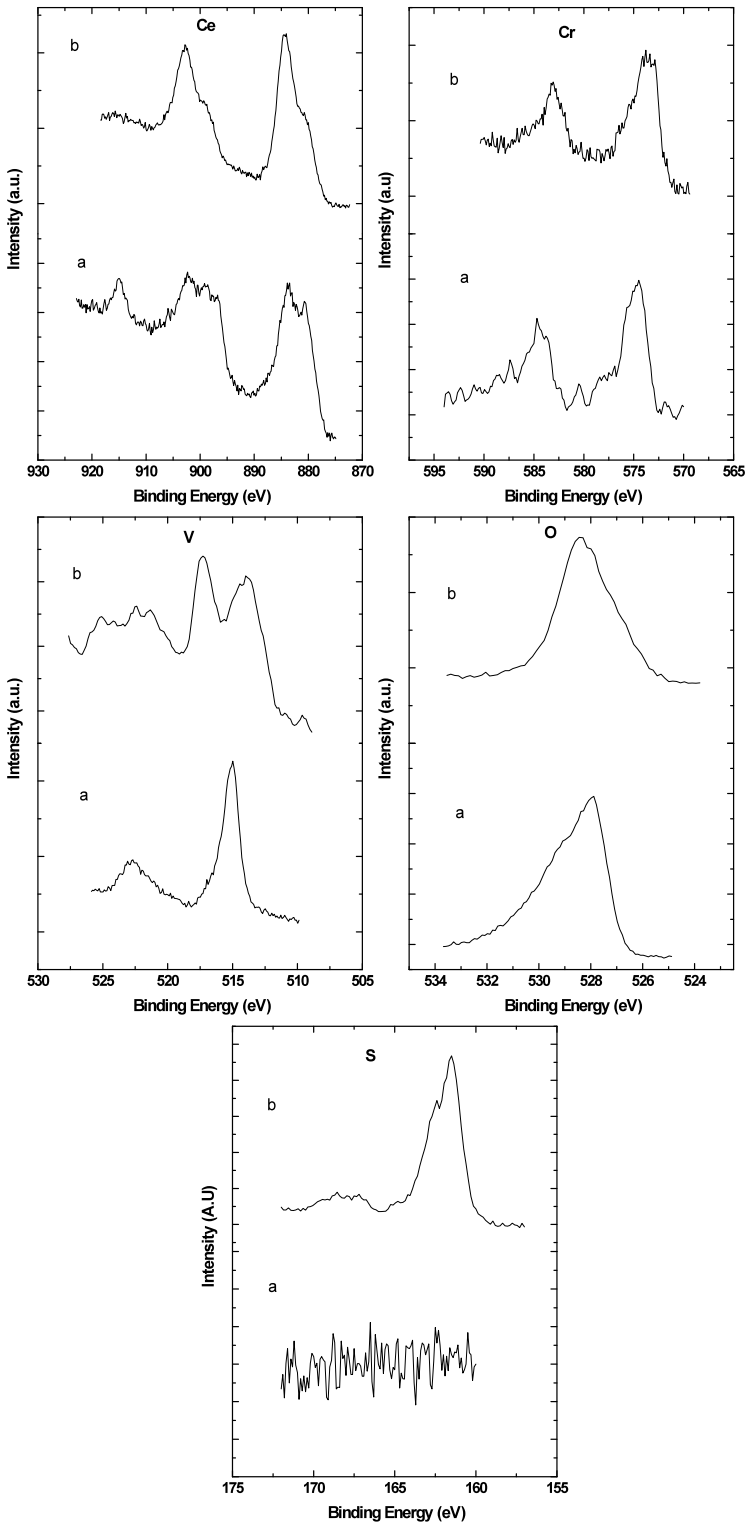

Figure 5.16: XPS spectra for different elements of (a) fresh and (b) sulfided $Ce_{0.9}Sr_{0.1}VO_3$.

Ce had five peaks attributed to $d^{5/2}$ and $d^{3/2}$ orbitals in the fresh sample while there were only four peaks in the spectrum of the sulfided material. The highest energy peak for

Ce, at 914.8 eV, was not present after sulfidation. The remaining four peaks all shifted to higher energies after sulfidation. The 880.5 and 883.8 eV peaks were shifted by about 0.5 eV, while the 897.2 eV and 901.5 eV peaks shifted by 1 eV to higher energies. The increase in binding energy may be related to an increase in oxidation state of a portion of Ce from Ce^{3+} to Ce^{4+} with sulfidation, since a more electropositive bond with S would decrease the binding energy. However, I will show below that the ratio of surface total anions/cations did not change by more than a small fraction, and so any partial change in oxidation state was small. It may be, therefore, that the change in peak position was attributable to a change in the anion bonded to the Ce cations.

The bond energy of the V peaks also shifted following sulfidation. A new peak formed at 512.3 eV, which was 3 eV lower than any V peak in the fresh CSCV sample. The $2p^{3/2}$ peaks at 515.1 and second peak 516.3 merged together to form one peak at 515.6 eV after sulfidation. A second peak was formed from the $2p^{1/2}$ peaks in the fresh sample at 521.4 eV and 522.9 eV that merged into one peak at 520.7 eV after sulfidation. The decrease in binding energy of all of the peaks is consistent with V-S bonding replacing V-O bonding. The appearance of the 512.3 eV peak may have resulted from formation of a new, lower valence V species, possibly V^{2+}.

Bond energy shifts of the Cr peaks were similar to those of V after sulfidation. Three peaks from the fresh sample at 574.6 eV, 584.2 eV and 587.2 eV each were shifted by about 1-1.5 eV to lower energies. One peak from the fresh sample at 577.2 eV was no longer present after sulfidation. The decrease in binding energy of all of the peaks signified formation of Cr-S bonding, similar to that for V.

Both O peaks shifted to higher binding energy by about 0.5 eV. The relative concentrations of the two peaks changed after sulfidation. Each binding energy representing a different bonding state for oxygen, as also occurred for sulphur as shown below, the first being a bridging O^{2-} between metal ions, the second being a terminal O^{2-} bonded to one metal ion.

There were four fitted peaks for sulfur on CSCV, which indicated bonding to each type of cation site. The spectrum for sulphur showed two pairs of overlapping peaks. The lower energy peak was attributed to a lattice sulphur, S^{2-}, while the higher energy peak was attributed to a bridging surface sulphur. These differed from the S adsorbed on NCY which showed only one peak centered at 167.2 eV (Figure 5.17). It seemed that the surface predominantly consisted of primarily Ni and S, instead of a mixture of O and S in the case of pure CSCV.

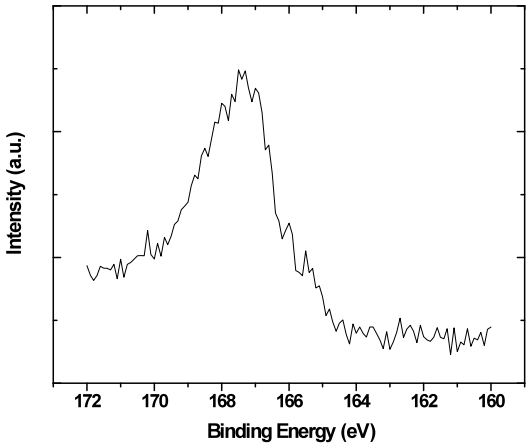

Figure 5.17: XPS spectra for S region of Ni-$Ce_{0.9}Sr_{0.1}Cr_{0.5}V_{0.5}O_3$-YSZ after exposure to H_2S.

Thus there was a change in the composition of the surface of the oxide which may have been, for example, from M-O-M(O)-O-M to either M-O-M(S)-O-M or M-S-M(O)-O-M, either of which would change the ratio of terminal surface O to bridging O, where M indicates a cation, -O- and S- indicate bridging anions, and (O) and (S) indicate terminal O and S.

The oxygen to metal cation ratio (O/cation) at the surface of fresh CSCV was 2.45, whereas the sulfided CSCV had an O/cation ratio of 1.71 and a sulfur to cation ratio (S/cation) of 0.74. Thus the formulation of the sulfided materials is best represented by the formula $Ce_{0.9}Sr_{0.1}Cr_{0.5}V_{0.5}(O,S)_3$, for which the ratio of O/S was 2.33 and the surface (O+S)/cation ratio was 2.44. Hence the ratio of total surface anions/cations was the same in each case.

Table 5.3: Summary of fitted XPS data.

					Ce				V				
CSCV	$3d^{5/2}$	$3d^{5/2}$	$3d^{3/2}$	$3d^{3/2}$	$3d^{3/2}$	$2p^{3/2}$	$2p^{3/2}$	$2p^{1/2}$	$2p^{1/2}$	$2p^{3/2}$	$2p^{3/2}$	$2p^{1/2}$	$2p^{1/2}$
Area	3567.9	5164.2	3007.6	3678.9	1084.0	1565.1	205.6	348.0	340.1	342.2	105.2	146.8	260.7
FWHM	3.3	4.2	3.8	5.2	2.7	1.5	1.3	2.8	1.8	2.2	3.2	2.0	7.0
Position (eV)	880.1	883.7	897.2	901.5	914.8	515.1	516.6	521.4	522.8	574.6	577.2	584.2	587.2
Concentration	21.5	31.2	18.3	22.4	6.5	63.7	8.4	14.2	13.8	40.1	12.3	17.2	30.5
	O												
	1s	1s											
Area	2812.8	5493.4											
FWHM	1.2	2.8											
Position (eV)	527.9	529.2											
Concentration	33.9	66.1											
CSCV-S													
Area	4072.7	7092.8	2240.9	5630.2		630.5	300.4	243.7		495.9	547.9	405.6	115.9
FWHM	3.7	3.4	3.5	4.2		2.9	1.5	3.7		1.8	3.0	2.2	2.4
Position (eV)	880.5	884.3	898.5	902.7		513.9	515.6	522.3		573.2	574.8	583.9	585.6
Concentration	21.3	37.2	11.8	29.7		53.7	25.6	20.7		31.7	35.0	7.4	25.9
	O		S										
	1s	1s	2p	2p	2p	2p							
Area	670.2	4116.7	667.9	1276.4	148.7	288.6							
FWHM	1.5	2.1	1.1	2.7	0.9	2.9							
Position (eV)	528.3	530.0	159.8	160.5	161.0	166.5							
Concentration	14.0	86.0	28.1	53.6	6.2	12.1							

5.4 Discussion

$CeVO_3$ with $CeCrO_3$ provided a substituted perovskite with better redox stability the pure oxide $CeVO_3$, as shown by DSC/TGA. The perovskite parent lattice had the capability of accommodating both Cr and V cations at B sites, due to their similar sizes. The Cr^{3+} ion is much more stable, as shown by Cr_2O_3 stability over a wide oxygen partial pressure range, and it appeared to stabilize the structure and stabilize V^{3+} at higher oxygen partial pressure conditions, as shown by the increased temperature required for oxidation and the lower weight increase during oxidation. The substitution of Cr at B-sites also almost doubled the total conductivity of the material compared to pure CSV in H_2 containing gas, from 0.33 S cm^{-1} to 0.57 S cm^{-1} at 850 ^oC [1]. Sr- or Ca- substituted $LaCrO_3$ is known to be a good electronic conductor, and it is used as a current collector material in SOFCs [16]. In CSCV, the incorporation of Cr and the $Cr^{3+/4+}$ couple formed as a result of doping the structure with Sr imparts higher electronic conductivity compared to that of the V oxide, CSV.

In H_2S-containing gas the conductivity of CSCV dramatically increased, from 0.57 S cm^{-1} to 42.27 S cm^{-1} at 850 ^oC. This dramatic increase accompanied a phase change in the material, which XRD spectra showed to be formation of a partly sulfided phase of similar structure to tetragonal $Ce_{0.9}Sr_{0.1}Cr_{0.5}V_{0.5}S_3$. Texturing in the XRD spectra as well as the XPS results showing an O/S atomic ratio of 2.4 which led to the conclusion that the material was an oxysulfide which had partial occupation of S^{2-} in O^{2-} sites in the tetragonal oxide perovskite. The ratio of total surface anions/cations was the same in each case; and thus there was no oxidation. The change in structure accompanying partial sulfidation was similar to that found previously for $Ce_{0.9}Sr_{0.1}VO_3$ [1]. The continuing presence of O^{2-} in the structure enabled the fuel cell activity as the anode material must be electronically and ionically conductive, no additional oxide ion conductor was added to the anode.

Potentiodynamic tests for CSCV showed that the anode was essentially inactive towards pure CH_4 and H_2. Upon heating the fuel cell to the reaction temperature in H_2 environment the ohmic resistance of the cell was high, typically about 10 Ω cm^2 or greater. With the introduction of H_2S as a component of the fuel, the resistance dropped and the altered catalyst, $Ce_{0.9}Sr_{0.1}Cr_{0.5}V_{0.5}(O,S)_3$, was highly active towards H_2S, although still not highly active to H_2 and CH_4. This is clearly seen in Figure 5.8, where the fuel cell produced similar amounts of power with H_2S balanced with either CH_4 or N_2. If the anode catalyst was significantly active for conversion of CH_4, the activity would show a pronounced increase in performance in the presence of a high concentration of CH_4. This interpretation was supported by the impedance spectra shown in Figure 5.9. The polarization resistance, as characterized by the second semicircle (the first semicircle is ascribed to the reaction at the Pt cathode), was higher in either N_2 or CH_4 alone. The anode was active for H_2S electro-oxidation in feeds containing either diluent, but the H_2S electro-oxidation reaction was impeded by either competitive adsorption (in the case of methane) or gas diffusion.

The evidence for competitive adsorption of methane was that the OCV was higher when methane was used, consistent with have adsorption onto the surface under OCV conditions.

Substitution of transition metal cation Cr^{3+}, into the perovskite catalyst B-site of $Ce_{0.9}Sr_{0.1}VO_3$ resulted in an improvement in performance in 0.5% H_2S-N_2 in comparison to unsubstituted $Ce_{0.9}Sr_{0.1}VO_3$ [1]. The potentially active sites for H_2S oxidation were Ce, V and Cr cations. The mechanism was different from that for low temperature oxidation of H_2S over $CeVO_4$, where only $Ce^{3+/4+}$ was found to participate in the reaction [17], and similar to electrochemical activity of $Ce_{0.9}Sr_{0.1}VO_3$ where both Ce and V were found to participate in the H_2S electro-oxidation reaction[1]. The evidence for participating cations in the reaction was found in the XPS data for sulfided CSCV: changes in bonding energies of the cations indicated their participation in the reaction mechanism. There was a peak associated with Ce^{4+} in the fresh oxide which disappeared after sulfidation, attributed to complete reduction of the Ce^{4+} cations during formation of the sulfided material. All the V and Cr peaks underwent shifts after sulfidation, and their binding energies were changed by at least 0.5 eV. In addition, two high energy peaks for each of Cr and V merged to form one peak.

The conductivity change resulting from the conversion of the oxide to sulfide was consistent with the high ohmic resistance of the material in non-H_2S-containing gases. The stability of CSCV towards carbon deposition and sulfur poisoning, as opposed to activation as a result of sulfidation, was confirmed by the long-term electrochemical tests in which performance did not degrade.

Ni and YSZ were added to CSCV to form a composite catalyst with the intent to improving methane oxidation kinetics of the anode. It was hypothesized that the presence of highly active oxide/sulfide around the Ni would prevent it from sulfiding in the sour gas, whereas, typically, 5 ppm of H_2S would poison Ni-YSZ anodes [5]. It was also recognized that the high H_2S concentration could enable favourable NiS formation [18-20]. The potentiodynamic and impedance data in Figures 5.10 and 5.11 showed that the composite catalyst was active for methane conversion. Overall the composite produced 18% more power in sour gas, which was due to a combination of lower ohmic resistance and lower electrode polarization and gas diffusion impedance. A 15 h galvanostatic stability test at 40 mA cm^{-2} showed slight degradation of the potential from -0.66 to -0.60V. This may have been a consequence of any one or combination of carbon deposition on the Ni particles, sulfur poisoning of the Ni, and agglomeration of Ni particles. Both DSC/TGA data and XPS data showed evidence of sulfidation of the anode. Under DSC/TGA conditions which simulated the atmosphere of the fuel cell, but without the potential gradient, the anode adsorbed S continuously over 30 min. This differed from the uptake of H_2S on the CSCV anode alone for which the increase in weight ceased after adsorbing about 0.3%w/w. The S XPS spectra for NCY differed from those for CSCV, in that there was evidence of primarily Ni-S bonds meaning that, even though H_2S active CSCV sites were near the Ni sites, the

H_2S still preferentially adsorbed onto Ni under fuel cell conditions.

5.5 Conclusions

- Cr^{+3} addition into $Ce_{0.9}Sr_{0.1}VO_3$ to form $Ce_{0.9}Sr_{0.1}Cr_{0.5}V_{0.5}O_3$ led to improved redox stability, and improved conductivity in reducing environments.
- $Ce_{0.9}Sr_{0.1}Cr_{0.5}V_{0.5}O_3$ had improved electrocatalytic activity towards H_2S oxidation compared to $Ce_{0.9}Sr_{0.1}VO_3$; however Cr addition did not improve methane conversion activity.
- $Ce_{0.9}Sr_{0.1}Cr_{0.5}V_{0.5}O_3$ underwent a solid-gas reaction with H_2S in which the materials reacted to form $Ce_{0.9}Sr_{0.1}Cr_{0.5}V_{0.5}(O,S)_3$. The oxide retained in the MEA allowed continuing O^{2-} conduction.
- Admixing of NiO with $Ce_{0.9}Sr_{0.1}Cr_{0.5}V_{0.5}O_3$ increased methane oxidation activity.
- Ni-YSZ-$Ce_{0.9}Sr_{0.1}Cr_{0.5}V_{0.5}O_3$and $Ce_{0.9}Sr_{0.1}Cr_{0.5}V_{0.5}O_3$ showed stable performance for 15 h under polarization conditions using H_2S-CH_4 as fuel. However, XPS results show that the long-term stability of the Ni cermet is questionable.

5.6 References

[1] N. Danilovic, J.L. Luo, K.T. Chuang, A.R. Sanger, J. Power Sources, in press (2009).

[2] T. Kawada, H. Yokokawa. In J. Nowotny, C.C. Sorrell ed., Key Engineering Materials, 125-126 (1996) 205.

[3] I. Takahara, W. C. Chang, N. Mimura, M. Saito, Catal. Today, 45 (1998) 55-59.

[4] J.B. Goodenough, Y.H. Huang, J. Power Sources, 173 (2007) 1-10.

[5] J.N. Kuhn, N. Lakshminarayanan, U.S. Ozkan, J. Mol. Catal A, 282 (2008) 9-21.

[6] Z. Cheng, M. Liu, Solid State Ionics, 178 (2007) 925-935.

[7] S. Zha, Z. Cheng, M. Liu, J. Electrochem. Soc., 154 (2007) B201-B206.

[8] H.P. He, A. Wood, D. Steedman, M. Tilleman, Solid State Ionics, 179 (2008) 1478-1482.

[9] K. Haga, S. Adachi, Y. Shiratori, K. Itoh, K. Sasaki, Solid State Ionics, 179 (2008) 1427-1431.

[10] Z. Cheng, M. Liu, Solid State Ionics, 178 (2007) 925-935.

[11] M. Gong, X. Liu, J. Trembly, C. Johnson, J. Power Sources, 168 (2007) 289298.

[12] X.J. Chen, Q.L. Liu, S.H. Chan, N.P. Brandon, K.A. Khor, J. Electrochem. Soc., 154 (2007) B1206- B1211.

[13] Z.R. Xu, J.L. Luo, K.T. Chuang, A.R. Sanger, J. Phys. Chem. C, 111 (2007) 16679-16685.

[14] S.P. Jiang, J. Mat. Sci., 38 (2003) 3775-3782.

[15] C.H. Bartholomew, Mechanisms of Nickel Catalyst Poisoning, in Catalyst Deactivation, B. Delmon and G.F. Froment, Editors. 1987, Elsevier. 81-104.
[16] W.Z. Zhu, S.C. Deevi, Mat. Sci. Eng. A, 362 (2003) 228-239.
[17] S. Yasyerli, G. Dogu, T. Dogu, Catal. Today, 117 (2006) 271-278.
[18] C.M. Grgicak, R.G. Green, J.B. Giorgi., J. Power Sources, 179 (2008) 317-328.
[19] C.M. Grgicak, J.B. Giorgi, J. Phys. Chem. C, 111 (2007) 15446-15455.
[20] C.M. Grgicak, M. M. Pakulska, J.S. OBrien, J. B. Giorgi, J. Power Sources, 183 (2008) 26-33.

Chapter 6

Carbon deposition on vanadium based solid oxide fuel cell anodes

6.0.1 Introduction

With the findings in § 4 and § 5 on the CSV/CSCV systems, where it was determined that those systems were inactive towards CH_4 but active towards H_2S, a novel application of those materials would be in fuel cell that upgraded sour methane containing mixtures by electrochemically oxidizing the H_2S. If the product is S_2, it can be condensed out of the mixture and the H_2S-free CH_4 can proceed to a second fuel preconditioning stage such as a reformer or to a fuel cell that can directly oxidize methane. To have practical application the anode material would have to be resistant to carbon deposition. In this chapter I report and discuss the carbon deposition on several oxide anode compositions that have showed promising H_2S activity. Previously, VOx-$LaCrO_3$-YSZ (VLY) composite anodes were shown to be stable in syngas, a mixture of 59.5% H_2 - 40% CO - 0.5% H_2S, and fuel cells using them achieved power densities up to 260 mW cm^{-2} at 1173 K [1]. Further $Ce_{0.9}Sr_{0.1}Cr_{0.5}V_{0.5}O_3$ (CSCV) mixed metal oxides also are stable in sour natural gas, modeled using CH_4 - 0.5% H_2S, and show enhanced performance compared to $Ce_{0.9}Sr_{0.1}VO_3$, up to 120 mW cm^{-2} at 1123 K [2, 3]. Although the two oxide materials do not exhibit superior electrocatalytic activity towards methane oxidation, and as such are not expected to catalyze carbon deposition, I will show that they can be used to electrochemically oxidize H_2S in a methane stream, via reactions 3.17 and 3.18.

For a fuel cell natural gas upgrader to function properly the catalysts used should be inactive to methane, and carbon deposition should be minimal. I will compare the propensities of CSCV and VLY for carbon deposition, to evaluate their propensity for carbon deposition, and their suitability for H_2S removal from a hydrocarbon stream. I will show that, when using pure methane as feed under no circuit conditions (Type I), open circuit (Type II) and polarization (Type III) for 6 h at 1073 K, each catalyst showed a propensity for carbon deposition under all conditions. The amounts of carbon deposited on the oxide anodes were significantly smaller than those deposited on similarly prepared

Ni-YSZ anode materials. Gold current collectors had an effect in increasing the amount of deposited carbon. Overall, even though the oxide anodes are unsuitable for methane oxidation in the fuel cell, they can remove H_2S from a flowing stream of CH_4 without significant carbon deposition.

6.1 Experimental

6.1.1 Catalyst preparation

CSCV preparation is as described previously in § 5.

VLY was prepared by mixing a mixture of reduced V_2O_5 (Aldrich, 99.9%), $LaCrO_3$ (Alfa Aesar, 99.5%) and 8 mol% YSZ nano-powder (Inframat Advanced Materials) in 40:40:20 weight ratio in iso-propanol in an ultrasonic bath for 1 h. The dry initmately mixed composite anode catalyst VLY remained after natural evaporation of iso-propanol at room temperature. Ni-YSZ was prepared by ball milling a 50-50 wt% mixture of NiO (Alfa Aesar, 99%) and YSZ (Tosoh) for 24 h.

6.1.2 Membrane assembly

The anode powders were finely ground, then dispersed in α-terpineol (Advanced Materials) to form a paste. A 1 cm^2 anode was applied by screen printing the paste onto one face of the membrane used to prepare the membrane electrode assemblies (MEA). MEAs used for Type I coking condition tests did not have a cathode, while membranes for Type II and Type III testing conditions had cathodes prepared by painting platinum paste (Heraeus, 1 cm^2 circular area) onto the opposite face of the YSZ electrolyte membrane (8 mol% Y_2O_3, Intertec Southwest, 25.4 mm OD, 0.3 mm thick) and sintering in-situ at 1273 K. The MEAs having CSCV and VLY anodes were sintered in 10% H_2-Ar for 2 h at 1273 K. NiO-YSZ membranes were fired in air at 1473 K for 2 h and then reduced in situ in 10% H_2-N_2 for 1 h before feeding methane to the anode compartment. Typical anode thicknesses were about 50 μm, while the cathode thickness was 5-10 μm.

6.1.3 Carbon deposition

MEAs were installed in a fuel cell testing apparatus shown schematically in Figure 6.1. Coking tests were conducted at 800 K for 6 h. The MEAs were situated between coaxial mullite tubes (25.4 mm OD and 12.7 mm OD, McDanel Advanced Ceramic Technologies) used for anode and cathode feeds and removal of effluent gases. Connectors were constructed from Swagelok Ultra-Torr fittings. Gold current collector wires with spiral wound ends were run through the length of the inlet tube and installed on MEAs used with Type II and Type III conditions. The pure CH_4 fuel flow rate was 50 mL min^{-1}, while the air flow rate was 200 mL min^{-1}. The chamber volume was close to 80 mL resulting in a LHSV of 150 h^{-1}. Ceramic sealant (Aremco, Type 503) was applied to one end the outlet anode tube, and the

exterior portion of a MEA was secured using the sealant. The sealant was then cured using the procedure prescribed by Aremco, and the cell was heated to 1073 K at 2 K min^{-1} in flowing 10% H_2 - N_2 gas.

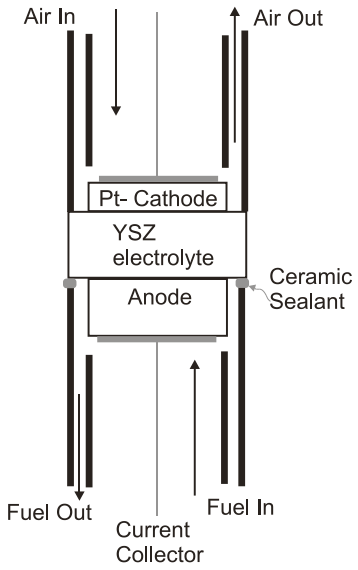

Figure 6.1: Experimental fuel cell setup.

6.1.4 Fuel cell evaluation

Fuel cell testing was conducted using standard DC and AC electrochemical techniques using a Solartron 1287A Potentiostat/Galvanostat. A MEA that was tested under Type II or III conditions was first evaluated using impedance spectroscopy to determine if the cells had adequate contact with the current collectors. The cell ohmic resistance was between 0.5 Ω cm^{-2} and 1 Ω cm^{-2}. An additional requirement was that the initial open circuit voltage (OCV) was within 10% of the theoretical OCV for the H_2-anode | YSZ| cathode-air cell.

6.1.5 Carbon deposition characterization

An Autochem II 2920 system was used for temperature programmed oxidation (TPO) of coked anode materials in a 10% O_2 - He mixture (50 mL min^{-1}) up to 1223 K, with a 10 K min^{-1} heating rate. The sample was held in a quartz U-tube with quartz wool packed in one arm, onto which the sample was placed, as shown in Figure 6.2. The amounts of evolved gases were measured using a thermal conductivity detector (TCD). The expressed amount of catalyst is the mass of nickel and/or oxide catalysts (YSZ excluded).

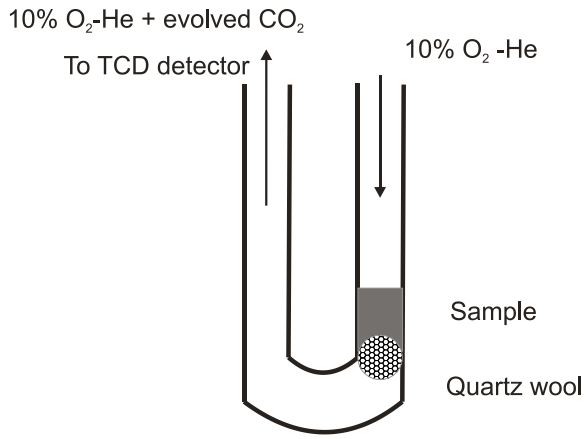

Figure 6.2: TPO experimental apparatus.

A mass spectrometer (Pfeiffer Thermostar GSD 301) was used to analyze the effluent from TPO of coked ceramic oxide anodes, both to confirm the product distribution for use with the TCD and to quantify the amount of carbon deposited when its concentration was below the detection limit for the TCD.

6.1.6 Materials characterization

A Rigaku RU200 powder X-ray diffraction (XRD) system with a rotating anode and a Co target was used for analysis of all synthesized powders. The commercially available software Jade was used to establish identities of all phases detected in the samples. A JEOL 6301F field emission scanning electron microscope (SEM) was used for characterizing structures of MEAs.

6.2 Results

6.2.1 Materials characterization

The XRD spectra of prepared powder materials are shown in Figure 6.3. CSCV had overlapping peaks that correspond to both $CeVO_3$ and $CeCrO_3$. There were no detectable peaks arising from impurity phases. The spectrum for VLY showed only peaks for VOx, YSZ and $LaCrO_3$, and so VLY was a composite anode without any significant amount of new phases.

SEM micrographs of as prepared and coked MEAs are shown in Figure 6.4. The anode structures of VLY (Figure 6.4 a), CSCV (Figure 6.4 c) and Ni-YSZ (Figure 6.4 e) are porous and well networked. There is no carbon apparent on VLY (Figure 6.4 b) and CSCV (Figure 6.4 d). In Figure 6.4 f carbon fibres (whiskers) can be seen growing in large numbers out of nickel particles in the Ni-YSZ structure. The cracking of the Ni-YSZ structure is a result of growth of the carbon whiskers.

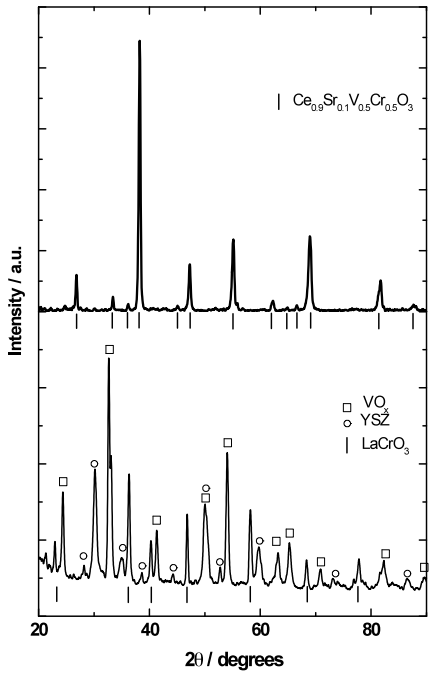

Figure 6.3: XRD patterns for a) CSCV and b) VLY.

6.2.2 Type I carbon deposition: catalysts coked under no current conditions

Anodes were coked in flowing dry methane in the fuel cell setup in which no cathode or current collector was present, and so there was no external circuit providing electrical contact between the anode and cathode sides. These conditions meant that there was only catalytic methane cracking on the catalyst surface, as in reaction 3.8. The TPO data are shown in Figures 6.5 a, 6.6 a and 6.7 a for VLY, CSCV and Ni-YSZ respectively. Type I coking was done in an otherwise similar experimental set up as for Types II and III conditions to minimize any differences that might arise due to changes in oxygen partial pressure and fuel conversion.

The TPO spectrum of carbon deposited on the oxide anode catalyst VLY (Figure 6.5 a) generated one CO_2 peak close to 625 K.

Oxidation of carbon deposited on the CSCV anode showed no evolution of carbon (Figure 6.5a).

For each of these oxide anode catalysts the amount of carbon deposition was determined using mass spectrometry, as the TCD method was unable to accurately determine low levels of deposited carbon by quantifying the evolution of very small amounts of CO_2. No carbon can be seen using SEM, and so that this was not a good method of evaluating carbon deposition on these oxide materials. TPO of carbon on the oxide anodes gave rise to considerably smaller CO_2 peaks when compared to the sample containing nickel.

The TPO spectrum of carbon deposited on the Ni-YSZ (Figure 6.7 a) showed one CO_2

peak at 860 K. The total amount of carbon evolved from the Ni-YSZ anode was three orders of magnitude greater than from the VLY oxide anode and the temperature of CO_2 evolution was greater by 200 K [5]. The SEM micrograph (Figure 6.4 f) of the Ni-YSZ anode cross-section after coking also shows significant evidence of carbon deposition and growth of carbon fibers.

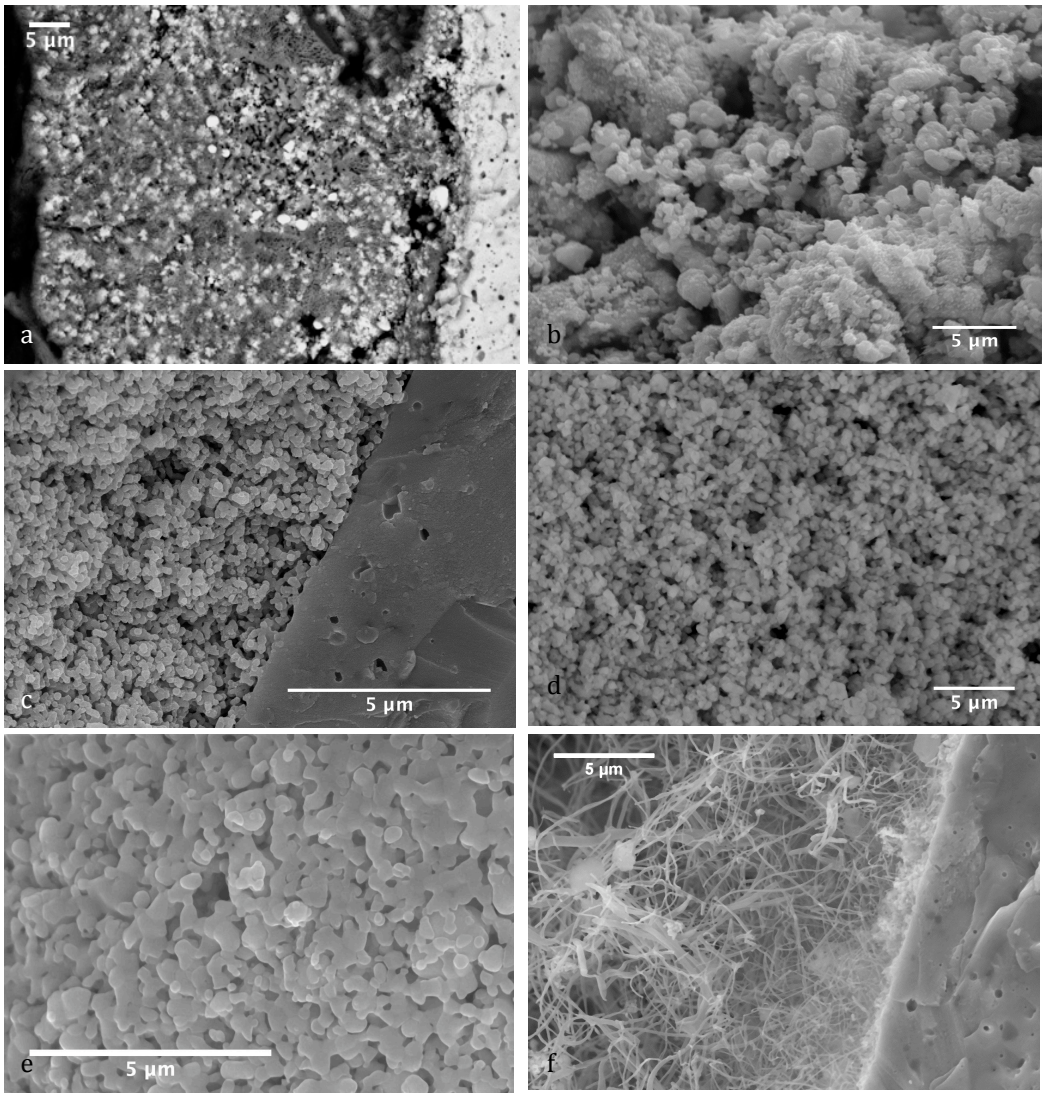

Figure 6.4: SEM images of cross-sections of a) VLY -as prepared b) VLY -coked c) CSCV -as prepared d) CSCV -coked e) Ni-YSZ -as prepared f) Ni-YSZ -coked.

6.2.3 Type II carbon deposition: catalysts coked under OCV conditions, with current collector attached to the anode

TPO results for anodes coked in the fuel cell setup under open circuit conditions in flowing methane are shown in Figures 6.5 b, 6.6 b and 6.7 b for VLY, CSCV and Ni-YSZ, respectively. The open circuit voltages as a function of time are shown in Figure 6.8 for all three

anodes. The theoretical OCV in methane at 1073 K is 1.04 V; the OCV values in the inactive oxides were lower between 0.9 and 1.0 V whereas the Ni-YSZ OCV was higher, about 1.2 V, due to reforming of methane on the surface and the establishment of OCV relative to H_2 [6].

However, under Type II conditions (OCV) VLY showed an order of magnitude increase in deposited carbon, and that carbon was oxidized at similar temperatures, 650 K and 697 K, as that formed under Type I conditions. Similarly, CSCV also had a higher amount of deposited carbon under Type II conditions, while the temperatures of CO_2 evolution during TPO were 750 K and 840 K, similar temperatures to those for CO_2 evolution from VLY.

The nickel containing catalysts had two orders of magnitude more carbon deposited than the oxide catalysts under open circuit conditions. The major difference between the types of carbon deposit was shown by the temperature of CO_2 desorption during TPO: the nickel containing catalyst had CO_2 evolution temperatures above 850 K, showing that the carbon which had formed on the surface was very hard to remove from the surface.

Overall, the amount of deposited carbon on all three anodes was greater under Type II than Type I conditions.

6.2.4 Type III carbon deposition: catalysts coked under polarization conditions

Type III conditions are more representative of those in an operating fuel cell, as the electrodes are polarized. TPO results for catalysts coked under Type III conditions are shown in Figures 6.5 c, 6.6 c and 6.7 c for VLY, CSCV and Ni-YSZ respectively. The power density for all three anodes as a function of time is shown in Figure 6.9.

VLY and CSCV showed low activity for methane electro-oxidation at low current density, 5 mA cm^{-2}, drawn from the cell during the experiment. They each had small amounts of carbon deposited on the surface under these conditions, and CSCV had more carbon deposited than VLY. While CSCV had a higher TPO CO_2 evolution temperature, 850 K, the resilience of the deposited carbon for this anode increased from Type I to Type III tests.

The Ni-YSZ anode catalyst was biased potentiostatically at 0.5 V and the current fell steadily during the 6 h tests, from an initial value of 40 mA cm^{-2} to 24 mA cm^{-2} as a result of the coking of the Ni anode. There was an initial increase in performance, due to an increase in electronic conductivity as a result of the deposited carbon. Ni-YSZ had TPO CO_2 evolution temperatures at 810 and 850 K which were similar to those under Type I and II conditions. The amount of carbon deposited on all three anodes was similar to that deposited during Type I, and less than that deposited during Type II.

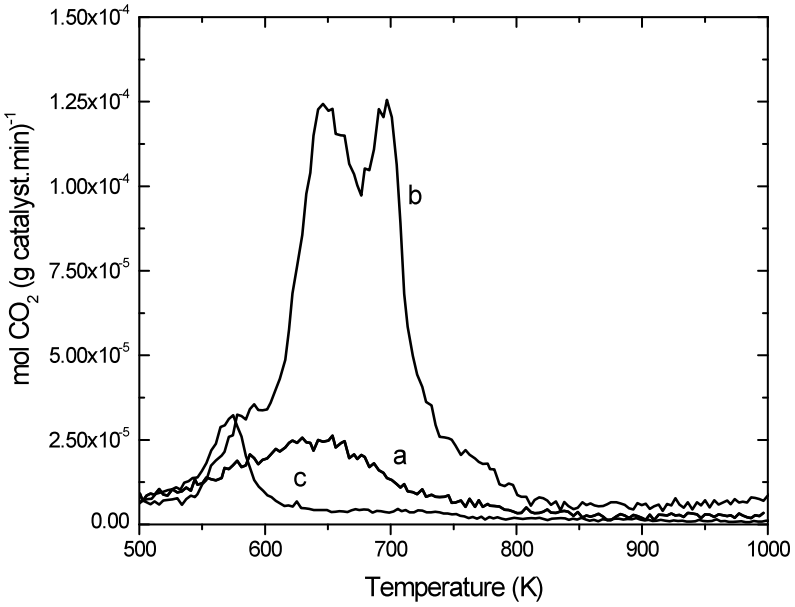

Figure 6.5: Amount of evolved CO_2 from carbon deposited on VLY under a) Type I, b) Type II and c) Type III conditions.

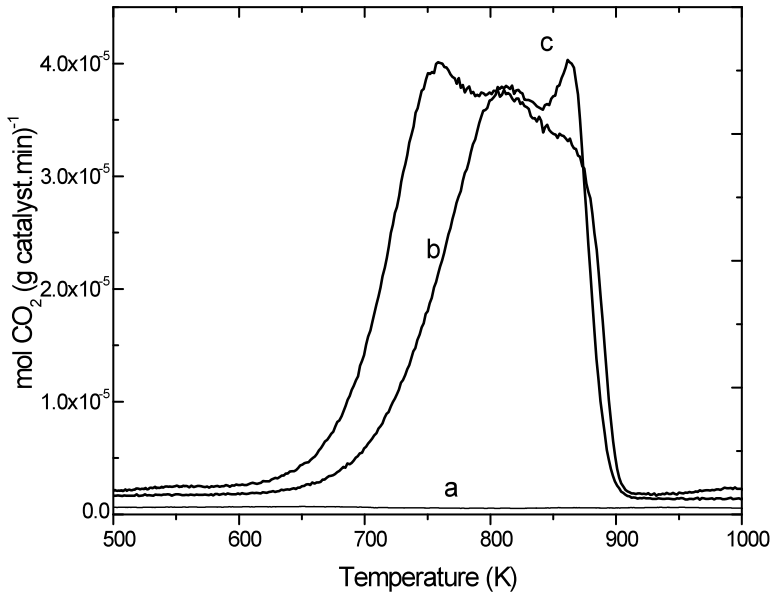

Figure 6.6: Amount of evolved CO_2 from carbon deposited on CSCV under a) Type I, b) Type II and c) Type III conditions.

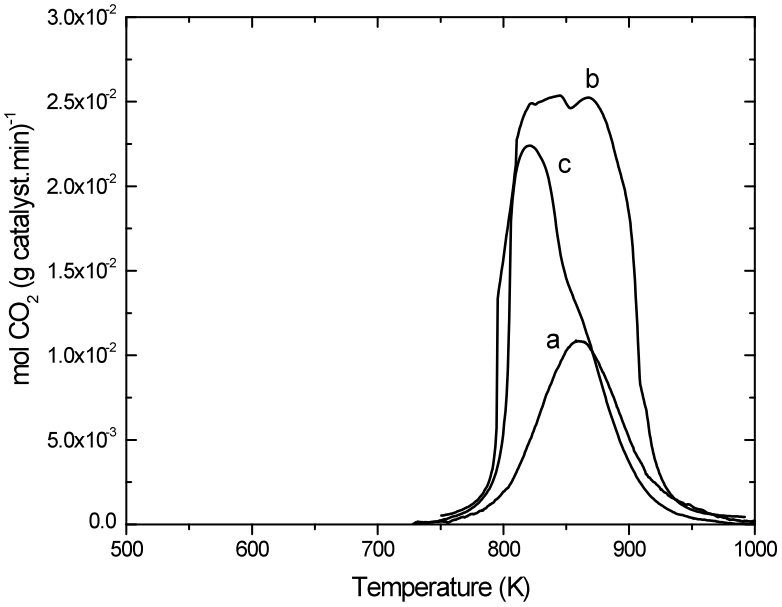

Figure 6.7: Amount of evolved CO_2 from carbon deposited on Ni-YSZ under a) Type I, b) Type II and c) Type III conditions.

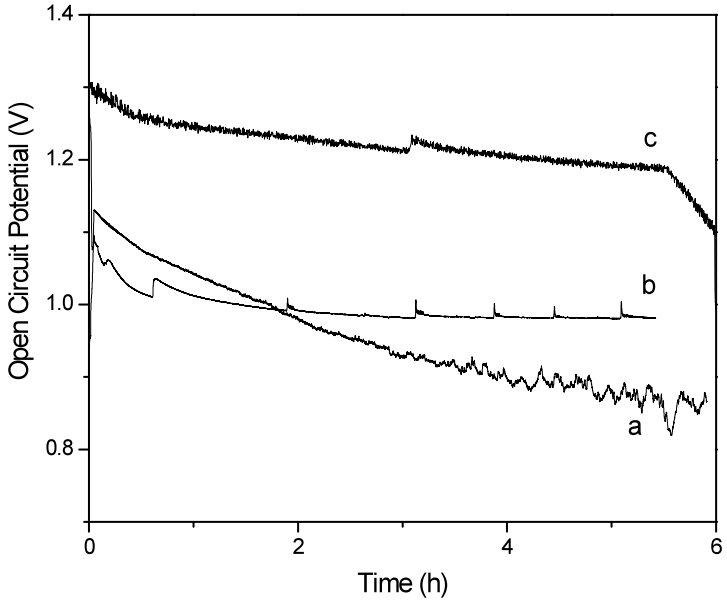

Figure 6.8: Change in open circuit voltage (Type II) over time in pure methane for anodes a) VLY, b) CSCV and c) Ni-YSZ.

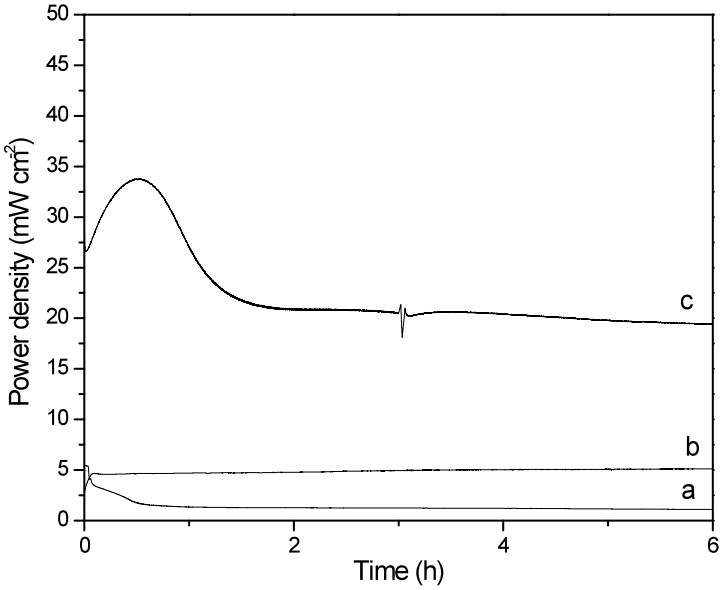

Figure 6.9: Change in power output (Type III) over time in pure methane for anodes a) VLY, b) CSCV and c) Ni-YSZ.

6.3 Discussion

Both VLY and CSCV oxide anode catalysts showed coking resistance superior to that of nickel containing catalysts under the same experimental conditions. The nickel containing catalyst evolved more CO_2 during TPO, and CO_2 evolution required a much higher temperature, 850 K, indicating a more refractory type of carbon deposit, seen as carbon fibers (whiskers) when imaged using SEM (Figures 6.4f). This was true under all three experimental conditions. These results indicated that the oxide catalysts had higher coking resistance than the nickel containing catalysts under both low oxygen conditions (absence of O^{2-} flux) and catalytic cracking conditions (absence of applied electric field). The low temperature required during TPO for evolution of CO_2 from coked VLY indicated that the carbon present was not bonded strongly to the catalyst, allowing it to be easily oxidized, when compared to the other cases in which a higher temperature was required for oxidation. The temperature was virtually the same for evolution of CO_2 from oxidation of carbon deposited on CSCV and Ni-YSZ during TPO, indicating that the carbon present in these catalysts was of the same type. Nickel catalyzed the cracking of methane to a much greater extent, and the deposited carbon was of a more refractory form, while neither VLY nor CSCV alone catalyzed methane cracking to a substantial degree.

Under Type II conditions VLY showed the lowest amount of deposited carbon. All three anodes had an increase in the amount of deposited carbon when compared to Type I coking

Table 6.1: Total amount of carbon removed as CO_2 from catalysts.

	Total carbon		(mol C(g catalyst)$^{-1}$))
Sample	Type I	Type II	Type III
VLY	3.03 x 10^{-4}	1.84 x 10^{-3}	5.61 x 10^{-4}
CSCV	5.00 x 10^{-7}	1.01 x 10^{-3}	6.77 x 10^{-4}
Ni-YSZ	9.29 x 10^{-2}	2.77 x 10^{-1}	1.65 x 10^{-1}

Table 6.2: Temperatures at maxima of TPO peaks for evolution of CO_2 from different catalysts.

	T max	(K)	
Sample	Type I	Type II	Type III
VLY	574/722	646/697	642
CSCV	644/945	750/804/981	805/855
Ni-YSZ	862	826/860	814/852

conditions. It was expected that any given catalyst would have the same amount of carbon deposited under OCV conditions as under no circuit condition, because the concentration of available oxygen in the anode chamber would be identical. This condition should be very similar to the Type I condition as there is no potential gradient for oxygen across the membrane, and so the oxygen partial pressure should be similar. The main difference is the presence of the gold current collector mesh in contact with the anode. The environment at the anode should not be perturbed by the presence of the gold current collector which, due to its low activity towards methane cracking and low surface area (gold mesh), was not anticipated to contribute to carbon deposition [7, 8]. Again the condition should only encompass catalytic cracking, without the possibility of C removal by reactions 3.9 and 3.11 at any appreciable rates because OCV necessitates an equilibrium condition. Thus the presence of the gold current collector mesh must have led to an increase in catalytic cracking of methane at the interface between the anode and the current collector which resulted in carbon depositing on the surface.

Type III condition differed greatly from Type I and II conditions, since there was an applied electric field, and so both electrocatalytic reactions 3.6, 3.7, 3.9, 3.11 and catalytic reaction 3.8 were capable of playing a role in the reaction mechanism(s), and the oxygen partial pressure was greater due to the induced oxygen ion flux. Interestingly, all materials had very similar carbon deposition amounts, in contrast to coking under Type I conditions. When compared to results found under Type II conditions, all three anodes had lower carbon deposition amounts. Under an applied current (Type III) either continual regeneration of surface O species from the ionic flux or the product of the reaction, H_2O, ensured that sources of O were present in quantities such that it would participate in removal of the

deposited carbon, reactions 3.9 and 3.11. Hence, the enhancement of carbon deposition as a result of the current collector experienced under Type II conditions is counterbalanced under Type III conditions by mechanisms for the removal of carbon.

6.4 Conclusions

- TPO experiments revealed that similar amounts of carbon (amount of carbon per g catalyst) were deposited on the surfaces of CSCV and VLY, and that total deposition was dependent on operating conditions. In all cases at least two orders of magnitude less carbon was deposited on the oxide anodes when compared to Ni-YSZ anodes.
- VLY and CSCV, hydrogen sulfide active anode catalysts, can be used to desulphurize a hydrocarbon stream under Type I-III conditions without building up significant carbon deposits.
- Ex-situ coking, Type I conditions, of potential anode materials is an adequate method for prediction of coking behaviour under electrochemical conditions.
- The gold current collector mesh contributed to an increase in carbon deposition during electrochemical coking tests, Type II and Type III conditions. However, under an applied potential , Type III condition, the availability and amount of O^{2-} and produced H_2O was sufficient to remove some or all of the carbon deposited as a consequence of the effect of the gold current collector.

6.5 References

[1] Z.R. Xu, J.L. Luo, K.T. Chuang, A.R. Sanger, J. Phys. Chem. C, 111 (2007) 16679-16685.
[2] N. Danilovic, J.L. Luo, K.T. Chuang, A.R. Sanger, J. Power Sources, 192 (2009) 247-257.
[3] N. Danilovic, J.L. Luo, K.T. Chuang, A.R. Sanger, J. Power Sources, 194 (2009) 252-262.
[4] J. Sehested, Catal. Today, 111 (2006) 103-110.
[5] N.C. Triantafyllopoulos, and S.G. Neophytides, J. Catal., 239 (2006) 187-199.
[6] M. K. Bruce, M. van den Bossche, S. McIntosh, J. Electrochem. Soc., 155 (2008) B1202-B1209.
[7] O.A. Marina and M. Mogensen, Appl. Catal. A, 189 (1999) 117-126.
[8] O.A. Marina, V.A. Sobyanin, V.D. Belyaev, Mat. Sci. Eng., B13 (1992) 153-155.

Chapter 7

Correlation of fuel cell anode electrocatalytic and ex situ catalytic activity of perovskites $La_{0.75}Sr_{0.25}Cr_{0.5}X_{0.5}O_{3-\delta}$ (X= Ti, Mn, Fe, Co)

7.1 Introduction

The work in this chapter was designed to address the need for rational selection criteria in the fuel cell literature for anode materials. The present research was directed to determination of the relative catalytic activity of the family of perovskites, $La_{0.75}Sr_{0.25}Cr_{0.5}X_{0.5}O_{3-\delta}3$, and to provide data for rational development of future materials for SOFC anode materials. Herein I will show that the catalytic and electrocatalytic performance for conversion of H_2, CH_4 and CH_4/0.5%-H_2S of a series of catalysts having a common perovskite structure depends on the elemental composition of perovskites $La_{0.75}Sr_{0.25}Cr_{0.5}X_{0.5}O_{3-\delta}$ (LSCX; X = Co, Fe, Ti, Mn), in which X occupies the B site.

The series of perovskites having Cr in the B-site was selected as it was expected that Cr would impart redox stability to all of the structures [1-3]. The LSCX perovskites containing Mn, Fe and Ti are known, but have not been comparatively tested to establish any electrocatalytic selection rules across the 3d-series transition metal cations [4-9]. In addition, a Co containing perovskite, LSCCo, was tested and compared as a potentially catalytically active material. It is known that $Ce_{0.9}Sr_{0.1}Cr_{0.5}V_{0.5}O_3$ is relatively inactive for conversion of CH_4, and so this LSCV perovskite was not tested within this series [10, 11]. In addition, Ni, and Cu containing perovskites are known to be unstable at low oxygen partial pressures, leading to segregation of the metal [12-14], and so these members of the same family of materials also were excluded from testing.

A rapid evaluation technique is described using simultaneous DSC/TGA-MS for screening potential candidate catalysts for CH_4 activity and carbon deposition resistance in an

environment closely simulating anode fuel cell conditions [14-16]. It's utility will be demonstrated through comparison of the present series of perovskites for catalytic and electrocatalytic CH_4 conversion and stability in 5000 ppm H_2S.

I will show that the electrocatalytic activity for methane oxidation in a fuel cell correlates well with ex-situ temperature programmed catalytic conversion of CH_4, X = Co>Mn∼Fe>Ti, under temperature programmed reaction conditions in 5% CH_4/He. The total conductivity of the materials in air decreases with X = Co>Fe>Mn>Ti. Within the series of catalysts the order of maximum fuel cell power density depends on feed: CH_4, X = Fe>Mn>Ti; H_2, X = Fe>Mn>Ti; and 0.5% H_2S/CH_4, X = Ti>Fe>Mn. The Co-containing catalyst is unstable under reducing conditions. A process is proposed to explain the difference in catalyst order and enhanced activities in H_2S/CH_4 as fuel compared to CH_4 alone.

7.2 Experimental

7.2.1 Catalyst preparation

LSC and LSCX catalyst powders were prepared using combustion gel synthesis. Initially, stoichiometric amounts of the nitrates $La(NO_3)_3{\cdot}6H_2O$ (Alfa Aesaer, 99.9%), $Sr(NO_3)_2{\cdot}6H_2O$ (Alfa Aesaer, 99%), $Co(NO_3)_2{\cdot}6H_2O$ (Sigma Aldrich, 98%), $Fe(NO_3)_3{\cdot}9H_2O$ (BDH, 98%), $Mn(NO_3)_2$ solution (Alfa Aesaer, 99%), $Cr(NO_3)_3{\cdot}9H_2O$ (Acros Organics, 99%), $Ce(NO3_3)_3{\cdot}6H_2O$ (Acros Organics, 99.5%), $Gd(NO_3)_3{\cdot}6H_2O$ (Sigma Aldrich, 99.9%) were mixed in water. The mixture was stirred on a hot plate at 90 ^{o}C. Citric acid was added to form a 2:1 ratio of acid to metal cations. Ammonium hydroxide (Fisher Scientific) was added to balance the pH to 7. The mixture was stirred further on the hot plate at 90 ^{o}C for several hours until the water had evaporated. The temperature was increased to 100 ^{o}C to form a gel. Once the gel was formed the beaker was placed directly into a combustion furnace at 500 ^{o}C. After 30 min the temperature was increased to 600 ^{o}C and held at that value for 1 h to combust all carbonaceous material from the mixture. The porous foams that formed were ground using a mortar and pestle and then calcined in air at 1000 ^{o}C for 4 h. The resulting powders were dispersed in isopropanol, then milled overnight in a ZrO_2 ball mill with ZrO_2 balls. LSCTi was prepared via a different procedure using titanium isopropoxide (Sigma Aldrich, 98%). Chromium deficient $La_{0.75}Sr_{0.25}Cr_{0.5}\bigcirc_{0.5}O_{3-\delta}$ ($\bigcirc$ representing a missing B-site cation) was prepared by the gel combustion process above and the resulting powder was dispersed in distilled water and stirred to form a suspension at 80 ^{o}C, into which the stoichiometric amount of titanium isopropoxide was injected. The resulting solution was dried and ground before calcining in air at 1000 ^{o}C for 4 h. Rapid hydrolsis of titanium isopropoxide when exposed to air ultimately results in clustering of Ti in the resulting perovskite, which is not the case for the other perovskites as the cations are well distributed in the strucutre.

Investigation of the potential utility of the present catalysts was extended by preparation

and testing of composite catalysts combining the benefits of additional components having complementary activity with that of the substituted perovskites. Composite $Ce_{0.9}Gd_{0.1}O_2$ (GDC)-LSCX catalysts in 50-50 mass ratio were milled for 24 h.

7.2.2 Temperature programmed analysis

Temperature programmed analyses were conducted using simultaneous differential scanning calorimetry-thermogravimetric analysis-mass spectrometry (DSC-TGA-MS) using a TA Instruments SDT Q600 connected to a mass spectrometer (Pfeiffer Thermostar GSD 301). The two instruments were connected by a transfer line maintained at 200 ^{o}C. The following reactions were performed sequentially on catalyst powders: oxidation in 5% O_2/He, reduction in 1% H_2/He, re-oxidation in 5% O_2/He, temperature programmed reaction (TPR) with methane in 5% CH_4/He, and temperature programmed oxidation (TPO) in 5% O_2/He. A flow rate of 100 mL min^{-1} was used in all experiments, except for the reaction in CH_4/He where a flow rate of 500 mL min^{-1} was utilized to minimize the effect of gas phase thermal reactions. An accurately measured sample of about 5 mg of powder was placed in an alumina cup (90 μL), then the system was purged for 30 min using 100 mL min^{-1} flowing He prior to testing. The samples were then heated to 1000 ^{o}C at 20 ^{o}C min^{-1}. The samples were not exposed to air between tests.

7.2.3 Conductivity testing

Conductivity measurements were conducted using a NorECs Probostat electrochemical measurement cell in atmospheres that were either air or 5% H_2/Ar. Cylindrical pellets were prepared by pressing powdered catalyst at 2 tonnes in a 1 cm ID die and sintering for 2 h at the following temperatures: LSCFe, 1400 ^{o}C; LSCCo, 1350 ^{o}C; LSCTi, 1550 ^{o}C; and LSCMn, 1400 ^{o}C. The samples were heated at 2 ^{o}C min^{-1} to prescribed temperatures 500-950 ^{o}C at which tests were performed. The samples were held at testing temperature until the conductivity value was stable. The measurements were performed using the four-point van der Pauw DC technique with platinum point contacts.

7.2.4 Fuel cell testing

MEAs having the configuration LSCX | YSZ (0.3 mm) | Pt were prepared, installed and tested in the fuel cell testing apparatus shown in ∮ 5 [10]. Gold paint was applied to the anode as a current collector, and sintered in-situ. The anode and cathode chamber gas flow rates were each 100 mL min^{-1}, and the chamber volume was close to 80 mL, so the residual time for the gases was about 0.8 min. The anode feed was humidified by bubbling the anode gas through DI water at RT, this ensures about 3% H_2O in the anode gas (humified anode feeds are those specifically indicated).

MEAs were tested at each temperature, 800 ^{o}C, 850 ^{o}C and 900 ^{o}C, consecutively. The fuels used for testing were varied in the following order H_2, CH_4 and 0.5% H_2S/CH_4. The

cells were held at open circuit voltage (OCV) for at least 30 min after switching fuels or changing temperature, and for 5-10 min after each potentiodynamic and impedance test. Potentiostatic tests at an uncompensated cell voltage of 0.7 V were conducted at 850 ^{o}C for 6 h for each MEA following completion of the sequence of potentiodynamic tests and then cooling the cell from 900 ^{o}C to 850 ^{o}C and holding it at that temperature.

7.2.5 Materials characterization

A Rigaku RU200 Powder X-ray diffraction (XRD) system with a rotating anode and a Co target was used for analysis of all synthesized powders, with a scan rate of 2 θ^{o} min^{-1}. The commercially available software Jade was used for identification of phases in the samples. A Hitachi S-4800 field emission scanning electron microscope (SEM) was used for characterizing cross-sections of MEAs. Quantachrome Instruments Autosorb I was used for BET surface area determination of freshly prepared catalysts using He gas. Elemental analyses using ICP-MS were conducted utilizing a Perkin Elmer Elan 6000 and solutions prepared by digesting the powders in a mixture of nitric and hydrochloric acids at 125 ^{o}C. A Setaram Setsys Evolution dilatometer was used to determine the thermal expansion coefficients (TEC) of samples in flowing air.

7.3 Results

7.3.1 Materials characterization

The XRD patterns of the prepared oxide powders (Figure 7.2) showed that all of the synthesized materials possessed perovskite structures with a tetragonal unit cell, similar to that of the $LaCrO_3$ parent (PDF# 24-1016). The dimensions of the unit cells were similar and varied with the size of the cation X (Table 7.1). The XRD patterns contained double peaks at high diffraction angles which were generated by the use of unfiltered Kα_2 X-rays. The BET surface areas of all the oxides were similar and high compared to powders prepared by conventional solid state synthesis. The TEC for each of LSCX (X = Mn, Fe) was compatible with that of YSZ and, therefore, unlikely to cause fracturing of the MEA through problems arising from differential TEC. However, LSCCo had a much larger TEC value than that of YSZ, used as electrolyte, and caused the anode to delaminate from the YSZ disk upon cooling of the sintered MEA. LSCTi was not tested in the dilatometer; however, experimentally there were no issues with TEC.

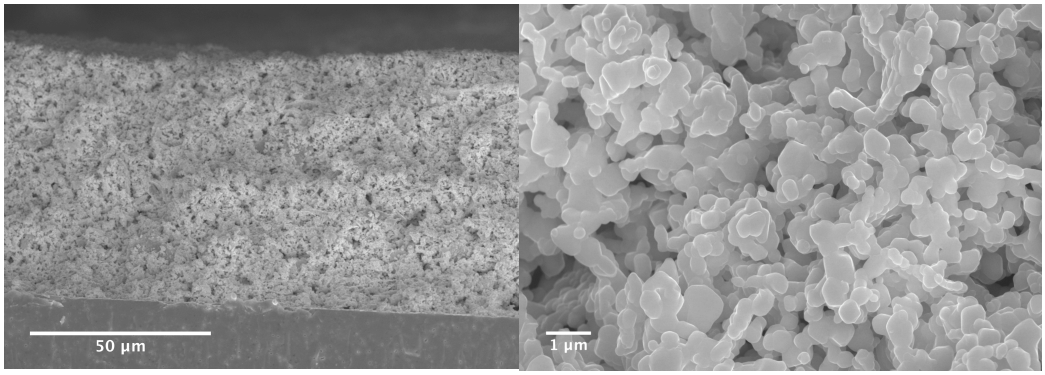

Figure 7.1: Cross-sectional SEM micrographs of a) crossection of prepared MEA having of LSCFe anode, and b) detail fo th anode structure.

SEM images of cross-sections of LSCFe anodes (Figure 7.1) showed that the anode adhered well to the YSZ electrolyte after sintering. Anode catalyst particles were well dispersed, well interconnected, and the structure had good porosity. LSCMn and LSCTi were similarly well-adhered and had similar porosity.

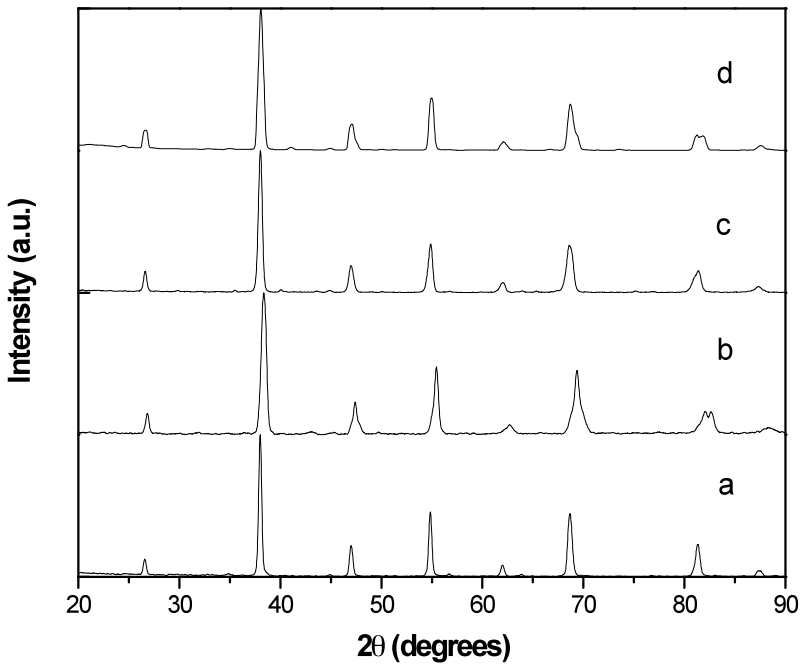

Figure 7.2: XRD patterns of a) LSCFe, b) LSCTi, c) LSCCo and d) LSCMn prepared by gel synthesis.

Electronic transport characterization showed that the conductivities of tested materials were in the order LSCCo>LSCFe>LSCMn>LSCTi in both air and hydrogen. All these

anode materials were mixed conductors. LSCCo was reduced in H_2 and this caused the pellet to crack, as detailed below. All materials, except for LSCCo, had total conductivity sufficiently high that they were suitable candidates for testing for anode catalyst applications. Table 7.1 compares the activation energies and conductivities for all tested anode materials at 800 ^{o}C, and the Arrhenius plots are shown in Figure 7.3.

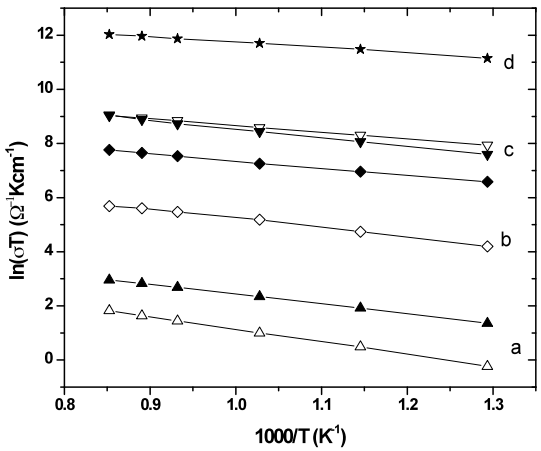

Figure 7.3: Conductivity comparison for a) LSCTi, b) LSCMn, c) LSCFe and d) LSCCo in air (full symbols) and humidified 5%H_2-Ar (clear symbols).

Of all the materials tested, only LSCCo was reduced in the 2%H_2/Ar stream, and peaks for Co metal were present in the XRD spectrum of reduced material. There were no secondary phases detectable using XRD following heating of 50-50 wt% mixtures of LSCX-YSZ (1200 ^{o}C, 6 h) in air or in 2%H_2/Ar.

Table 7.1: Summary of anode materials properties.

Materials	LSCTi	LSCMn	LSCFe	LSCCo
Elemental (La/Sr)	0.73/0.26	0.82/0.18	0.8/0.2	0.8/0.2
Comp. ICP (Cr/X)	0.45/0.55	0.44/0.56	0.5/0.5	0.48/0.52
BET surface area (m^2g^{-1})	5.22	4.28	5.61	3.60
σ_{total} in Air	1.37 x 10^{-2}	1.75 x 10^{-1}	5.73	133.58
in H_2	3.95 x 10^{-3}	2.22	6.45	N/A
@ 800 ^{o}C / (Scm^{-1})				
Ea in Air/H_2 (eV)	0.72/0.91	0.53/0.68	0.64/0.49	0.39/N/A
TEC (K^{-1})	N/A	10.8 x $10^{-6} from$[17]	11.8 x 10^{-6}	19.5 x 10^{-6}

7.3.2 Temperature programmed analysis

The MS data during TPR for all of the catalysts is shown in Figure 7.4, and the corresponding TGA and DSC data (acquired simultaneously) are in Figures 7.5 and 7.6. The TPR data showed that the order of catalytic activity or methane oxidation (based on the normalized CO_2 evolved; Table 7.2) is LSCCo>LSCMn>LSCFe>LSCTi. The CO_2 MS signals indicated initial deep methane oxidation in which lattice oxygen reacted with methane, after which H_2 was formed concurrently with the onset of carbon deposition after all readily available lattice oxygen was spent. The oxidation of methane correlated directly with the reduction in mass of the samples through loss of oxygen (TGA, Figure 7.5), and the oxidation reaction was evident as corresponding DSC peaks (Figure 7.6). No similar DSC peak was present in the test using LSCTi, no CO_2 was formed, and the weight of the LSCTi sample remained constant, indicating that LSCTi had no significant activity for oxidation of CH_4. In contrast, each of LSCCo, LSCFe and LSCMn was an active oxidizer.

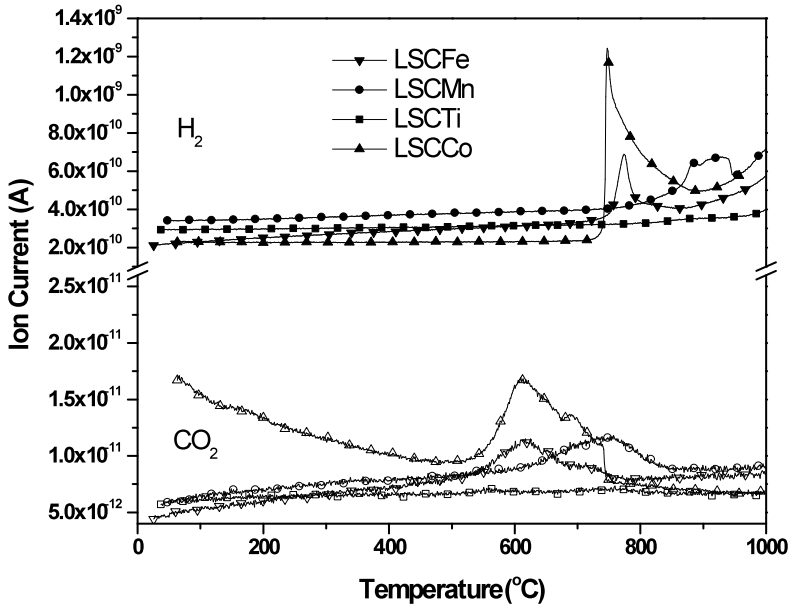

Figure 7.4: MS data during TPR of oxide anode materials in 5% CH_4.

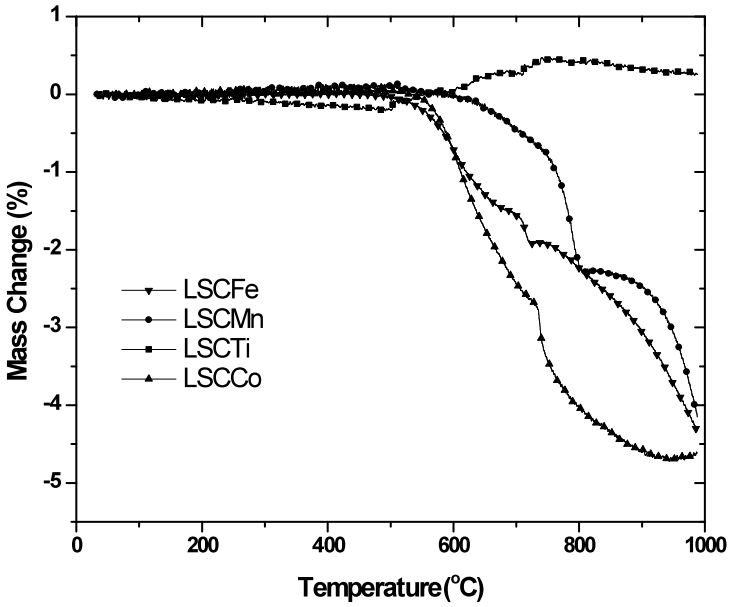

Figure 7.5: TGA data during TPR of oxide anode materials in 5% CH_4.

After all available surface O was depleted, carbonaceous deposits were formed on all of the materials during prolonged heating under flowing CH_4-He. When the materials were then heated in air CO_2 was formed, providing a quantitative measure of the carbon deposited (Figure 7.7). When the deposited carbonaceous deposits included both C and H, there were also H_2O evolution peaks. The amount of deposited carbon was similar for all tested materials, and the temperatures for on-set of evolution of CO_2 were each in the range 400-600 ^oC (Table 7.3). Only reactions of CH_4-He over LSCCo and LSCFe formed C- and H-containing carbonaceous deposits, which then gave rise to H_2O evolution starting at about 225 ^oC and occurring in two stages. TGA and DSC curves (Figures 7.8 and 7.9) showed that all of the materials that were reduced under CH_4-He were reoxidized fully during TPO.

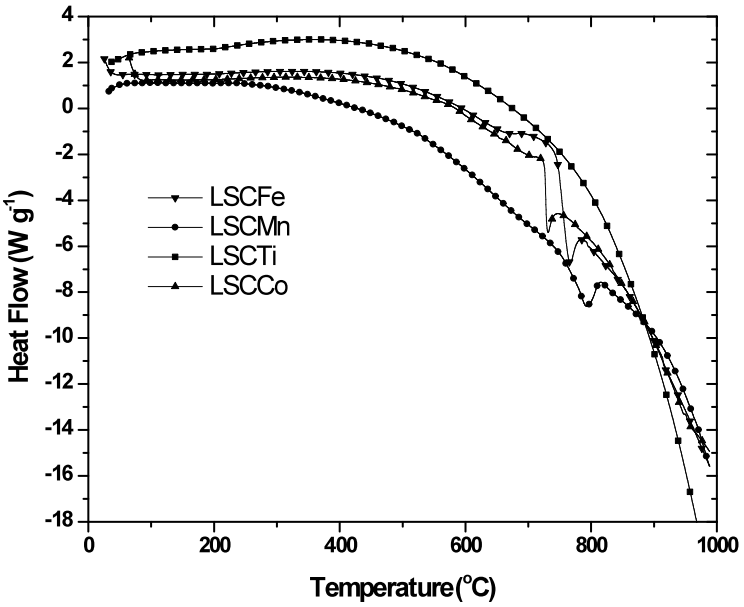

Figure 7.6: DSC data during TPR of oxide anode materials in 5% CH_4.

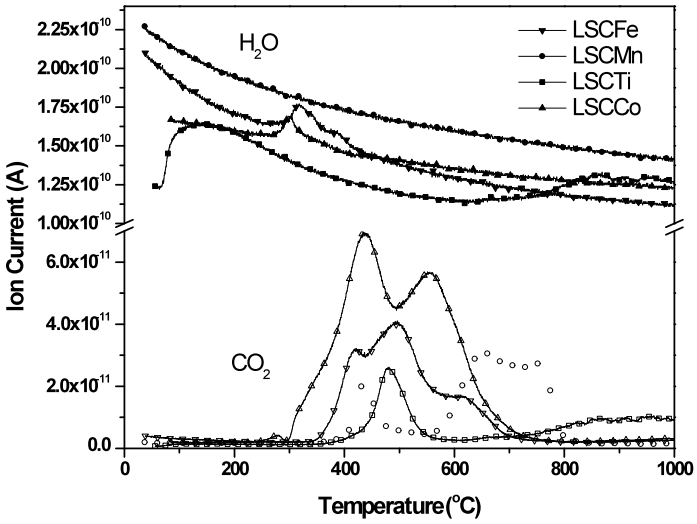

Figure 7.7: MS data during TPO of oxide anode materials in 5% O_2.

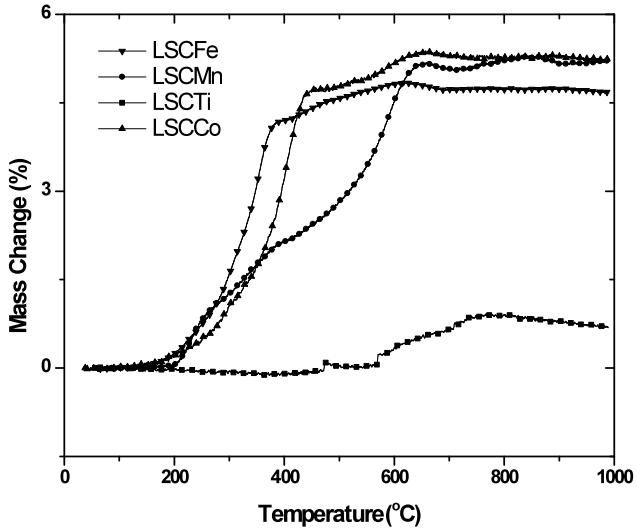

Figure 7.8: TGA data during TPO of oxide anode materials in 5% O_2.

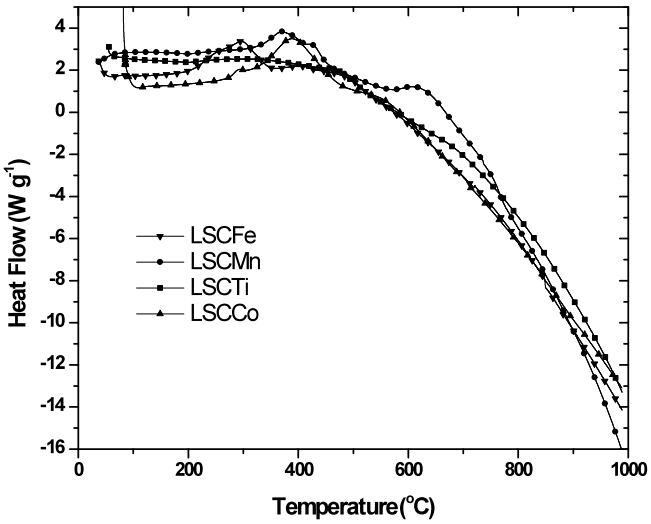

Figure 7.9: DSC data during TPO of oxide anode materials in 5% O_2.

7.3.3 Electrochemical characterization

Typical potentiodynamic performance curves are shown in Figure 7.10 for a fuel cell using LSCFe at 850 ^oC, and the corresponding impedance spectra for all materials, temperatures and dry gases used are shown in Figure 7.12. LSCFe was tested in humidified sour gas,

Table 7.2: Normalized CO_2 evolution during TPR of CH_4 with LSCX.

Materials	CO_2 evolved (A g ^oC m^{-2})
LSCTi	N/A
LSCMn	8.73 x 10 $^{-11}$
LSCFe	6.74 x 10 $^{-11}$
LSCCo	6.20 x 10 $^{-10}$

Table 7.3: Normalized CO_2 evolution during TPO of carbonaceous deposits with O_2.

Materials	CO_2 evolved (A g ^oC m^{-2})
LSCTi	8.74 x 10 $^{-10}$
LSCMn	1.43 x 10 $^{-9}$
LSCFe	1.18 x 10 $^{-9}$
LSCCo	3.98 x 10 $^{-9}$

as shown in 7.11, and in comparison to 7.10 the fuel cell did not achieve the same power output. Therefore all electrochemical testing was done in dry gases (no humidification).

Maximum power densities for all LSCX materials, fuels and temperatures are summarized in Figures 7.13-7.15. The fuel cell performance in CH_4 was the lowest achieved using any of the tested fuels, and there were significant anode limitations, shown as a rapid reduction in current density starting around 0.5 V. This suggests that either at higher potentials methane electrooxidation is no longer activated or the limit of charge transfer between the catalyst and adsorbed gas is reached. Each of the oxides except for LSCTi performed very well in H_2 (Figure 7.13). LSCTi showed no apparent activity for activation of either CH_4 or H_2 (Figures 7.13 and 7.14). All of the anodes were active in 0.5% H_2S/CH_4 feed (Figure 7.15).

At OCV the impedance curves in H_2 showed low polarization resistance values for each anode, higher values in 0.5% H_2S/CH_4 and very high values in CH_4. In sour gas and CH_4 the polarization resistances decreased drastically with the application of overvoltage during impedance measurements. The rankings of the activities of LSCX oxides (X = Ti, Mn, Fe) according to power density values in the different feeds were: H_2, Fe>Mn>Ti; CH_4, Fe>Mn>Ti; and 0.5% H_2S/CH_4, Fe>Mn>Ti at 800 ^oC and 850 ^oC, and Ti>Mn>Fe at 900 ^oC.

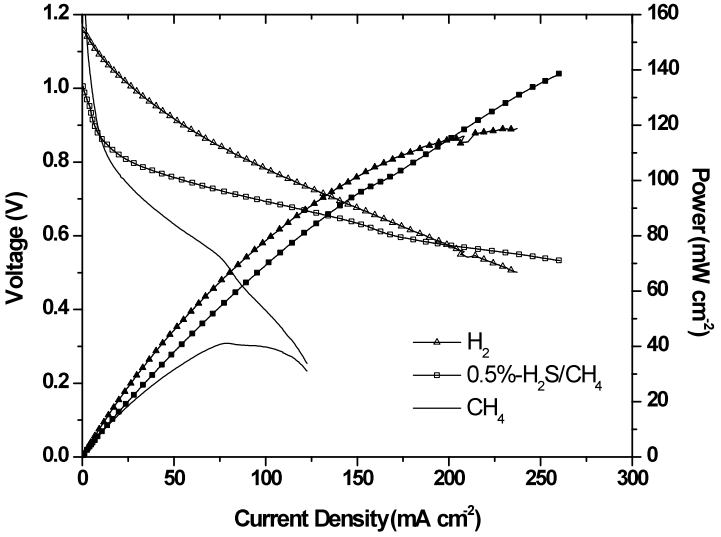

Figure 7.10: Potentiodynamic curves for LSCFe | YSZ | Pt at 850 ^{o}C.

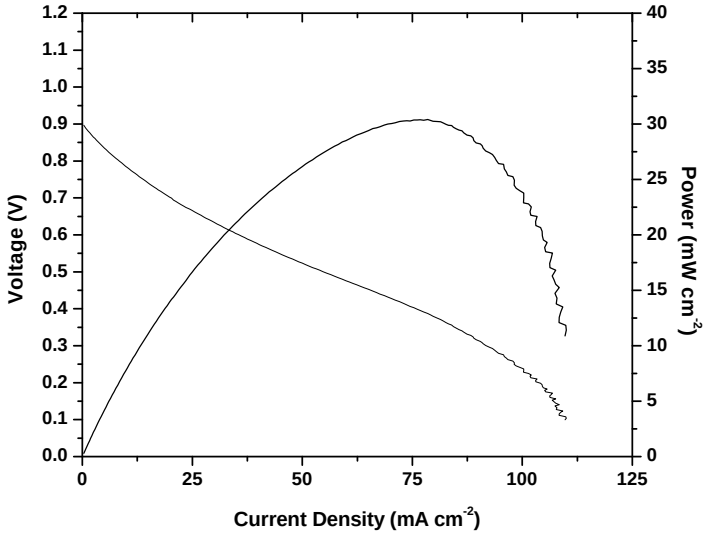

Figure 7.11: Potentiodynamic curve for LSCFe | YSZ | Pt at 850 ^{o}C in 0.5 % H_2S-CH_4 (3%H_2O).

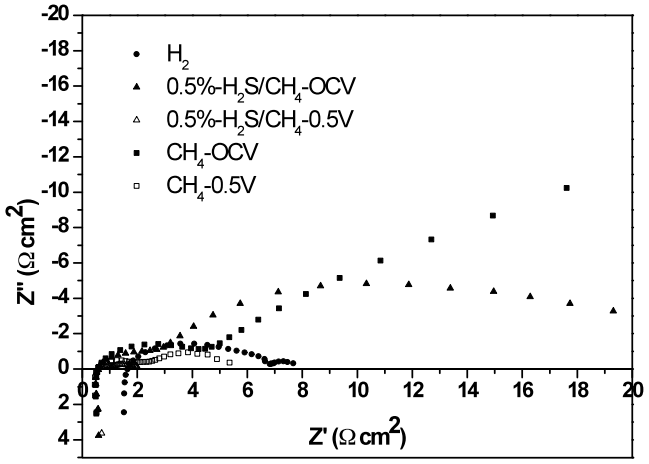

Figure 7.12: Impedance spectra for LSCFe | YSZ | Pt at 850 ^{o}C.

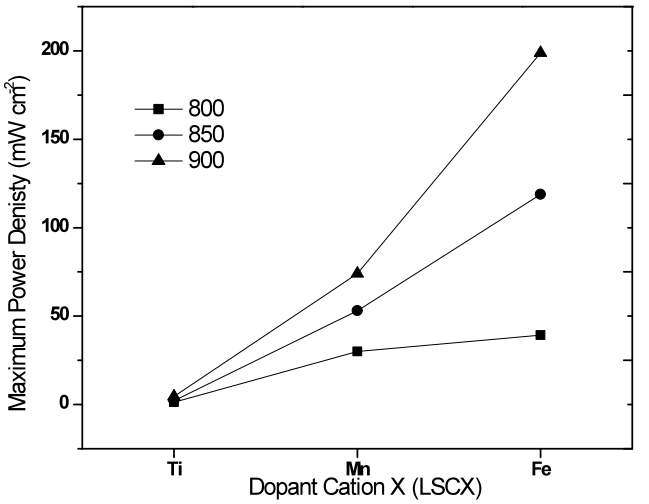

Figure 7.13: Dependence of performance on substituent cation using H_2 feed.

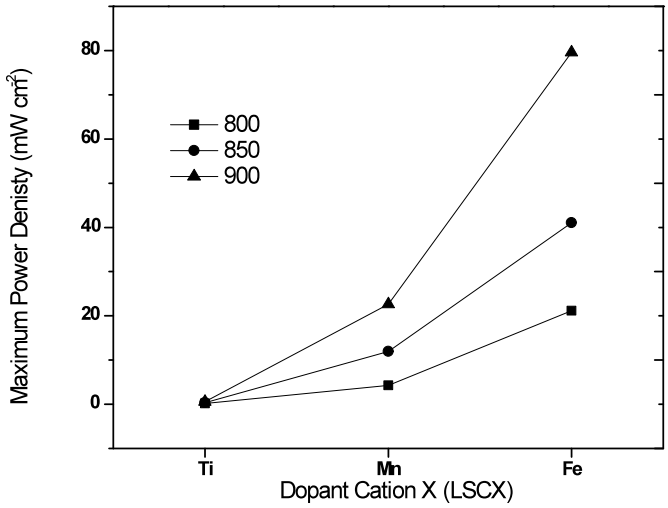

Figure 7.14: Dependence of performance on substituent cation using CH_4 feed.

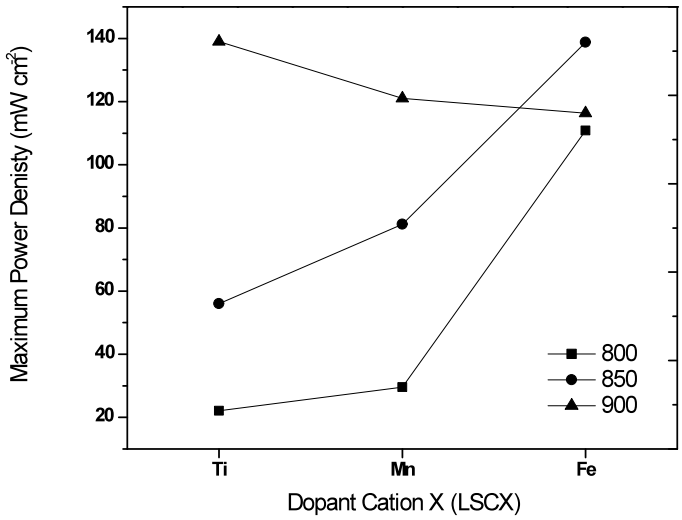

Figure 7.15: Dependence of performance on substituent cation using 0.5% H_2S/CH_4 feed.

Potentiostatic tests were conducted in CH_4 and 0.5% H_2S-CH_4 for 6 h (Figure 7.16). Initially, the highest power was achieved using LSCTi in 0.5% H_2S/CH_4; however, there was a significant reduction in performance (ca. 25%) during the 6 h test. Long term performance of LSCTi in CH_4 was low and stable. While LSCFe had the second highest power output in CH_4, again there was significant reduction (>20%) in performance over 6 h. The performance of LSCFe was stable in 0.5% H_2S/CH_4. LSCMn had similar stable, lower

power outputs in either CH_4 or 0.5% H_2S/CH_4, suggesting that there was little influence from the presence of H_2S in this case.

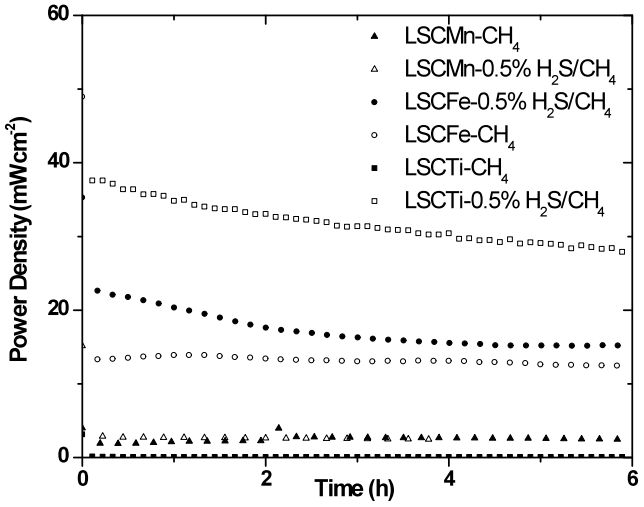

Figure 7.16: Long term potentiostatic test at 0.7 V of LSCFe | YSZ | Pt at 850 ^oC.

In an attempt to improve sinterability of MEA and to enhance anode catalyst activity through introduction of complementary capability, I compared performances of composite anodes comprising mixtures of LSCX with $Ce_{0.9}Ga_{0.1}O_{2-\delta}$ (GDC). The performances of the composites were in each case superior to those of the single component LSCX anodes at all temperatures. A typical performance curve is shown in Figure 7.17 for a fuel cell using the LSCFe-GDC composite anode at 850 ^oC, and the corresponding impedance curve is shown in Figure 7.18. The maximum power densities for all composite anodes with each feed are shown in Figure 7.19. With the addition of GDC to LSCCo it still was possible to sinter various suitable combinations of anode and electrolyte to form MEAs, even when there was a mismatch of expansion coefficients between the anode and the YSZ electrolyte. The polarization resistances and ohmic resistances of all composite anodes were reduced compared to the corresponding LSCX alone. However, it was found again that there were similar limiting current losses when using CH_4 as a fuel. The highest power densities were achieved using H_2 as a fuel, while in 0.5% H_2S/CH_4 the maximum power density was approximately 50% of that value. The highest power density, almost 250 mW cm^{-2}, was achieved in H_2 using LSCFe-GDC as the anode. The ranking of the LSCX-GDC composite anodes according to maximum power density values using the different fuels was: H_2, Fe>Mn>Co>Ti; CH_4, Fe>Co>Mn>Ti; and 0.5% H_2S/CH_4, Fe>Ti>Mn>Co. It is noteworthy that the composite anodes containing LSCCo-GDC were more stable during testing, in contrast to LSCCo alone.

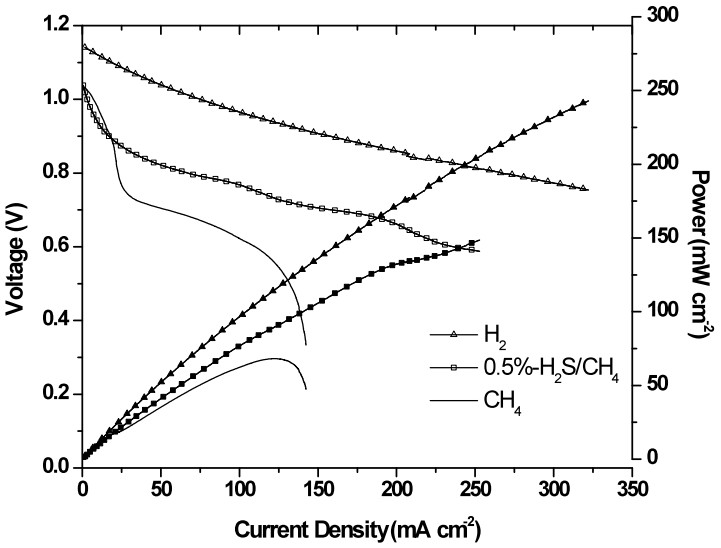

Figure 7.17: Potentiodynamic curves for LSCFe | YSZ | Pt at 850 ^{o}C.

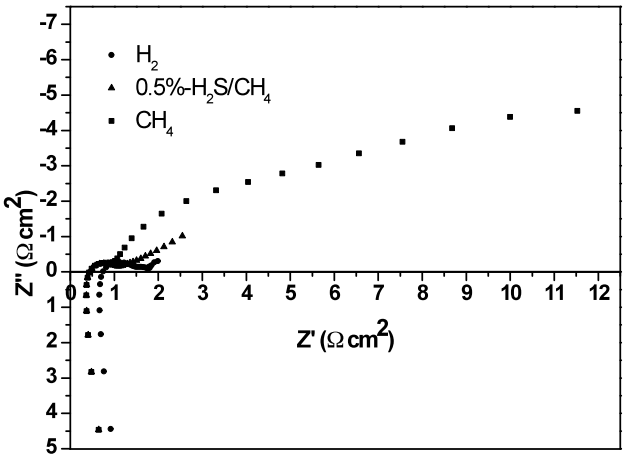

Figure 7.18: Impedance spectra for LSCFe | YSZ | Pt at 850 ^{o}C.

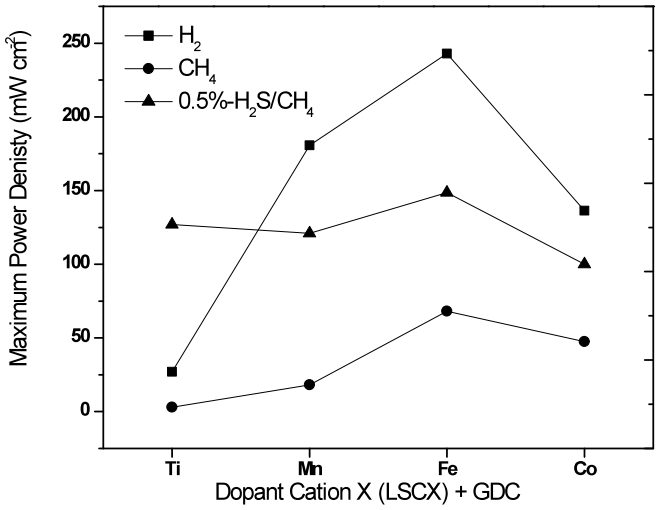

Figure 7.19: Summary of effectiveness of GDC on anodes' performances at 850 ^{o}C.

A mass spectrometer was connected to the outlet of the anode compartment of the fuel cell to analyze the effluent gas so as to determine the products formed and thereby gain insight into the process and reaction mechanism. The gas was analyzed before, during a potentiodynamic sweep (0 V to OCV), and after that sweep. The results for LSCFe-GDC at 850 ^{o}C are shown in Figure 7.20. CO_2 and H_2O were produced when CH_4 was used as a fuel, while the effluent contained CS2, CO_2, SO_2 and H_2O when 0.5% H_2S-CH_4 was used over all LSCX-GDC composites at all temperatures. The exceptions were LSCCo-GDC which was readily reduced, as described above, and LSCTi which had essentially no activity in pure CH_4, although CO_2 was produced when 0.5% H_2S/CH_4 was used as the fuel.

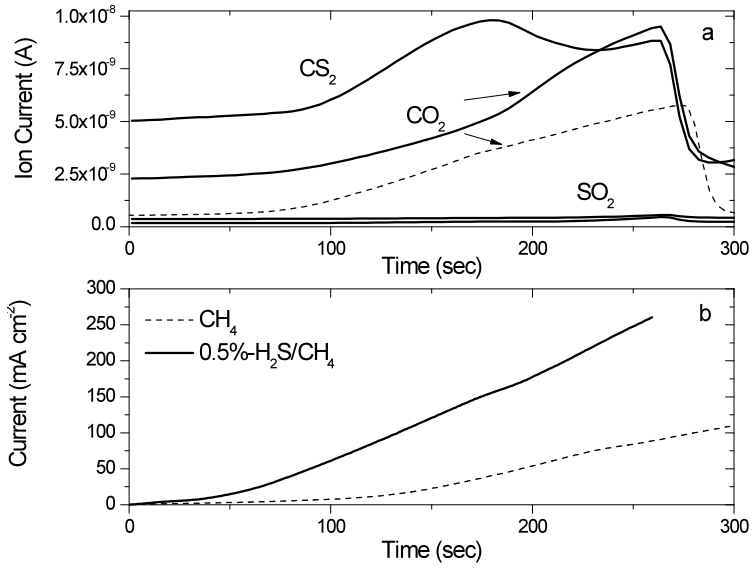

Figure 7.20: Variation of a) anodic cell exhaust with b) cell current for LSCFe—YSZ—Pt at 850 ^{o}C.

7.4 Discussion

Conductivity, TEC and surface area measurements indicated that all four LSCX oxides have comparable structures and physical and electrical properties. The oxides where X = Ti, Mn or Fe all were stable under reducing conditions, but LSCCo was not and so that material was unsuitable for use as a fuel cell anode material.

In conventional TPR, oxygen is fed with methane over a heterogeneous catalyst and the methane oxidation reaction (7.1) occurs over the surface, as previously performed using LSCFe and LSCMn [7, 18]. While there is a relationship between these tests and fuel cell experiments, the test conditions do not truly represent the fuel cell anode environment. In this study the CH_4 TPR was conducted without co-feeding oxygen, and the oxygen necessary for the methane oxidation reaction was provided from the catalyst, as initially described by Baker and Metcalfe [14-16] and more recently by Mcintosh et al. [19, 20] specifically for LSCMn.

$$CH_4 + 2O_2 \Rightarrow CO_2 + 2H_2O \tag{7.1}$$

A good fuel cell catalyst would provide oxygen, replenished by conduction of oxide ions via the electrolyte, while retaining its structure, thereby retaining physical integrity and electrocatalytic activity without risking severance of the bonding to the electrolyte. The equivalent electrochemical reaction in the fuel cell is (7.2).

$$CH_4 + 4O^{2-} \Rightarrow CO_2 + 2H_2O + 8e^- \tag{7.2}$$

The oxides LSCX, X = Ti, Mn, Fe, retained their structure during oxidation of CH_4, and were fully regenerated under O_2. However, LSCCo was not stable under reducing conditions. The TPR tests were conducted after a oxidation-reduction-reoxidation treatment to ensure that no carbonaceous contaminant was present on the surface. The temperature at which the oxidation reaction started to occur and the amount of CO/CO_2 released during TPR was indicative of the capability of the catalyst to activate methane. Three reaction characteristics were indicative of good activity of the catalyst: a lower initial reaction temperature, a greater amount of CO/CO_2 released, and a narrower CO/CO_2 peak. The most active oxidation catalysts were those containing cations to the right of Cr in the periodic table: Mn, Fe and Co. As Mn and Fe were the most active, they appeared to have the highest potential for activity as fuel cell catalysts.

All of the materials showed signs of coke formation, and the normalized amount of formed coke was similar for all materials. The temperature at which CO_2 was removed during TPO was indicative of the catalyst-coke bond strength. A low temperature for CO_2 evolution indicated that the deposited carbon was easily removed. In contrast, LSCMn had more refractory carbon deposits, since oxidation at 600-800 ^oC was required to remove the bulk of the coke as CO_2. LSCFe had the least refractory carbon, and the bulk of the CO_2 evolved between 400-500 ^oC. Secondly, evolution of water at 250-350 ^oC, as well as DSC peaks corresponding to exothermic heat evolved during the oxidation of carbonaceous deposits intimately bonded to the oxide powder, showed the presence of adsorbed CH_x species on the surface of LSCFe, LSCMn and LSCCo. Oxidation of the deposits on LSCTi did not produce a peak for H_2O, indicating that carbon was formed by cracking of methane in the gas stream.

Data from electrochemical testing of selected anode materials were in the same order as activities for CH_4-TPR: LSCFe was the most electrochemically active, followed by Mn and Ti. Additionally, CH_4 active catalysts were also active towards H_2 and 0.5% H_2S/CH_4, with a similar ranking in terms of activity. The anodes were most active in either H_2 or H_2S-containing CH_4. However, there was a severe limit on the current density above 0.5 V when CH_4 alone was used as fuel. When a low potential was applied the LSCFe anode was stable in CH_4 fuel but not in 0.5% H_2S/CH_4. LSCMn was stable in both fuels under potentiostatic conditions.

Addition of GDC to form composite anodes improved the oxygen ion conductivity of the anode and expanded the triple phase boundary area of each anode without affecting the order of activity using any of the fuels. By forming a composite of GDC and LSCCo it was possible to overcome the TEC mismatch, sinter and test a Co-containing anode for an MEA. LSCCo-GDC was not as active as LSCFe-GDC but was slightly more active than LSCMn-GDC, characteristic of a volcano type plot for activity when H_2 and CH_4 are used as fuel [9].

Compositions of MEAs with and without GDC were not optimized for performance;

however, the batches of each material were closely replicated for reproducibility of performance, with standard deviation within ±10%. Electrolyte supported cells all had Pt as the cathode, to enable comparison of anode performance.

The difference between performances in CH_4 and H_2S-CH_4 showed that the addition of H_2S changed either or both of the reaction mechanism and the surface state. The MS results revealed information about the process and the possible reaction mechanism occurring in the presence of H_2S. Not only was H_2S electrochemically oxidized (Eq. 7.3 and 7.4), it also appeared to participate in and affect the conversion of CH_4. CS_2 was produced, indicating the possibility that CH_4 first dissociated on the catalyst surface (Eq. 7.5), then reacted with surface S (*S) or a S-containing species (Eq. 7.6).

$$H_2S + O^{2-} \Rightarrow 0.5S_2 + H_2O + 2e^- \tag{7.3}$$

$$H_2S + 3O^{2-} \Rightarrow SO_2 + H_2O + 6e^- \tag{7.4}$$

$$CH_4 \Rightarrow *C + 2H_2 \tag{7.5}$$

$$*C + 2*S \Rightarrow CS_2 \tag{7.6}$$

This reaction path is not thermodynamically viable as reaction (7.7) has a positive free energy below 1000^oC.

$$C + 2H_2S \Rightarrow CS_2 + 2H_2 \quad (\Delta G_{850^oC} = 52.1 kJmol^{-1}) \tag{7.7}$$

And the methane hydrogen sulfide reforming reaction is only viable above 950^oC.

$$CH_4 + 2H_2S \Rightarrow CS_2 + 4H_2 \quad (\Delta G_{950^oC} = -1.9 kJmol^{-1}) \tag{7.8}$$

Alternatively, the sulfur may have provided adsorption sites between the oxide anode surface and CH_4, after which further reactions would form CS_2 (Eq. 7.9).

$$*H - S + CH_4 \Rightarrow *H - S - CH_4 \Rightarrow products \tag{7.9}$$

A gas phase reaction between H_2S and CH_4 was unfavorable: the amount of CS_2 in our system would be very low (371 ppm at 850 ^oC), and the concentration of CS_2 would be dependent of the current drawn from the cell.

Furthermore, there was a greyish film on the surface of all used anodes after being operated potentiostatically, regardless of the anode used. A similar effect was reported for use of 5% H_2S-CH_4 gas with NiS-YSZ and CoS-YSZ anode materials [21, 22]. XPS analysis of the surface powder shows the presence of a C-O-S species on the surface, with O and S having different binding energies and peaks. TPO of the anode powders showed CO_2 and

SO_2 evolution from the surface of the anode. The amount of carbon present was greater than for the anodes tested in pure CH_4. This further indicated participation of S in the anodic reaction. Unfortunately, the present data are insufficient to fully define the reaction mechanism.

7.5 Conclusions

Catalytic and electrocatalytic activities of perovskites $La_{0.75}Sr_{0.25}Cr_{0.5}X_{0.5}O_{3-\delta}$, (LSCX); where X is a cation of the first row d-transition metals, Ti, Mn, Fe, Co, and their utility as fuel cell anodes using H_2-, H_2S- and CH_4-containing fuels, each depend on the nature of X.

- The oxides where X = Ti, Mn, Fe were sufficiently conductive for fuel cell anode catalyst applications.
- However, LSCCo alone was not stable under reducing conditions, and there was a large thermal expansion coefficient mismatch with YSZ.
- Composite catalysts comprising equal amounts of LSCX and $Ce_{0.9}Ga_{0.1}O_{2-\delta}$ (GDC) were each more active than the corresponding LSCX alone. Further, GDC stabilized LSCCo sufficiently to enable its use as an anode catalyst.
- Temperature programmed reaction (TPR) of CH_4 under O_2-free conditions showed that the catalytic activity of the oxides for conversion of CH_4 was in the order Co>Mn>Fe>Ti.
- The order of CH_4 TPR activities of LSCX approximately parallelled with their electrocatalytic activity. Thus TPR is useful as a preliminary predictor of electrocatalytic activity for conversion of CH_4, which was found to be Fe>Mn>Ti for LSCX alone and Fe>Co>Mn>Ti for LSCX-GDC.
- Fuel cell performances using each of the LSCX anodes was highest using H_2 fuel, and lowest using CH_4. When the fuel was 0.5% H_2S/CH_4 the performance was considerably greater than that in CH_4 alone, and close to that when using pure H_2. Fuel cells using anodes LSCX-GDC performed considerably better than those using LSCX alone; the highest performance attained was 250 mW cm^{-2} using a fuel cell with the configuration LSCFe-GDC | YSZ(0.3mm) | Pt at 850 ^oC.
- The composition of the effluent streams from fuel cell tests, determined using in-situ MS, varied with LSCX. The effluent when 0.5% H_2S/CH_4 was used as a feed differed from that from sulphur-free feeds, and CS_2 was present in the effluent.

7.6 References

[1] E. Konysheva, J.T.S. Irvine, Chem. Mater., 21 (2009) 1514-1523.

[2] J. Sfeir, J. Power Sources, 118 (2003) 276-285.

[3] J. Nowotny, C.C. Sorrell, eds. Key Engineering Materials, 1997, 125-126, 187.

[4] G. Pudmich, B.A. Boukamp, M. Gonzalez-Cuenca, W. Jungen, W. Zipprich, F. Tietz, Solid State Ionics, 135 (2000) 433-438.

[5] E.V. Tsipis, V.V. Kharton, J. Solid State Electroch., 12 (2008) 1367-1391.

[6] S. Tao, J.T.S. Irvine, Nat. Mater., 2 (2003) 320-323.

[7] S. Tao, J.T.S. Irvine, Chem. Mater., 16 (2004) 4116-4121.

[8] J.C. Fisher, S.S.C. Chuang, Catal. Comm., 10 (2009) 772-776.

[9] J. Rossmeisl, W.G. Bessler, Solid State Ionics, 178 (2008) 1694-1700.

[10] N. Danilovic, J.L. Luo, K.T. Chuang, A.R. Sanger, J. Power Sources, 192 (2009) 247-257.

[11] N. Danilovic, J.L. Luo, K.T. Chuang, A.R. Sanger, J. Power Sources, 194 (2009) 252-262.

[12] T. Nakamura, G. Petzow, L. Gauckler, J. Mater. Res. Bul., 14 (1979) 649-659.

[13] H. Falcon, M.J. Martinez-Lope, J.A. Alonso, J.L.G. Fierro, Appl. Catal. B, 26 (2000) 131-142.

[14] R.T. Baker, I.S. Metcalfe, Appl. Catal. A, 126 (1995) 319-332.

[15] R.T. Baker, I.S. Metcalfe, Ind. Eng. Chem. Res., 34 (1995) 1558-1565.

[16] R.T. Baker, I.S. Metcalfe, Appl. Catal. A, 126 (1995) 297-317.

[17] V.V. Kharton, E.V. Tsipis, I.P. Marozau, A.P. Viskup, J.R. Frade, J.T.S. Irvine, Solid State Ionics, 178 (2007) 101-113.

[18] S. Tao, J.T.S. Irvine, S.M. Plint, J. Phys. Chem. B, 110 (2006) 21771-21776.

[19] M. K. Bruce, M. van den Bossche, S. McIntosh, J. Electrochem. Soc., 155 (2008) B1202-B1209.

[20] M. van den Bossche, S. McIntosh, J. Catal., 255 (2008) 313323.

[21] C.M. Grgicak, R. Green, J.B. Giorgi, J. Power Sources, 179 (2008) 317-329.

[22] C.M. Grgicak, M.M. Pakulska, J.S. OBrien, J.B. Giorgi, J. Power Sources, 183 (2008) 26-33.

Chapter 8

Conclusions, recommendations and future work

The potential use of sour natural gas as a fuel in solid oxide fuel cells was investigated using various oxide anodes. Several different compositions were developed and tested. It was determined that a strong correlation existed between the B site dopant, in the perovskite structure ABO_3, and electrocatalytic activity for conversion of CH_4 and H_2S. Perovskites containing the early transition metal cations Ti and V are inactive towards CH_4; the later transition metal cations Mn, Fe and Co are active. At the same time, H_2S has a two fold effect at the concentrations used: first it partially sulfides the V perovskite which leads to an enhancment of activity and conductivity in H_2S; second, partial sulfidation of the surface of the Ti, Mn, Fe and Co perovskites leads to a change in reaction pathway and enhancement of CH_4 oxidation activity. Cr at the B site acts primarily to give the structure redox stability. Substitution at the A site was found to have minimal effect on the performance, although it may have increased the susceptability for redox instability and sulfidation of the structure.

8.1 $Ce_{0.9}Sr_{0.1}VO_3$ and $Ce_{0.9}Sr_{0.1}Cr_{0.5}V_{0.5}O_3$ catalysts

New Ce- and V-containing perovskite ($Ce_{0.9}Sr_{0.1}VO_3$) and zircon-type ($Ce_{0.9}Sr_{0.1}VO_4$) oxide anode materials were tested in H_2S- and CH_4-containing atmospheres. These were adapted from $La_{0.9}Sr_{0.1}VO_3$, which was reported to be active in 0.5% H_2S-CH_4 [1]. The A site subsitution of Ce for La was designed to determine whether the idea that the multivalent Ce cation could also contribute to the reaction enhancing performance.

The zircon-type $Ce_{0.9}Sr_{0.1}VO_4$ anodes are reduced in 0.5% H_2S-CH_4 and in H_2-containing atmospheres. Due to the dimensional changes associated with the reduction of the oxide when bonded to an electrolyte, this material is not a suitable anode.

$Ce_{0.9}Sr_{0.1}VO_3$ anodes are chemically stable in 0.5% H_2S-CH_4 at 950 ^oC for 12 h under non-electrochemical conditions, but $Ce_{0.9}Sr_{0.1}V(O,S)_3$ is formed under 5% H_2S during conductivity measurements, as determined using XRD and XPS analyses.

$Ce_{0.9}Sr_{0.1}VO_3$ anodes have high activity only after the introduction of H_2S to the fuel feed. A possible explanation for the sustainable electrochemical activity of sulfided $Ce_{0.9}Sr_{0.1}$ VO_3 catalyst, consistent with XPS, XRD and DSC/TGA results, is that the structure of the anode must contain a significant portion of O^{2-} to sustain fuel cell activity; such a structure is denoted as $Ce_{0.9}Sr_{0.1}V(O,S)_3$.

After initially forming $Ce_{0.9}Sr_{0.1}V(O,S)_3$ the anodes are only active towards the oxidation of H_2S in the fuel feed. A maximum power density of 140 mW cm^{-2} was achieved at 950 ^oC in 5% H_2S-N_2.

To improve the activity of CSV towards CH_4, Cr^{+3} was chosen as a B site dopant. Addition of Cr^{+3} into CSV to form CSCV led to improved redox stability, and improved conductivity in reducing environments. CSCV had improved electrocatalytic activity towards H_2S oxidation compared to CSV; however, Cr addition did not improve methane conversion activity.

CSCV undergoes a solid-gas reaction with H_2S in which the materials reacts to form $Ce_{0.9}Sr_{0.1}Cr_{0.5}V_{0.5}(O,S)_3$. The oxide retained in the MEA allows continuing O^{2-} conduction.

Admixing of NiO with CSCV increases methane oxidation activity, but the performance of Ni is not stable under the testing conditions. Ni-YSZ-CSCV and CSCV have stable performance for 15 h under polarization conditions using H_2S-CH_4 as fuel.

While CSV and CSCV are not suitable anodes for sour natural gas solid oxide fuel cells, due to their inactivity towards CH_4, they can be used as electrochemcial H_2S scrubbers from CH_4. To evaluate this application, the oxide anode must not catalyze carbon deposition, under all fuel cell conditions. To examine this process, CSCV and VLY anodes were coked under ex-situ (Type I), open circuit (Type II) and galvanostatic (Type III) conditions. Post mortem temperature programmed oxidation (TPO) experiments revealed that similar amounts of carbon (amount of carbon per g catalyst) were deposited to the surfaces of CSCV and VLY, and that total deposition was dependent on operating conditions. In all cases at least two orders of magnitude less of carbon were deposited on the oxide anodes when compared to Ni-YSZ anodes.

VLY and CSCV are methane inactive but hydrogen sulfide active anode catalysts, and can be used to desulphurize a hydrocarbon stream under Type I-III conditions without building up significant carbon deposits.

Ex-situ coking, Type I conditions, of potential anode materials is adequate to predict coking behaviour under electrochemical conditions.

The gold current collector mesh in contact with VLY or CSCV anodes unexpectedly contributed to an increase in carbon deposition during electrochemical coking tests, Type II and Type III conditions. However, under an applied potential, Type III condition, the available amounts of O^{2-} and produced H_2O were sufficient to remove the carbon deposited as a result of the the activity of the current collector.

Recommendations and future work

It is recommended that the use of V containing oxides be limited to applications only when H_2S is present in the anode feed. It is not a good choice for H_2 or CH_4 fuels. It would be of scientific interest to examine the development of the oxysulfide with temperature and H_2S concentration. An in depth structural analysis using neutron diffraction would provide further insights into the identity of the structure and O^{2-}/S^{2-} positions in the oxysulfide lattice. The concept of a electrochemical H_2S scrubber should be developed further, and long-term coking experiments should be conducted in the presence of H_2S to further prove the viability of the concept.

8.2 $La_{0.75}Sr_{0.25}Cr_{0.5}X_{0.5}O_{3-\delta}$ (X= Ti, Mn, Fe, Co) catalysts

The work herein is the first attempt to determine catalyst activity trends for solid oxide fuel cells. By varying the B site dopant in a consistent, isostructural parent oxide I was able to determine the optimal catalytic dopant among the first row transition metals. The catalytic and electrocatalytic activities of perovskites $La_{0.75}Sr_{0.25}Cr_{0.5}X_{0.5}O_{3-\delta}$, (LSCX); where X is a cation of the first row transition metals, Ti, Mn, Fe, Co, and their utility as fuel cell anodes using H_2-, H_2S- and CH_4-containing fuels, each depend on the nature of X. The oxides where X = Ti, Mn, Fe are sufficiently conductive for fuel cell anode catalyst applications. However, LSCCo alone is not stable under reducing conditions, and there is a large thermal expansion coefficient mismatch with YSZ.

Composite catalysts comprising equal amounts of LSCX and $Ce_{0.9}Ga_{0.1}O_2$ (GDC) are each more active than the corresponding LSCX alone. Further, GDC stabilizes LSCCo sufficiently to enable its use as anode catalyst. Fuel cell performances using each of LSCX are highest using H_2 fuel, and lower using CH_4. When the fuel is 0.5% H_2S/CH_4 the performance is considerably greater than that in CH_4 alone, and close to that when using pure H_2. Fuel cells using anodes LSCX-GDC perform considerably better than those using LSCX alone; the highest performance attained was 250 mW cm^{-2} using a fuel cell with the configuration LSCFe-GDC | YSZ(0.3mm) | Pt at 850 ^oC.

The composition of the effluent streams from fuel cell tests, determined using in-situ MS, varied with LSCX. The effluent when 0.5% H_2S/CH_4 was used as a feed differed from that from sulphur-free feeds, and CS_2 was present in the effluent.

Temperature programmed reaction (TPR) of CH_4 under O_2-free conditions showed that the catalytic activity of the oxides for conversion of CH_4 is in the order Co>Mn>Fe>Ti. The order of CH_4 TPR activities of LSCX is approximately parallel with their electrocatalytic activity. Thus TPR is useful as a preliminary predictor of electrocatalytic activity for conversion of CH_4, which was found to be Fe>Mn>Ti for LSCX alone and Fe>Co>Mn>Ti for LSCX-GDC.

Recommendations and future work

It is recommended that this concept of testing dopants in mixed oxides be extended to other fuel cell anode catalyst oxide systems, for instance the pyrochlores or the double perovskites, to see if the same trends persist independent of structure. LSCFe appears to be adequately stable and active to be further optimized as a fuel cell catalyst. The Sr dopant concentration (Sr/La) can be changed, and the proportion of Fe dopant concentration (Cr/Fe) can be changed to see if there will be an improvement in activity. Furthermore, the composition and structure of either LSCX or LSCX-GDC are as yet unoptimized, and so a series of rational variations is required to determine optimum performance. For example, a second catalytic component may be added, such as Ni or a noble metal dopant at 5 wt% concentration, to determine the effect on the reaction rate, which is sluggish on the oxide. The ideal system would be an anode supported LSCFe-GDC-Ni anode with a thin electrolyte and LSM or other perovskite cathode; this kind of cell should yield superior performance.

Of scientific and technical importance is the nature of activation of CH_4 on the oxide anodes in the presence of H_2. The minimum H_2 concentration that achieves this should be determined,and this would give further insight to the phenomena. The C-O-S surface phase presently is unknown, and should be further analysed to identify its nature and function, to determine if it participates in the reaction as an intermediary or as a product.

8.3 References

[1] Z. Cheng, S. Zha, L. Aguilar, D. Wang, J. Winnick, M. Liu, Electrochem. Solid-State Lett., 9 (2006) A31-A33.